BATTERY TESTING AND THERMAL ANALYSIS FOR

ULTRA-FAST CHARGING

TESTING, CHARACTERIZATION, AND THERMAL ANALYSIS OF

LITHIUM-ION BATTERIES TOWARD BATTERY PACK DESIGN FOR

ULTRA-FAST CHARGING

By MELISSA HE, B.Sc.

A Thesis Submitted to the School of Graduate Studies

in Partial Fulfilment of the Requirements for the Degree

Master of Applied Science

i

MASTER OF APPLIED SCIENCE (2018)   McMaster University

(Mechanical Engineering)   Hamilton, Ontario

TITLE: Testing, Characterization, and Thermal Analysis of

Lithium-Ion Batteries Toward Battery Pack Design

for Ultra-Fast Charging

AUTHOR: Melissa He, B.Sc. (McMaster University)

SUPERVISOR: Professor Ali Emadi

NUMBER OF PAGES: xvi, 106

Lay Abstract

Ultra-fast charging of electric vehicles, i.e., fully charging the vehicle in less than 15 minutes, will soon be more available. However, literature on the ultra-fast charging of the batteries used in these vehicles is limited. It is not widely known whether the batteries can effectively achieve ultra-fast charging or how the batteries behave under these conditions. Charging batteries this fast means that the battery cells will heat up. The temperature of the cell greatly impacts its longevity and safety. The thesis attempts to address these questions by studying three commercial lithium-ion batteries, selected for specific characteristics, that show potential for ultra-fast charging. The batteries are charged at different rates to ultra-fast charging levels and the charge performance at each rate is determined. The temperature of the batteries is simulated with different cooling systems to determine how effectively must heat be removed from the batteries to maintain the cells at a specific temperature.

Abstract

Ultra-fast charging of electric vehicles will soon be available to charge the batteries in less than 15 minutes to 80% state of charge. However, very few studies of batteries under these conditions exist. To design a battery pack with ultra-fast charging in mind, more information about batteries is needed, both electrically and thermally. In this thesis, the performance of three specific commercial lithium-ion batteries during ultra-fast charging is investigated and their thermal behaviour is simulated for use in the battery pack design process. The cells are charged at 1C to 6C current rates, or as high as 10C, and the surface temperature of each cell is measured. The loss calculated from the charging tests are used in a thermal analysis of the three batteries using finite element analysis. The batteries are modeled in a simple cooling apparatus to determine their thermal management requirements in a pack, i.e., how effectively must the heat be removed from the cells to obtain a specific temperature in a pack. Test results show that ultra-fast charging is possible with very little loss; but, it is dependent on the battery. The analysis illustrates important trade-offs between the battery type, charge rate, and the thermal management system. This thesis presents a holistic view to the study of the batteries for eventual use in the design of a battery pack. The thermal performance of the batteries is equally important as their electrical (charge) performance. It also attempts to justify the observed behaviour of the batteries by their underlying chemical behaviour. The work here can be used as a jumping-off point for further work on the ultra-fast charging of batteries or the design of a battery pack.

Acknowledgments

First and foremost, I want to thank my supervisor, Dr. Ali Emadi. Thank you for taking a chance on a chemist who wanted to be an engineer. I so appreciate all of the opportunities and experiences I have gained from this group.

I would like to express my gratitude to every member of the battery group: Dr. Phillip Kollmeyer, Dr. Ran Gu, Mackenzie Wootton, and Mike Haußmann. I am so grateful for everyone giving up their time and sharing their knowledge with me. Special thanks to Mike for building the test fixtures and Phil for providing the vehicle model used in the thermal analysis.

I would also like to thank all of my teammates over the years on the McMaster University Varsity Fencing Team, especially the épée team. University would have been less bearable if I could not stab my friends.

Last but not least, I want to thank my family, Kevin, Sue, and Sabrina. It is not hyperbole to say that I would not have made it to this point without your support.

Table of Contents

List of Figures

List of Tables

Abbreviations

CCCV	Constant Voltage/Constant Current
EV	Electric Vehicle
FEA	Finite Element Analysis
HPPC	Hybrid Pulse Power Characterization
LCO	Lithium Cobalt Oxide
LIB	Lithium-Ion Battery
Li-GIC	Lithium-Graphite Intercalation Compound
LFP	Lithium Iron Phosphate
LMO	Lithium Manganese Oxide
LTO	Lithium Titanate Oxide
NCA	Lithium Nickel Cobalt Aluminum Oxide
NMC	Lithium Nickel Manganese Cobalt Oxide
OCV	Open Circuit Voltage (V)
SOC	State of Charge (%)

Symbols

C_p	Heat Capacity (J/kg·K)
E_{chg}	Charge Energy (Wh)
E_{dis}	Discharge Energy (Wh)
$E_{dis,loss}$	Discharge Energy Loss (Wh)
I	Current (A)
κ	Thermal Conductivity (W/m·K)
η_{chg}	Charge Efficiency (%)
p	Plate Thickness (% Cell Thickness)
P_{chg}	Charge Pulse Power Capability (W)
$P_{chg,loss}$	Charge Loss (W)
P_{dis}	Discharge Pulse Power Capability (W)
Q	Heat/Loss (W)
σ	Density (kg/m^3)
R_{chg}	Charge Cell Resistance (Ω)
R_{dis}	Discharge Cell Resistance (Ω)
T	Temperature (°C)
V	Voltage (V)

Chapter 1
Introduction

1.1. Background and Motivation

With rising oil prices and stricter emissions regulations, electrified vehicles, especially electric vehicles (EVs), are an attractive alternative to the conventional gasoline-only vehicles. The high energy and power density of lithium-ion batteries (LIBs) make them ideal for these vehicles [1]. However, a barrier to adoption of EVs is their charging time. Vehicle chargers are currently classified in three groups: Level 1 chargers, which have power levels between 1 and 2 kW and charge times up to 36 hours, Level 2 chargers, which have power levels between 4 and 20 kW and charge times up to 10 hours, and Level 3 (or fast) chargers, which have power levels between 50 and 120 kW and charge times up to around an hour [2].

In attempt to solve the problem of long charge times in EVs, there has been a significant push for fast chargers. From 2015 to 2016 alone, the number of Level 3 chargers globally increased by 290%, while Level 1 and 2 chargers combined only increased by 30% [3]. But Level 3 chargers still do not achieve the convenience of gasoline. The charge time for EVs must be comparable to the refueling time for gasoline-powered vehicles. Ultra-fast chargers, which are capable of 350 kW of power and battery charge times of 15 minutes or less, are expected to alleviate the inconvenience of EVs. Plans for ultra-fast charging networks have been announced in Europe and North America (Figure 1.1a) [4]–[6].

Ultra-fast charging, i.e., charging a battery to 80% of its capacity in less than 15 minutes, has already been achieved in electric buses or e-buses (Figure 1.1b). ABB, Microvast, Siemens, and Endesa, to name a few, have implemented ultra-fast charging systems throughout Europe and Asia to provide top-up charges for buses in less than a minute or a full bus recharge in less than 15 minutes [7]–[10]. With a majority of these systems, LIBs are used in the e-buses [11], [12]. In particular, lithium iron phosphate (LFP) dominates the market at 80% of all e-buses, due to its high safety and lower price. This is followed by lithium titanate oxide (LTO), which is known for its high charge and discharge rates and excellent cycle life [13]. While in the laboratory, other LIBs have shown potential for ultra-fast charging. Wu *et al.* showed that lithium nickel manganese cobalt oxide (NMC) could be charged and discharged to 100C in a coin cell using lithium metal as the counter electrode [14]. NMC is attractive option because of its higher operating voltage and energy density. Unfortunately, literature on the behaviour as well as the performance of commercial LIBs during ultra-fast charging is limited. Prezas *et al.* studied effects on a battery at 6C charge [15]. Yang and Miller have investigated the effect of charging at 16C [16]. The surface temperature of a battery cell during 3C charge by Grandjean *et al* [17]. Kim *et al.* measured the temperature of a cell during 3C and 5C charge [18]. Keyser *et al.* presented simulations that give the thermal implications of ultra-fast charging for different LIBs [19]. Burke and Miller investigated battery aging at 4C charge [20]. With all of these works, no direct comparisons can be made between the batteries as different methodologies were used.

Ultra-E

Ionity

Electrify America

350 kW

350 kW

350 kW

(a)

ABB

Microvast

Geneva, Switzerland

Chongqing, China

Siemens

Endesa

Hamburg, Germany

Barcelona, Spain

(b)
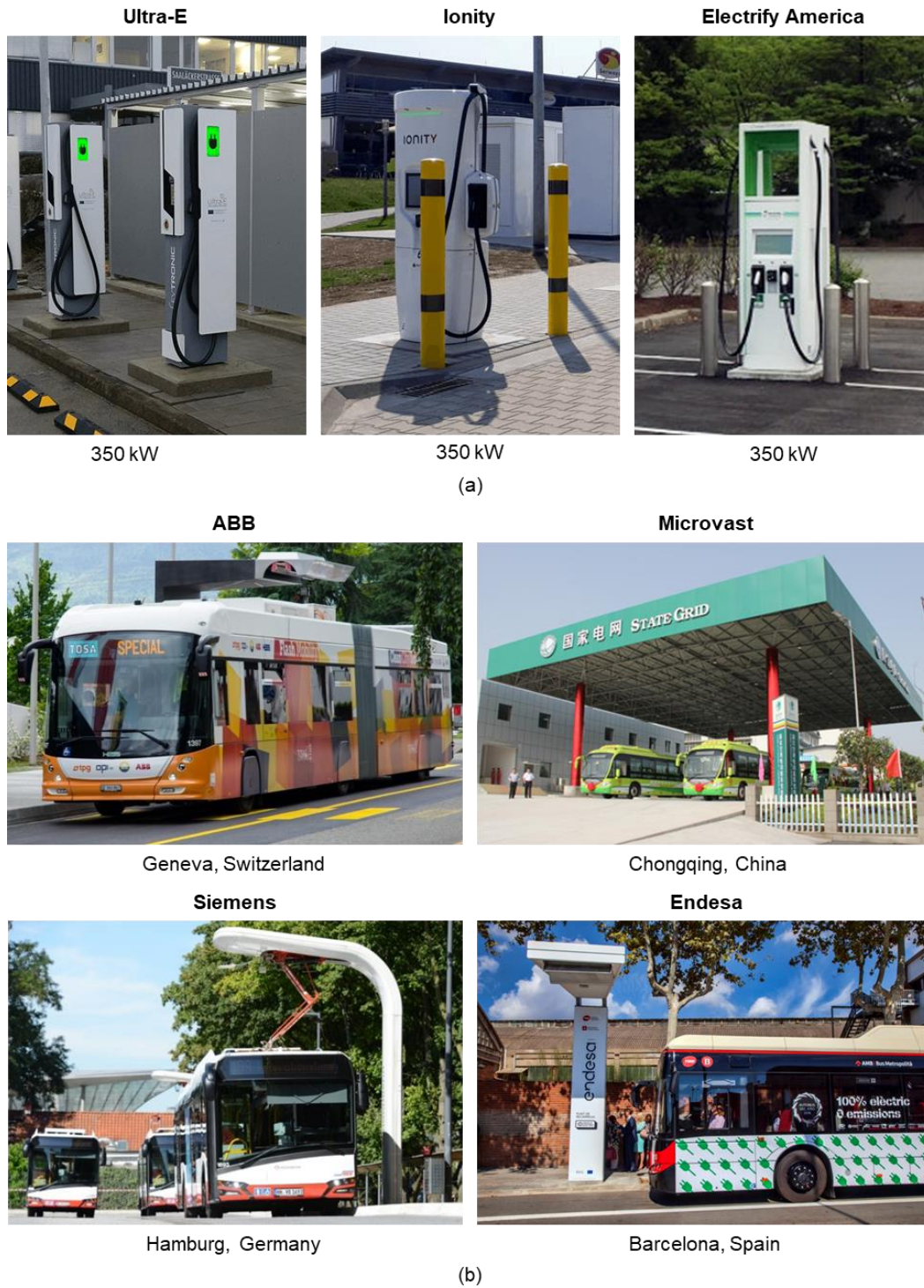
Figure 1.1. Examples of (a) ultra-fast chargers for EVs and (b) ultra-fast charging of electric buses.

1.2. Contributions

As ultra-fast charging will likely be a feature in most next-generation EVs, more research on ultra-fast charging is needed for a wide variety of commercial LIBs to inform the design of battery packs with ultra-fast charging capabilities. In addition, it is important to understand the thermal behaviour of LIBs under these ultra-fast charging conditions. The thermal implications of ultra-fast charging are significant. Due to the high current and power associated with ultra-fast charging, charging now becomes a substantial source of heat generation in an EV. During ultra-fast charging, the batteries experience higher continuous current for a longer period of the time when compared to typical driving conditions, which means elevated cell temperatures.

The significance of the work presented in this thesis is that it begins to address the holes in knowledge about the batteries used in the ultra-fast charging of EVs. It brings together concepts from literature regarding ultra-fast charging to present a comprehensive study of LIBs during ultra-fast charging. In this thesis, the ultra-fast charging performance of different commercial LIBs are compared to evaluate their suitability for EVs and the trade-offs between battery performance and thermal management are identified for the design of a battery pack for ultra-fast charging. The purpose of the thesis is to provide a resource and a starting point for the design of a battery pack for ultra-fast charging. Note that aging is not considered in the study. Aging is a definite consequence of repeated charging of a battery [21]. But there was no significant change in capacity from testing.

1.3. Thesis Outline

In conjunction to the work on the ultra-fast charging of LIBs, there are two specific objectives for this thesis:

(1) Establish a holistic approach to the selection of a battery for a battery pack that considers the thermal performance of the battery with its electrical performance. The thermal behaviour of a battery cannot be separated from its electrical behaviour. When they are separated, the thermal management system for the pack will be overdesigned, and the resulting pack will be larger, heavier, and more expensive.

(2) Reconcile the electrical engineering with the chemistry. A battery is not a black box. It is important to understand the electrochemical principles that underlie the observed behaviour of the battery during operation. Without some understanding of these principles, an informed selection of a battery cannot be truly made when designing a battery pack.

These two objectives are addressed in the context of ultra-fast charging LIBs. In Chapter 2, the fundamentals of LIBs and its state of the art, i.e., current state and future trends, are reviewed to provide a background for the discussion of batteries with ultra-fast charging. In Chapter 3, LIBs are discussed with ultra-fast charging in mind. Here, factors that dictate the charge capability of a battery are examined. The impact of ultra-fast charging on the battery components is also explored. Heat generation and the thermal behaviour of LIBs during charging are then explained. In Chapter 4, commercial LIBs are chosen and characterized for ultra-fast charging.

This includes the cell resistance and power capabilities. The charge performance, specifically efficiency and power loss, of the batteries is evaluated and compared. Knowledge of LIBs from Chapters 2 and 3 are used to explain the observed charge behaviour of the batteries. In Chapter 5, the thermal management requirements for the batteries are explored via finite element analysis of a range of cooling system designs. The loss calculated from experimental testing is used as an input for the thermal model. The temperature of the cells is investigated at steady state and then over time to obtain their transient behaviour. The impact of the cooling system on the use of each battery in a pack is compared. The work in Chapter 5 illustrates the trade-offs between the electrical performance (charging) and the thermal behaviour (cooling) of the three batteries. Their actual thermal management requirements are determined so that the thermal management system is not overdesigned. Chapter 6 introduces work to experimentally validate the thermal analysis. A test fixture was designed and built, and test plans for the selected battery and fixture are discussed. In Chapter 7, conclusions from the research are summarized where the next steps and future work are explained.

Chapter 2
Lithium-Ion Batteries: Fundamentals, Current Status, and Future Trends

2.1. Battery Fundamentals

2.1.1. Battery Operation

A battery is a device that converts chemical energy into electrical energy upon discharge [22], [23]. This is achieved through two key chemical reactions, oxidation and reduction. The battery cell can be separated into three active regions: the (1) negative electrode, (2) positive electrode, and (3) electrolyte (Figure 2.1a). At the negative electrode or anode, electrons are released from the material via oxidation, which produces positive ions (red). These positive ions migrate from the negative to the positive electrode through the electrolyte. Here, a separator allows the transport of the ions through the electrolyte but prevents electron movement. As a result, electrons flow through an external circuit to the positive electrode, which generates a current. At the positive electrode, or cathode, the electrons are accepted by the material via reduction. The resulting negative ions (blue) migrate from the positive to the negative electrode to complete the conversion.

Batteries can be classified as either primary or secondary. In a primary cell, the chemical reactions are irreversible; once the battery has been discharged and all of the material has been reacted, the battery must be discarded. But in a secondary cell, the reactions are reversible via the application of an external current. Electrons

can be forced back into the material at the negative electrode. During charge, oxidation occurs at the positive electrode, which is now the anode, and reduction occurs at the negative electrode, now the cathode (Figure 2.1b). The associated ions migrate toward the opposing electrodes and the battery is returned to its original state. The secondary cell is also known as a rechargeable battery as it can be repeatedly discharged and charged. An example of a primary cell is the alkaline battery. Secondary cells include lead-acid, nickel-cadmium (Ni-Cd), nickel-metal hydride (Ni-MH), and lithium-ion batteries (LIBs). LIBs will be discussed here. Lithium ions are transported back and forth between electrodes where lithiation and delithiation describes their insertion and removal of the lithium ions.
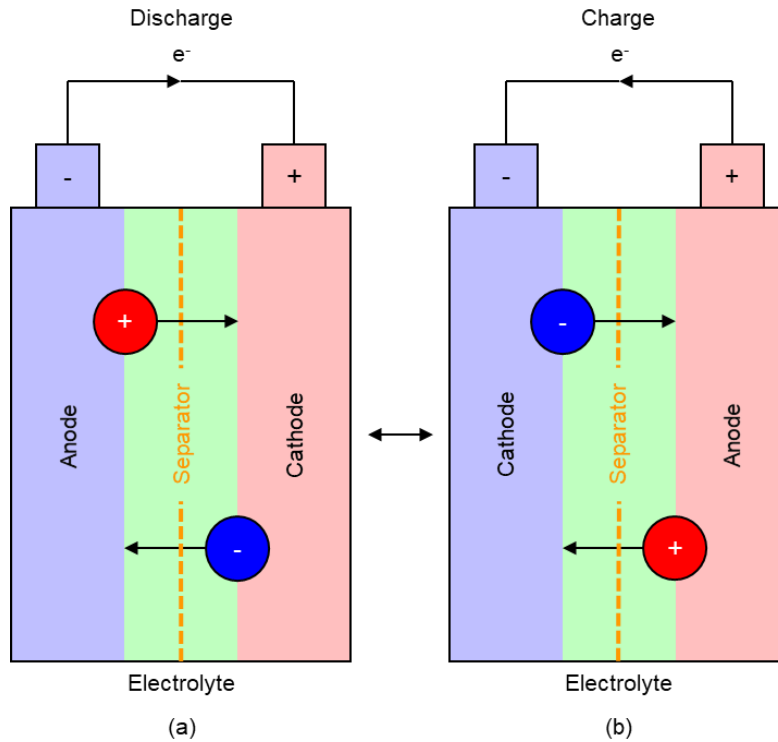
Figure 2.1. Schematic of a battery cell during (a) discharge and (b) charge.

2.1.2. Battery Definitions

The capacity (Ah) of a battery is a measure of the charge stored in a cell. It gives the total current that can be delivered over time by the cell. A battery with a higher capacity therefore has a longer run time. The state of charge (SOC) of a battery is a measure of the remaining charge in a cell. The SOC is expressed as a percentage; it is the remaining capacity of a cell relative to its maximum capacity. The charge or discharge rate specifies the speed at which a battery is charged or discharged. It is described as a C-rate, which is the magnitude of the current relative to the capacity of the battery. For example, a 1C rate for a 20 Ah cell equals a 20 A of current, which can charge or discharge the battery in one hour. A 0.5C rate equals a current of 10 A that charges or discharges the battery in two hours. And a 2C rate equals 40 A of current to charge or discharge the battery in 30 minutes.

Energy and power density are two important characteristics of a battery [24]. The energy density gives the storage capability of a cell. It describes how much energy a cell can hold by mass, gravimetric/specific energy density (Wh/kg), or volume, volumetric energy density (Wh/L). The power density then gives the load capability of the cell. This describes how much power can be given to a load per unit mass, gravimetric/specific power density (W/kg), or unit volume, volumetric power density (W/L). The rate capability of a battery is linked to its power density. Power is a product of current and voltage. Assuming all things being equal apart from the power density, i.e., capacity, mass, voltage, a battery with a higher power density means that it is capable of higher currents and therefore, higher rates.

2.2. Current Status of Lithium-Ion Batteries

For the discussion of LIBs, the negative electrode is referred to as the anode and the positive electrode, the cathode. Performance and safety characteristics of a battery are dependent on the materials and construction in the cell.

2.2.1. Cathode

There are five chemistries currently available on the market (Table 2.1). Lithium cobalt oxide ($LiCoO_2$) or LCO was the first chemistry used in commercial LIBs. It has double the energy density of Ni-Cd and Ni-MH cells and much better cycling performance. However, LCO suffers from low thermal stability and high cost, which can be attributed to the presence of cobalt. Bonds with cobalt are weak. When LCO is heated, the oxide decomposes to produce oxygen. The high cost is then due to the scarcity of cobalt. Lithium manganese oxide ($LiMn_2O_4$) or LMO was introduced as an alternative to LCO. Manganese is more readily available, which decreases the cost of the material. But the cycling performance of LMO is much poorer. This is because LMO undergoes phase (structural) changes during cycling and manganese leaches out of the material. Another alternative to LCO is lithium nickel cobalt aluminum oxide ($LiNiCoAlO_2$) or NCA, which uses nickel and aluminum to lower the cobalt content in the material. NCA maintains the high energy density of LCO but also has the structural stability needed during cycling. Still, the presence of cobalt means that the thermal stability of the material is low. Lithium iron phosphate ($LiFePO_4$) or LFP has the thermal and structural stability. The phosphate is less reactive than the oxide. It also has a high power density. A

major weakness of LFP is its low electrical and ionic conductivity. Lithium nickel manganese cobalt oxide ($LiNiMnCoO_2$) or NMC is the latest cathode material to be brought to market. NMC achieves both a high energy density and power density.

Table 2.1. Cathode chemistry specifications for LIBs.

	LCO	LMO	NCA	LFP	NMC
Structure	Layered	Spinel	Layered	Olivine	Layered
Theoretical Capacity (mAh/g)	274	148	279	170	280
Nominal Voltage (V)	3.6	3.8	3.7	3.2	3.7
Operating Voltage Range (V)	3.0–4.2	3.0–4.2	3.0–4.2	2.5–3.65	3.0–4.2
Energy Density					
Gravimetric (Wh/kg)	170–245	150–240	130–240	70–150	70–200
Volumetric (Wh/L)	400–640	240–360	490–670	100–300	150–400
Power Density					
Gravimetric (W/kg)	~1000	~4000	~1000	~4000	~4000
Volumetric (W/L)	~2000	~10000	~2000	~10000	~10000
Electrical Conductivity (S/cm²)	$\sim10^{-1}$	$\sim10^{-6}$	$\sim10^{-5}$	$\sim10^{-8}$	$\sim10^{-5}$
Ionic Diffusivity (cm²/s)	$\sim10^{-10}$	$\sim10^{-11}$	$\sim10^{-10}$	$\sim10^{-9}$	$\sim10^{-9}$

Obtained from [25]–[30]

2.2.2. Anode

Graphitic carbon is used for the anode in most commercial LIBs [28]. The voltage of a battery arises from the difference in reduction potential between the graphite anode and the cathode material. LCO has the highest operating voltage range, followed by NMC and NCA. LFP has the lowest range. A higher operating range is preferred as more energy can be stored and then used. Lithium titanate ($Li_4Ti_5O_{12}$) or LTO is another anode material found on the market. LTO is known for its high power density and cycle life [31]. It has a larger surface area compared to graphite, which allows for more lithium ions to be inserted into the material. And many of the reactions that degrade graphite during cycling do not occur with LTO. The usage of LTO is limited by its low voltages and energy density [31].

2.2.3. Cell Format

LIBs are available in three formats, as a cylindrical, pouch, or prismatic cell. In a cylindrical cell, alternating layers of the electrode materials are wound into a jelly-roll structure and placed in a tubular metal case (Figure 2.2a). In a pouch cell, the electrode materials are stacked in alternating layers; the stack is then covered with a metalized plastic material and sealed to form a so-called pouch (Figure 2.2b). In a prismatic cell, the electrode materials can be wound or stacked and are placed in a rectangular metal case (Figure 2.2c). Cylindrical cells are found in everything from laptops to the Tesla vehicles. Pouch cells come in all different sizes and are used in cellphones to drones and other vehicles. Prismatic cells are typically used in automotive applications.

The cylindrical cell is the most common format for LIBs. The jelly roll allows for more material to be packed into the cell, resulting in a high energy density. The cell has good mechanical stability; the tubular casing can withstand high internal pressures without deforming. However, the packaging efficiency of cylindrical cells is low. The round nature of the cell means that there will always be gaps between cells when placed side by side. The prismatic cell can achieve a similar energy density with a better packaging efficiency. But prismatic cells are more expensive to manufacture than cylindrical cells. The structural stability of the cell is also lowered, and the cell has been shown to expand during cycling. The pouch cell is the lightest and smallest format, has the best packaging efficiency. It also requires support because the cell is soft and will expand.
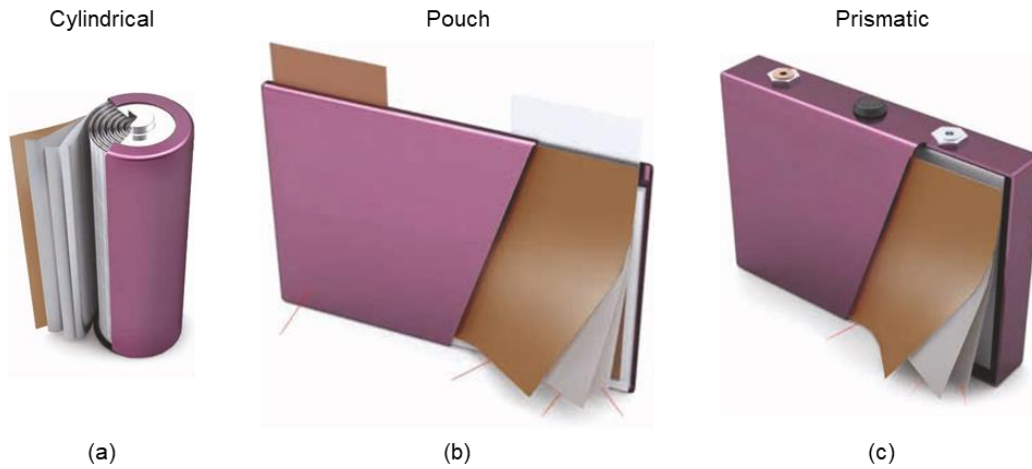
Figure 2.2. Formats for lithium-ion batteries: (a) cylindrical, (b) pouch, and (c) prismatic cell [27].

2.3. Future Trends in Lithium-Ion Batteries

There are two key trends for LIBs: (1) larger capacity (energy density) and (2) higher power (power density) [32]–[35]. Gasoline, for example, has an energy density of 14000 Wh/kg. The best commercial LIB only has an energy density of 250 Wh/kg [35]. With all of the progress in EVs and the associated technologies, the battery energy density does not need to equal the gasoline energy density. At present, research is aimed at doubling the energy density of LIBs to 600 Wh/kg to meet the energy demands of EVs. And with ultra-fast charging and increasing electrification of vehicles, from passenger cars to long-haul trucks, LIBs must also be able to support any power demand. This is only possible if the battery has a high power density. LTO can achieve the desired charge and discharge rates, but this comes at the cost of the energy density. In current LIBs, there is a trade-off between the energy and power density, as shown by the Ragone plot in Figure 2.3. There are no batteries that meet the energy and power requirements for electrified vehicles.

For instance, to meet the USDOE goal for EVs shown in Figure 2.3, a battery that meets the power density requirements must double its energy density.
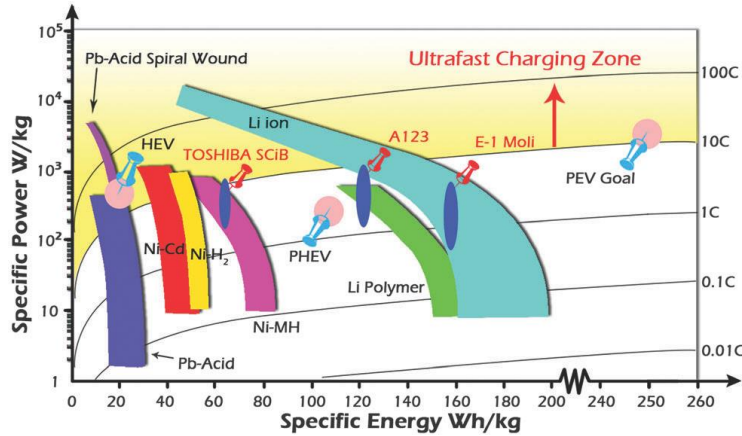
Figure 2.3. Ragone plot of different battery types for ultra-fast charging [36].

Advancements in batteries can be separated into new battery technologies that will replace existing technologies or existing technologies that are improved using materials engineering strategies. Notable strategies include nanostructuring, doping, and hybridization. Nanostructuring replaces the original material with a nanoscale equivalent, whose particles range from 1 nm to 100 nm in size. Doping introduces ions into the original material. Hybridization combines the original material with other materials to form new composite materials.

2.3.1. Energy Density

There are energy-increasing technologies that are ready, in part, to be used commercially. They include silicon-based anodes and nickel-rich cathode materials. Silicon has a high theoretical capacity (4000 mAh/g) when compared to graphite (360 mAh/g), which results in more than a ten-fold increase in the energy density

for a cell with the same chemistry and format. But initial work on cells with silicon anodes show large volume changes with lithiation and delithiation, which leads to cell failure. Materials engineering has been used to minimize the volume changes [37]–[39]. Nanostructuring silicon into nanowires or nanotubes, for example, allow for mechanical strain relief [38]. At the nanoscale, silicon particles can withstand volume changes without cracking. The stability of the silicon anode can also be improved through hybridization. Silicon has been combined with carbon materials, e.g., graphite, carbon black, porous carbon, graphene, carbon nanotubes, or alloyed with metals, e.g., Cu-Si, $FeSi_6$, Mg_2Si [37]. And to minimize the volume changes, silicon has been used as a dopant instead. When a small amount of silicon (<8 wt%) was combined with graphite, the energy density of the anode increased by 20% [40].

In a similar manner, there have been attempts to increase the energy density of cathode materials by increasing the nickel content in the material [34], [41]–[43]. In nickel-rich materials, the formation of nickel compounds allows for more lithium ions to be inserted into the cathode, which increases its energy density (Figure 2.4a). This can be seen in NMC. NMC has the form $LiNi_xMn_yCo_zO_2$ where $x + y + z = 1$. The ratio of the nickel, manganese, and cobalt can be tuned to obtain any desired performance (Figure 2.4b). The most common is $LiNi_{0.33}Mn_{0.33}Co_{0.33}O_2$, which is often referred to as NMC 111 due to the 1:1:1 ratio of nickel, manganese, and cobalt. $LiNi_{0.6}Mn_{0.2}Co_{0.2}O_2$ or NMC 622 and $LiNi_{0.8}Mn_{0.1}Co_{0.1}O_2$ or NMC 811 has shown great promise in energy density [35]. NMC 622 has an energy density of 225 Wh/kg, while NMC 811 has an energy density of 245Wh/kg [44].

15
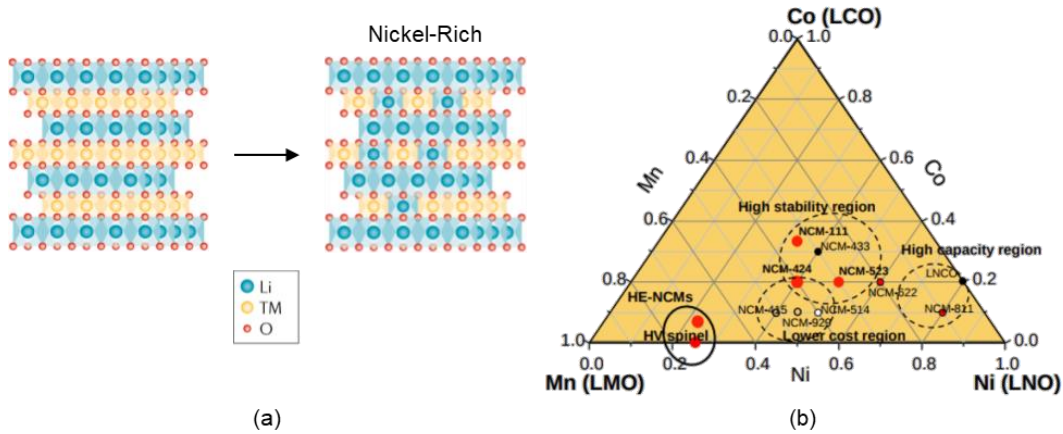
Figure 2.4. (a) Structure of nickel-rich cathode material [34] and (b) ternary phase diagram for nickel, manganese, cobalt, and the associated NMC chemistries.

Other energy-increasing technologies, including lithium metal anodes or lithium-oxygen batteries, have the potential to be industry changing [34], [45]–[47]. But these technologies are not yet fully understood. There are still major hurdles to overcome before they can be commercially implemented. Lithium metal has a theoretical capacity of 3860 mAh/g, similar to silicon and more than ten times higher than graphite. However, cells with a lithium metal anode are unstable due to dendrite formation, which makes them inviable. Materials engineering is being used to make lithium metal a viable option [48], [49]. In lithium-air cells, the anode material is replaced by oxygen, which has a theoretical energy density similar to gasoline. But the cyclability of lithium-air batteries are poor. Severe capacity fade can occur after a few cycles and most lithium-air batteries can only achieve about 50 cycles before capacity fade occurs [46]. This is orders of magnitude less than the cycle life of current LIBs. Another issue for these batteries is a low power density. To be viable, both a high energy density and power density are needed.

2.3.2. Power Density

The power density is associated with the movement of lithium ions between the anode and cathode. Materials engineering has been applied to the existing electrode materials to increase the transport rate for lithium ions and improve the power density of the battery while maintaining its energy density. Nanostructuring increases the surface area for lithium ion insertion and reduces the time required for insertion into the electrode [50]. In this case, carbon nanostructured materials, such as graphene or graphene oxide and carbon nanotubes, are used for the anode instead of graphitic carbon [50]. Mukherjee *et al.* used reduced graphene to achieve charge rates above 100C [51]. Nanostructuring cathode materials, which include nanowires and nanoplates, are able to achieve higher rates than normal as the larger surface area of the nanostructure reduces the current applied to the cathode per unit area [52]–[55]. In doping, ions are introduced to enhance the conductivity of the electrodes by removing or gaining electrons. Wu *et al.* achieved a charge time of 30 seconds using doped graphene sheets for the anode [56]. Doping can also be used to enhance the stability of a high-power material. Kim *et al.* showed that doping nickel-rich NMC with aluminum improved its stability, which allowed for a cycle life of more than 3000 cycles [57]. For hybridization, conductive materials are added to electrode material to create composite materials with better transport rates and higher electrical conductivities. The conductive material provides additional pathways for lithium ion insertion. Derrien *et al.* show that tin-carbon composite anode can be charged above 5C while maintaining its capacity [58].

Chapter 3
Lithium-Ion Batteries and Ultra-Fast Charging

3.1. Lithium-Ion Batteries with Ultra-Fast Charging Capabilities

Current LIBs cannot achieve the energy density of gasoline fuel. As a result, LIBs must achieve gasoline-like convenience in order for EVs to compete with the gasoline-powered vehicles. The goal with ultra-fast charging is to achieve a similar charge time for the battery to the fill time for a tank of gasoline. This is realized by increasing the battery power density. Ultra-fast charging can only be achieved if the LIB has an appropriately high rate capability.

3.1.1. Rate Capability for Ultra-Fast Charging

The rate capability is dictated by the transport rates of lithium ions and electrons, which includes the migration rate of lithium ions through the electrolyte as well as the diffusion rate of lithium ions and electrons in and out of the electrode material [36], [59]–[61]. When the rates of these transport processes align, the battery functions as expected. Problems occur when there is a mismatch between any of these transport rates. Stress is put on the electrodes that can lead to fragmentation, disintegration, and/or fracturing of the electrodes [62]–[64].

The electrode material can be viewed as a matrix in which lithium ions are homogeneously embedded into the matrix (Figure 3.1). Lithium ions are extracted from the material, leaving holes in the matrix. These holes are then filled by the

insertion of lithium ions. At a high enough rate, the extraction and insertion of lithium ions falls out of sync and the distribution of lithium ions in the materials becomes inhomogeneous. Some of these holes remain unfilled, while others are partially filled or overfilled. As a result, areas of the electrode material will expand or contract, leading to its deformation [65], [66].
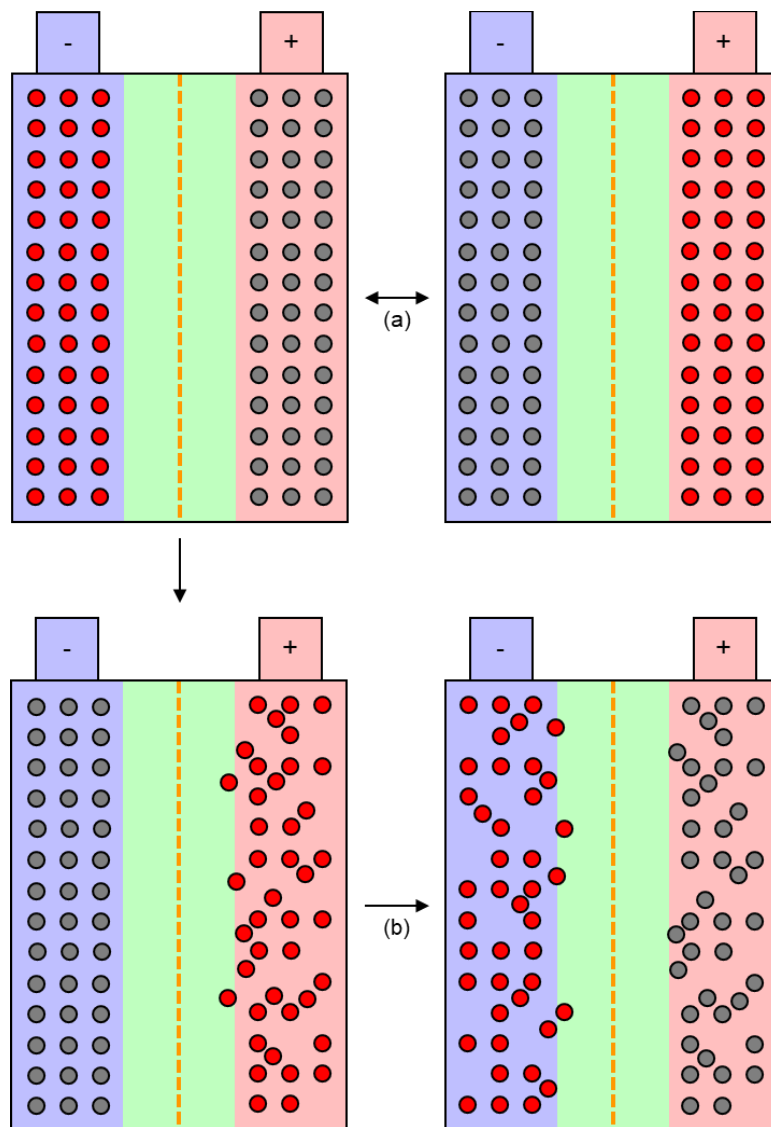
Figure 3.1. Insertion and removal of lithium ions from the electrodes (a) within the rate capability and (b) above the rate capability of the battery.

3.1.2. Battery Materials for Ultra-Fast Charging

The rate capability of a battery can be improved in three ways: (1) increase ionic diffusivity in the electrode materials, (2) enhance ionic conductivity in the electrolyte, and (3) improve electrical conductivity in the electrode materials. Since commercial LIBs cannot be altered to achieve a higher rate, information about the battery materials, i.e., anode, cathode, electrolyte, can help inform the cell selection for the battery pack and explain the behaviour of the cells during ultra-fast charging.

3.1.2.1. Anode

The anode in commercial LIBs has remained relatively unchanged [67]. Graphitic carbon has been used for the anode since the commercialization of LIBs. Therefore, it is important to understand the limitations of this material for ultra-fast charging. Graphite consists of layers of carbon atoms arranged to form a hexagonal lattice (Figure 3.2). Lithium ions are inserted between the layers in a process called intercalation. Intercalation can be broken down into four stages (Figure 3.2). The stages are characterized by a progressive increase in spacing between carbon layers due to the insertion of lithium ions between the layers. Interactions between the carbon atoms and lithium ions at each stage form lithium-graphite intercalation compounds (Li-GICs). Li-GICs are observed as distinct phases in the anode that show the progression from one stage to the next (Figure 3.3a) [68]. At full lithiation, there is, at maximum, one lithium ion per six carbon atoms, giving rise to the Li-C_6 structure typically found for graphite. The maximum gravimetric energy density of graphite is then 279 Wh/kg [69].

Graphite is known to have a poor rate capability during charge. At high charge rates, intercalation is impacted by the poor diffusion at the interface of the anode with the electrolyte [70]. During transport, lithium ions are stabilized by a shell of the electrolyte. This shell must be removed in order for lithium ions to move past the interface [70]. There is an energy barrier associated with the removal of the electrolyte shell, which impedes lithium ions from reaching the anode. As a result, lithium ions are intercalated at varying rates. Multiple Li-GICs are then formed at once, giving rise to multiple phases at once (Figure 3.3a) [71]. Stress arises from the coexistence of the different phases in the material [62]. These phases cause uneven contraction and expansion of the anode, which are shown in red and purple in Figure 3.3b, that leads to cracks in the material [71]. These cracks make graphite susceptible to further damage, which is discussed in Section 3.1.2.3, leading to its deformation and fragmentation.
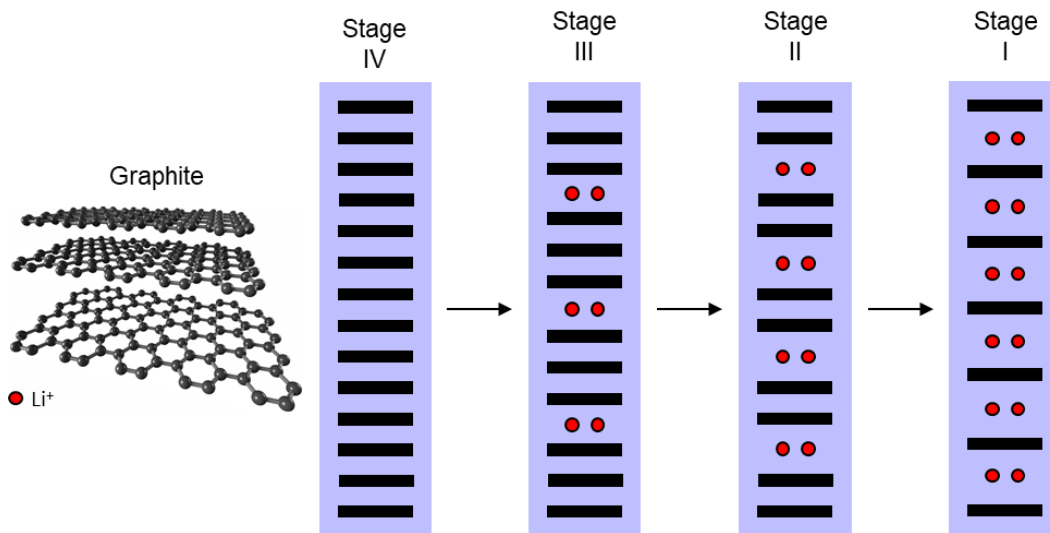
Figure 3.2. Stages of lithium-ion intercalation into graphite.
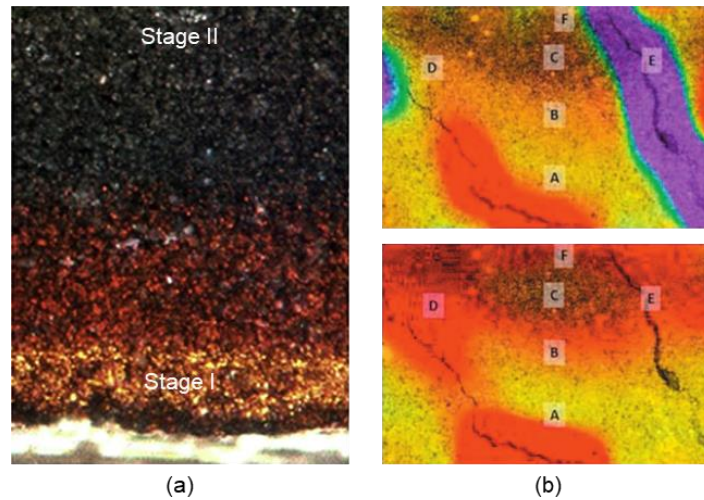
Figure 3.3. (a) Optical micrograph showing the colour changes in graphite with lithium intercalation [68] and (b) stress along tears in the graphite anode from lithiation [71].

3.1.2.2. Cathode

The cathode material in commercial LIBs has undergone far more changes over the years. Here, it is important to understand how the materials may facilitate ultra-fast charging. All commercial cathode materials are intercalation materials. They are separated by their crystal structure, which include layered, spinel, and olivine materials (Figure 3.4). LCO, NCA, and NMC are all layered materials. High rates may be achieved due their layers. Diffusion of lithium ions occur in channels created by the layers, which can allow for greater ion transport. LMO is an example of a spinel material. The structure of spinel materials favours high-rate applications. In spinel materials, lithium ions can diffuse in all directions. Since there are more pathways for lithium ion transport, more lithium ions can diffuse. LFP is an olivine material. Lithium ions can only diffuse through holes in the material. Since transport is limited in LFP, it may not be suitable for high rates.

At high rates, lithium ions may not diffuse fast enough into the electrode and rather deposit on the surface causing lithium plating.
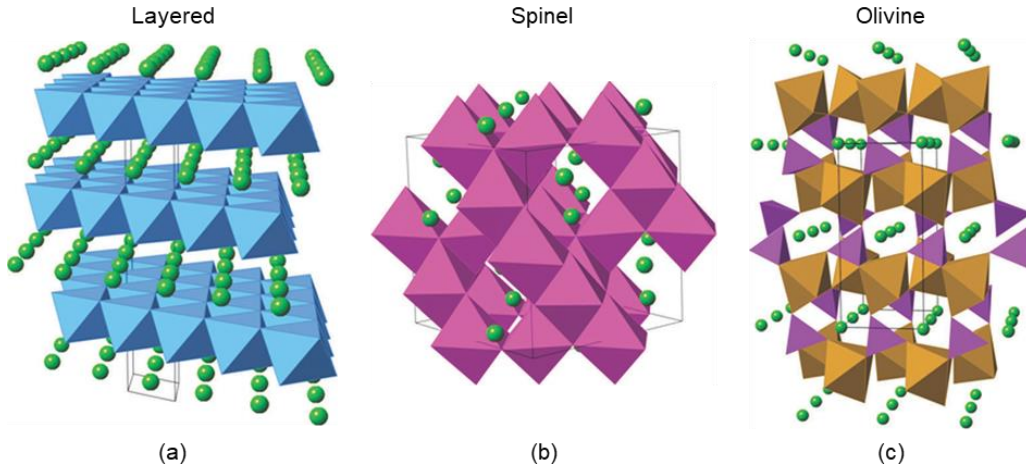
Figure 3.4. Representative structure of (a) layered, (b) spinel, and (c) olivine materials [72].

But the structure is not enough. Lithium ion transport is also affected by the material properties, which are given in Table 2.1. While LMO has the structure for ultra-fast charging, the ionic diffusivity and electrical conductivity of LMO is an order of magnitude less than LCO. For LCO, NCA, and NMC, their structural stability can impact transport. The van der Waals interaction that holds the layers together is weak and so, rapid lithium ion insertion can cause deformation of the material. And while the structure of LFP is not conducive to high lithium ion diffusion, the structural stability of LFP can help to achieve high rates. Ultra-fast charging subjects the battery electrodes to extremely harsh conditions. Since the phosphorus-oxygen bond in LFP is much stronger than the interactions in other cathode materials. It can maintain its structure during ultra-fast charging.

3.1.2.3. Electrolyte

The electrolyte composition is typically proprietary knowledge. In general, most commercial LIBs use a liquid containing lithium hexafluorophosphate ($LiPF_6$). The liquid is often ethylene carbonate (EC), propylene carbonate (PC), dimethyl carbonate (DMC), ethyl methyl carbonate (EMC), diethyl carbonate (DEC), or a combination of the above [73]. Since electrolyte permeates the cell, it is important to understand interactions between the electrolyte and other components of the cell. The electrolyte has been shown to have a large impact on performance at the electrodes [74]. As the battery is cycled, reactions at the surface of the electrode cause the electrolyte to decompose. It forms a coating on the electrodes known as the surface-electrolyte interface (SEI). The SEI is necessary as it protects the electrode from damage as lithium ions and electrons diffuse into the material [75].

Issues arise from the instability of the SEI layer. The SEI formation can cause exfoliation of the electrode. Over time, the electrolyte can cause the electrode to erode completely, causing a short. At high enough rates, there is a severe increase in the thickness of the SEI, which affects lithium ion diffusion [75]. At the electrode surface, lithium ions must compete with the electrolyte decomposition products. Lithium ions will remain on the surface of the electrode, resulting in plating and dendrite formation. Additives can be introduced to improve battery performance [76]. For example, vinylene carbonate (VC) and 2-propynyl methanesulfonate (PMS) are added to protect the anode, while 1,3-propanesultone (PS) is added to protect the cathode by forming layers between the electrodes and electrolyte [73].

3.2. Battery Temperature and Thermal Management

3.2.1. Heat Generation

Under ultra-fast charging conditions, substantial heat generation is expected. This is because LIBs are not 100% efficient. While the efficiencies of batteries are typically high under normal conditions (>99%), with ultra-fast charging, the losses are likely to be much more significant. Section 3.1 showed that the high currents associated with ultra-fast charging take a toll on the battery, which will then be less efficient. Heat generation is associated with the inefficiencies or losses in the cell. In the battery, the losses can be divided into four types:

(1) Interface: Many reactions take place at the surface of the electrodes. These reactions involve charge transfer from the electrolyte to the electrode. Lithium ions in the electrolyte have a different electrochemical potential than the lithium ions in the electrode material. The transfer from the electrolyte to the electrode has an associated energy barrier that results in energy loss, which is manifested as heat. Interface losses can account for 30% to 40% of the heat generated during cell operation [19].

(2) Transport: Lithium ions experience a fluid resistance (or drag) in the electrolyte. Poor ionic conductivity in the electrolyte results in increased drag on the lithium ions. As a result, energy is lost as lithium ions move through the electrolyte and heat is generated.

(3) Ohmic: Joule heating arises from poor electrical conductivity in the electrodes and at the junction between the electrode material and current

collector. As electrons move through the electrode, the resistances due to the poor conductivities result in heat generation. The losses are a function of current and size. For small cells, heat from the movement of electrons in the current collectors is negligible. As the size of the cell increases, the distance between the current source and cell tab increases. Since there is a larger concentration of electrons at the collector, large amounts of heat can be generated. Ohmic losses can account for 50% of the heat generated.

(4) Entropic: The insertion and removal of lithium ions causes a change of state in the electrode materials. There is an energy loss associated with the change in state. Since this change is reversible, the heat generated is also reversible. Entropic losses only account for 5% to 10% of the total heat generated [19].

3.2.2. Heat Generation Models

The performance of a battery is strongly linked to its temperature. As such, it is important to accurately quantify the heat generated in the cell and its dissipation. Many models have been proposed to predict the rate of heat generation and the response of the batteries. Here, three representative examples of heat generation models will be discussed. The aim of the heat generation model is to capture the losses in the cell that generate heat to accurately calculate the cell temperature [77]. The model by Bernardi *et al.* is most commonly used to estimate heat generation in a cell when excluding the current collectors [78]. It is derived from the first law of thermodynamics where heat is generated from electrochemical reactions, phase changes, and mixing.

$$q = -IV$$

$$-\sum_l I_l T^2 \frac{d\frac{U_{l,avg}}{T}}{dT}$$

$$+\sum_j \frac{d}{dt}\left[\int_{v_j} \sum_i c_{i,j} RT^2 \frac{\partial}{\partial T} \ln\left(\frac{\gamma_{i,j}}{\gamma_{i,j}^{avg}}\right) dv_j\right] \quad\quad (3.1)$$

$$+\sum_{j,j\neq m} \sum_i \left[\left(\Delta H_{i,j\to m}^\circ - RT^2 \frac{d}{dT} \ln\left(\frac{\gamma_{i,j}}{\gamma_{i,j}^{avg}}\right)\right)\frac{dn_{i,j}}{dt}\right]$$

The first term is the loss in the battery from electrical work. The second term gives

the entropic heating from reversible work in the cell. The third term is the heat from

mixing. Reaction rates vary in the cell and so, a concentration gradient is formed

from the mixture of species. When the gradient dissipates, heat is released. The

final term is the heat from phase changes. The expression can be simplified to:

$$q = I\left(U - V\right) - I\left(T\frac{\partial U}{\partial T}\right) \quad\quad (3.2)$$

The first term describes heat generated from cell overpotential, which results from

the ohmic losses in the cell, charge transfer at the electrodes, and mass transfer

limitations of the cell. The second term describes the entropic heat, calculated from

the change in electrical potential with respect to temperature. This change is known

as the entropic heat coefficient. This simplified model is valid if there is no heat

generated from mixing or phase changes, which means that the temperature must

be uniform in the cell.

Other heat generation models exist. The Bernadi model assumes that heat

generation is uniform and its uses an average electrode potential in the calculation. Rao and Newman show that the potential differs along the electrode [79]. They consider local heat generation in the cell. The total heat in the cell is the sum of the heat generated at cell interfaces and in the bulk material in different parts of the cell.

$$q" = -i\left(\eta_a + \Delta\phi_s\right) - \int_{x_1}^{x_2}\left(ai_n\eta_c - i_1\frac{d\phi_1}{dx} - i_2\frac{d\phi_2}{dx}\right)dx \qquad (3.3)$$

The above expression gives the rate of irreversible heat generation in a cell. It describes the overpotential and ohmic losses of the cell with respect to the length and thickness of the electrodes. An advantage of this model when compared to the simplified Bernardi model is that heat can be attributed to either overpotential or ohmic losses. Again, it assumes that there is no mixing or phase changes and that the temperature is uniform in the cell.

Kim *et al.* expands upon these models to include the current collectors. Unlike the Bernardi and Rao models, which are one dimensional, the Kim model is two dimensional. A current collector model is combined with the electrochemical model to estimate heat generation. The volumetric heat generation is calculated as,

$$q''' = i'''\left(U - V - T\frac{\partial U}{\partial T}\right) + \left(\sigma\left|\nabla\phi\right|^2\right)_{cc,pos} + \left(\sigma\left|\nabla\phi\right|^2\right)_{cc,neg} \qquad (3.4)$$

The first term gives the heat from the electrochemical reactions per unit volume. The following two terms describe joule heating from the movement of electrons in the current collectors.

3.2.3. Thermal Modeling

In literature, the two most common thermal models for a battery cell include the electro-thermal model [80]–[83] and the electrochemical model [84]–[86]; the electro-thermal model treats the battery as a lumped system where the thermal behaviour of the battery is given by an equivalent circuit, while the electrochemical model is a physics-based model that describes the underlying electrochemistry of the battery. Both models are based on the general energy balance equation,

$$Q_{cell} = mC_p\Delta T = Q_{gen} - Q_{trans} \tag{3.5}$$

$$Q_{trans} = Q_{conv} + Q_{cond} + Q_{rad} \tag{3.6}$$

Where Q_{cell} is the total heat in the cell, m is the mass of the cell, C_p is the heat capacity, and ΔT is the change temperature of the cell. The total heat in the cell is the difference in the heat generated by the cell, Q_{gen}, and the heat transferred out of the cell, Q_{trans}. Heat generation in a battery has been discussed above. Heat transfer out of the battery must now be discussed. There are three modes of heat transfer: (1) convection (Q_{conv}), (2) conduction (Q_{cond}), and (3) radiation (Q_{rad}). Convection is the transfer of heat through the movement of a fluid, e.g., air, water, coolant. Conduction is the transfer of heat through a solid such as a metal. Radiation is the transfer of heat via electromagnetic waves. The main methods of heat transfer for a battery are conduction and convection. Typically, radiation is ignored in the energy balance equation since cells are most likely found in an enclosure, which limits radiative heat transfer.

3.2.4. Experimental Thermal Behaviour

Experimental observations are key in obtaining an accurate heat generation model of a battery. The thermal behaviour of LIBs during cycling has been readily investigated in literature. For the thesis, the discussion will focus on pouch cells. In a paper by Goutam *et al.*, they investigated the surface temperature behaviour of three different pouch cells [87]. Figure 3.5 gives the results of imaging the cells during discharge at 100 A. The hottest region of the cells is shown in red where the maximum temperature is indicated. They show differences in heat generation for an LFP, NMC, and LTO cell over the discharge time. The heat generated is highly dependent on the cell. The NMC cell is the hottest, followed by the LFP cell, and then the LTO cell. But there are common patterns in the temperature distribution between the three cells. At the beginning of discharge, the hottest region appears near the positive tab. Over time, the distribution becomes more uniform where the hottest region becomes the center of the cell. Goutam *et al.* attribute the localization of heat to faster depletion of ions in the cathode due to its higher current density.

In a paper by Panchal *et al.*, the transient thermal behaviour of a pouch cell was studied [88]. Figure 3.6 shows the images taken during 4C discharge and 1C charge. At 900 seconds, the switch from discharge to charge causes the cell temperature to decrease. Calorimetric studies of LIBs demonstrate that charging is an endothermic process [89]–[91]. It is eventually overcome by the losses, which generates heat. The magnitude of heat is smaller during charge than discharge, resulting in a temperature decrease.
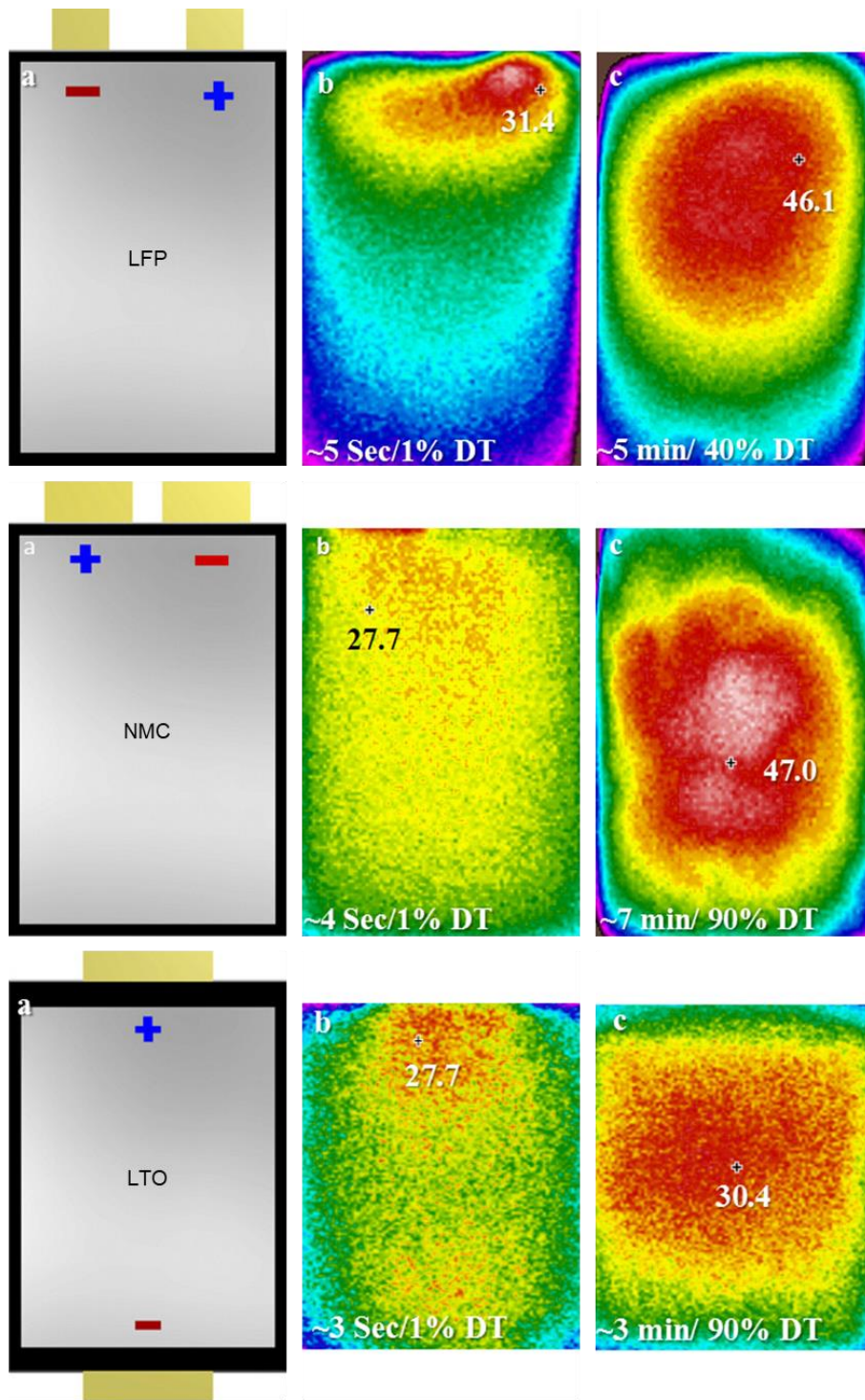
Figure 3.5. Infrared images of a 14 Ah LFP cell, a 20 Ah NMC cell, and a 5 Ah LTO cell during discharge at 100 A [87].
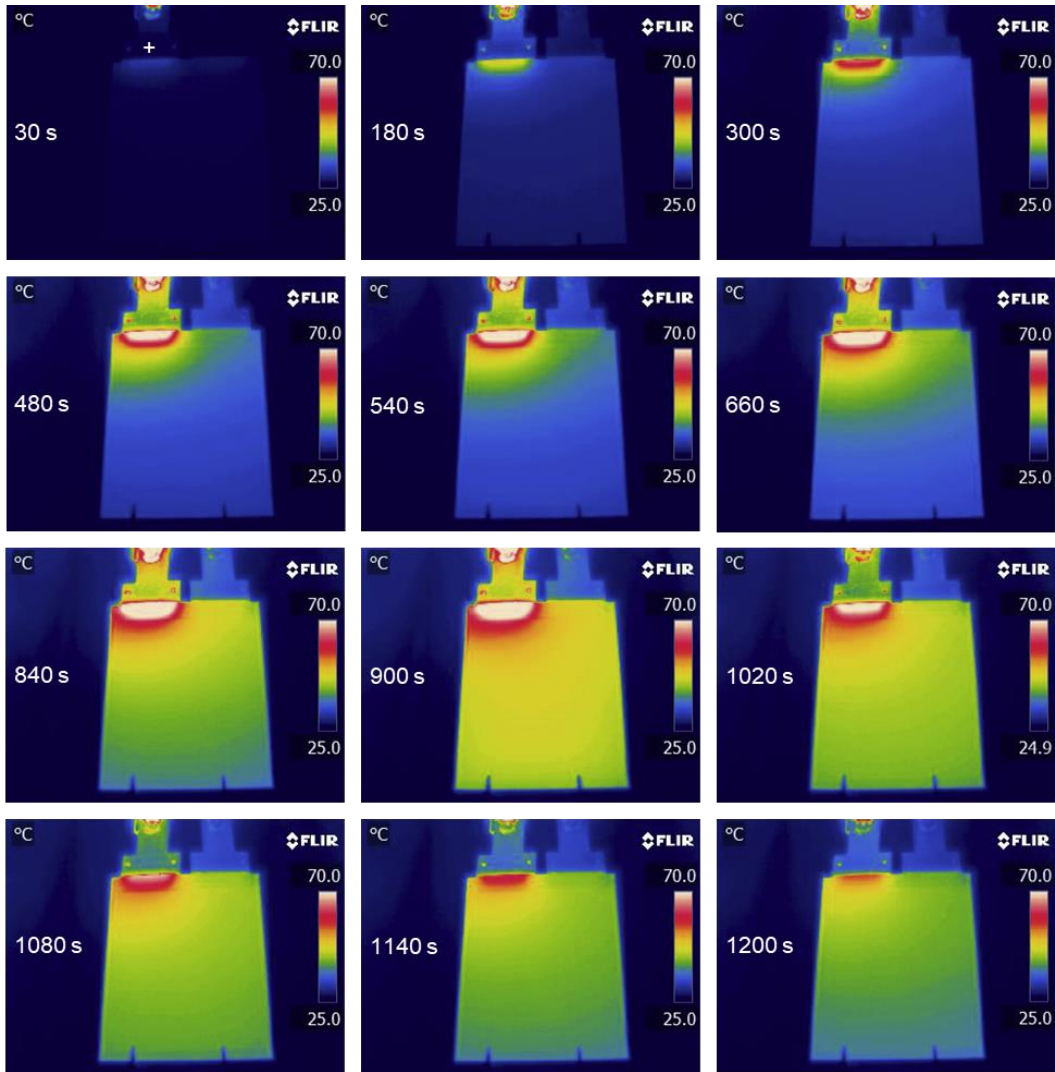
Figure 3.6. Infrared images of a 20 Ah LFP pouch cell during 4C discharge and 1C charge [88].

3.2.5. Thermal Management

The thermal management of LIBs becomes extremely important during ultra-fast charging. The high charge rates will result in large temperature rises. Elevated temperatures are linked to the degradation and destruction of the battery. Therefore, the temperature rise in LIBs must be controlled in order to maintain their proper performance and safety. Thermal management systems can be separated into

air or liquid cooling systems. In an air cooling system, air flows through the system to remove heat. In a liquid cooling system, a liquid such as water, glycol, or a refrigerant, is pumped into the system to remove heat. The systems can be further divided into active or passive cooling systems. In an active system, fans and pumps used to move the cooling medium, air or liquid, through the system to remove the heat. In a passive system, there are no fans or pumps. It relies on natural convection, conduction, and radiation to transfer the heat.

All types of thermal management systems have been used for the battery thermal management in EVs. the Nissan Leaf uses a passive, air cooling system on pouch cells (Figure 3.7a). There is no fan or pump in the system. Air flows through the openings in the battery pack enclosure to cool the batteries. The Tesla Model S uses active, liquid cooling with cylindrical cells (Figure 3.7b). A cooling tube containing glycol is placed between the cylindrical cells to cool the batteries. The Chevrolet Volt also uses an active liquid cooling system but for prismatic cells (Figure 3.7c). Aluminum plates are sandwiched between the cells. These plates contain channels in which the coolant removes heat from the cell faces.
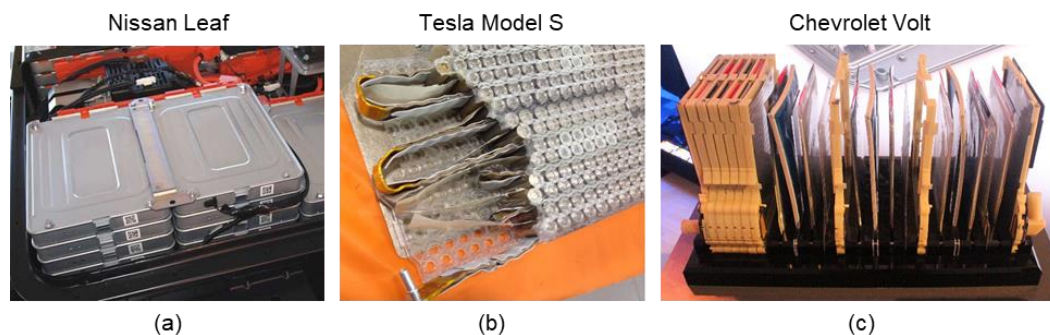
Figure 3.7. Examples of thermal management systems in EVs.

Chapter 4
Characterization and Ultra-Fast Charging

4.1. Cell Selection

Three batteries were studied (Figure 4.1). The batteries were selected for their differences in energy and power density. They cover a matrix of densities: (1) A123 LFP – medium energy density, medium power density, (2) A123 NMC – high energy density, medium power density, and (3) Turnigy – medium energy density, high power density. The charge capability of the batteries can be inferred from the power densities. As mentioned in the previous chapter, the higher the power density, the higher currents the battery can withstand. Therefore, the medium to high power densities of these cells give potential for high rates and ultra-fast charging.

The A123 LFP cell has the most mature battery technology and is well-known in industry and academia. A123 Systems has also published a design guide, which contains a comprehensive study of this cell [92]. The thermal behaviour of this cell has also been well-studied [17], [88], [93]. It will be used as a benchmark for the other cells. The A123 NMC cell, in comparison, has similar dimensions to the LFP cell but a different cathode chemistry. It uses newer battery technologies from A123 Systems and has a 37% higher energy density than the LFP cell. Since NMC is expected to perform better at high rates, it will be used to qualitatively examine the charge performance of different cathode chemistries during ultra-fast charging and their thermal behaviour. The Turnigy cell, which is typically used in

remote control (RC) vehicles, is rated for 65C discharge and 10C charge [94]. The Turnigy cell is the best high-power cell that could be obtained for the study; there are higher power cells on the market, such as the Kokam 30 Ah NMC cell, but they could not be purchased. Regardless, the Turnigy cell has two-and-a-half times the power density of the A123 cells with a comparable energy density to the A123 LFP cell, making it an excellent candidate for ultra-fast charging. The smaller size of the Turnigy cell also has unique implications in thermal management and packaging. It will be used to study the impact of cell size for application in a battery pack.
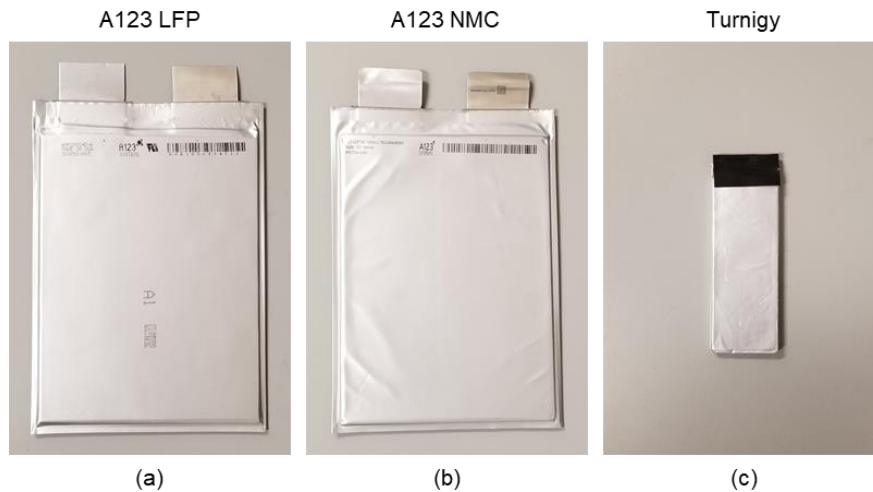
Figure 4.1. Batteries selected for ultra-fast charging: (a) A123 LFP, (b) A123 NMC, and (c) Turnigy cell.

4.2. Cell Specifications

Specifications for the batteries are listed in Table 4.1. Specific differences between the batteries can be highlighted from the table. The first difference is the cell size. The Turnigy cell is one-fifth of the size of the A123 cells. This means that there is more flexibility in packaging compared to a large cell. However, more cells

are needed due to its lower capacity. It is also 20% thicker with 82% less surface area on the face of the cell. Heat will be dissipated very differently than the larger but thinner A123 cells. The second difference is the chemistry. As indicated earlier, the A123 cells have two different chemistries, LFP and NMC. LFP is known to have rate limitations. Yet LFP is a much more stable material than NMC, which may enable ultra-fast charging. Conversely, NMC has achieved high rates in the laboratory [14]. But in commercial cells, the rate capability of NMC has not been fully investigated. And the chemistry for the Turnigy cell is not specified. Based on the voltage range of the cell and its nominal voltage, it is assumed that the chemistry is either NMC or NCA. The third difference is the energy and power density. The A123 LFP cell is a well-known power cell. It, however, has the lowest energy and power density at 131 Wh/kg and 1600 W/kg, respectively. This can be attributed to the older chemistry as well as manufacturing methods. Between the two newer batteries, the A123 NMC cell has the higher energy density at 180 Wh/kg. The Turnigy cell has the higher power density at 8000 W/kg.

Table 4.1. Specifications for the selected batteries.

	A123 LFP	A123 NMC	Turnigy
Dimensions (mm)	$w = 160$ $h = 227$ $t = 7.25$	$w = 161$ $h = 227$ $t = 7.5$	$w = 49.4$ $h = 135$ $t = 9$
Mass (kg)	0.496	0.55	0.14
Cathode Chemistry	LFP	NMC	NMC/NCA[a]
Rated Capacity (Ah)	20	26	5
Nominal Voltage (V)	3.3	3.7	3.8
Nominal Resistance (mΩ)	2.6	2.7	2.9
Gravimetric Energy Density (Wh/kg)	131	180	136
Gravimetric Power Density (W/kg)	1600	2500	8000

[a]Not specified on data sheet

4.3. Cell Characterization

The USABC Battery Test Procedures Manual was used in the characterization of the batteries [95]. The hybrid pulse power characterization (HPPC) test was used to obtain the open circuit voltage (OCV), resistance, and pulse power capabilities of the batteries. The test consists of a series of charge and discharge pulses from 100% to 0% SOC (Figure 4.2a). At each SOC point, there is a 10-second 1C discharge pulse, followed by a 10-second pause, and then a 10-second 1C charge pulse. There is then a pause for 30 seconds where the discharge and charge pulses are repeated for 2.5C and 5C. After another 30-second pause, the cell is discharged to the next SOC point and allowed to rest for one hour. The process is then repeated for the SOC range. The 1C values are used in the characterization.
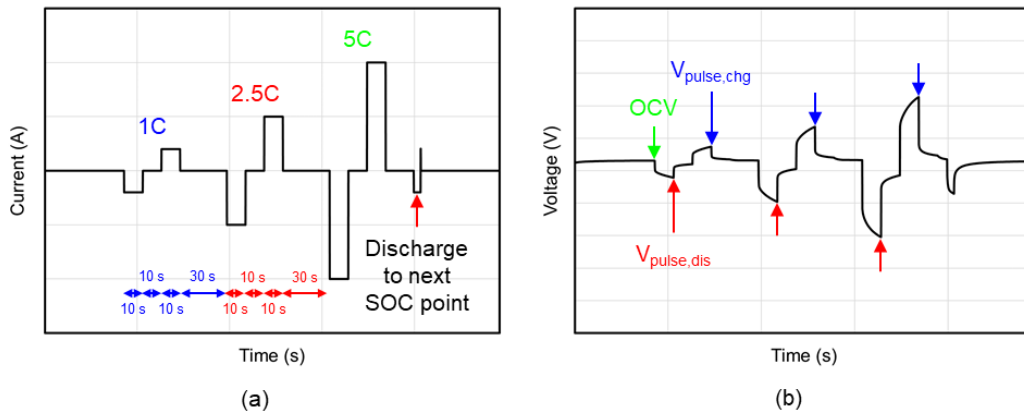
Figure 4.2. HPPC test: (a) current and (b) voltage.

The cell resistance during charge and discharge are then,

$$R_{chg} = \frac{\max\left(V_{pulse,chg}\right) - OCV}{\left|I_{pulse,chg}\right|} \tag{4.1}$$

$$R_{dis} = \frac{OCV - \min\left(V_{pulse,dis}\right)}{\left|I_{pulse,dis}\right|} \tag{4.2}$$

The OCV at each SOC point is chosen as the voltage before the first discharge pulse, as shown by the green arrow in Figure 4.2b. The maximum voltage from the charge pulse and the minimum voltage from the discharge pulse for the calculation are indicated by the red and blue arrows in Figure 4.2b. The resistances are shown in Figure 4.3. The pulse power capabilities for each battery are,

$$P_{chg} = \frac{V_{\max} \times \left[V_{\max} - OCV\right]}{R_{chg}} \tag{4.3}$$

$$P_{dis} = \frac{V_{\min} \times \left[OCV - V_{\min}\right]}{R_{dis}} \tag{4.4}$$

They were calculated over the entire SOC range from the OCV and calculated cell resistances (Figure 4.3). The maximum and minimum voltage in the calculation is defined by the maximum and minimum in their operating voltage ranges. For the A123 LFP cell, these values are 3.7 V and 2.0 V. For the A123 NMC and Turnigy cells, the voltages used in the calculation are 2.8 V and 4.2 V.

A comparison of the battery characterization results is shown in Figure 4.3. A123 NMC cell has the lowest cell discharge resistances over the entire SOC range. The A123 LFP and Turnigy cells have lower and similar discharge resistances, which increase sharply at low SOC. The difference in the cell charge resistances is much smaller. The resistance for the A123 LFP cell ranges from 2.1 mΩ to 2.5 mΩ,

the A123 NMC cell ranges from 2.4 mΩ to 2.6 mΩ, and the Turnigy cell ranges from 2.4 mΩ to 2.7 mΩ. The A123 NMC cell also has the highest pulse power capability during both discharge and charge, at 1.8 kW for 100% SOC and 1.2 kW at 5% SOC, respectively. The Turnigy cell has a similar pulse power capability, but its capability drops more quickly with decreasing SOC. The pulse power capability is important in predicting how a battery will perform during ultra-fast charging; it determines how much energy is used or gained for a specific power output or input. Thus, the A123 NMC and Turnigy cells can be charged at a faster rate because of the higher power capability.
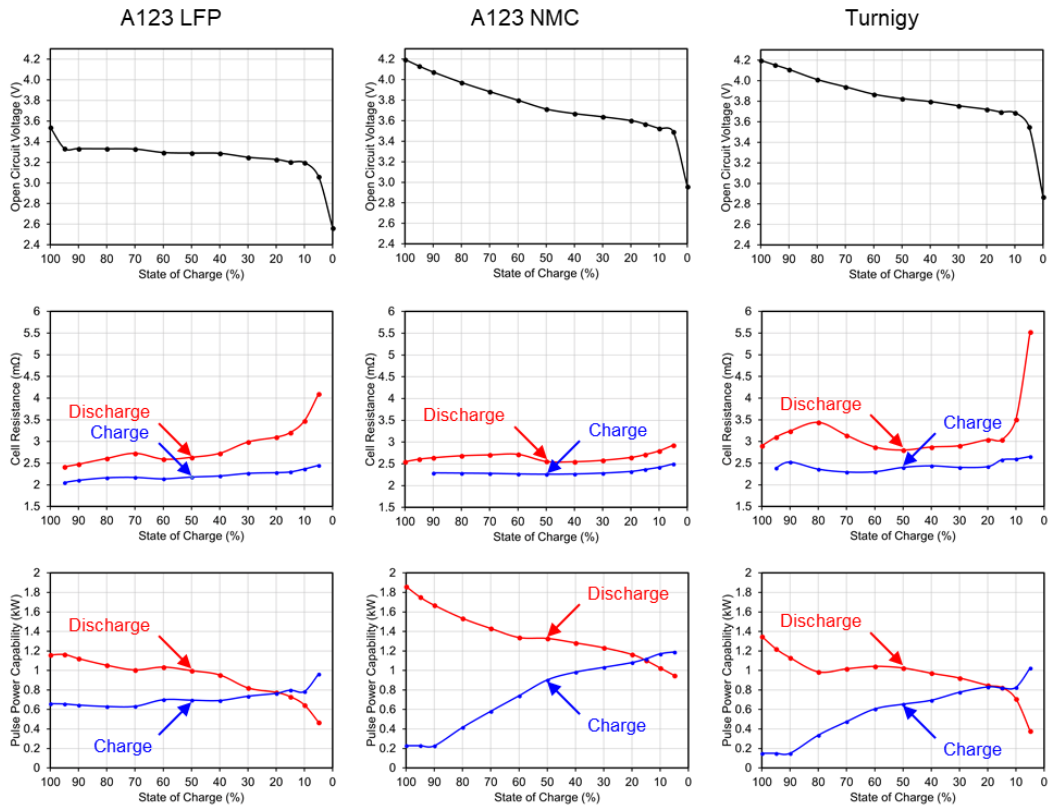
Figure 4.3. HPPC test results: open circuit voltage, cell resistance, and pulse power capability.

4.4. Experimental Battery Performance During Charging

4.4.1. Test Fixture

The A123 and Turnigy cells were tested in the fixtures shown in Figure 4.4. Since the batteries would charged above their rated current, expansion of the cells was of great concern. The purpose of the fixtures was to maintain uniform pressure on the cells during cycling. This was done to ensure the safety and longevity of the batteries. Recommendations from the A123 design guide for the A123 LFP cell were used to build the fixture [92]. In the fixture, cells are compressed using springs with two aluminum plates (Figure 4.4a). Approximately 3–4 psi is applied to the cells. For the Turnigy cell, the two acrylic plates provided with the original pack from which the cell was obtained was compressed with heat shrink (Figure 4.4b).

A123

(a)

Turnigy

(b)
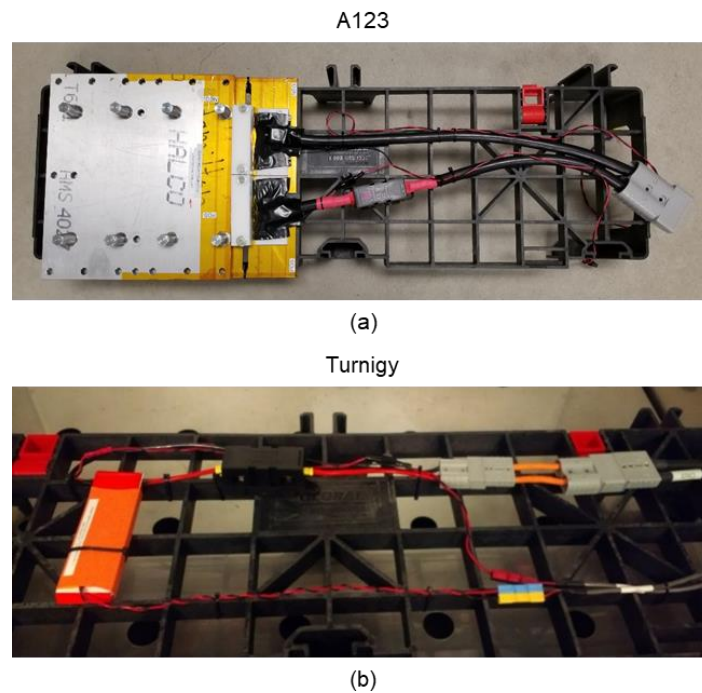
Figure 4.4. Test fixture for (a) A123 and (b) Turnigy cells.

4.4.2. Charge Protocol

The batteries were charged at a series of increasing rates of charge, up to limits of the cells (Table 4.2). The testing was performed with parallel-connected, 75 A, 0–5 V, 0.1% accuracy channels of a Digatron Power Electronics Universal Battery Tester system. Prior to each charge, each cell was discharged slowly at a rate of C/2 until a voltage cut-off, which correlates to about 10% SOC (3.2 V for the A123 LFP cell, 3.5 V for the A123 NMC and Turnigy cells). After a 30-minute rest period, the cell was charged using a constant current/constant voltage (CCCV) profile at the desired C-rate until the constant upper voltage limit is reached (3.6 V for the A123 LFP cell, 4.2 V for the A123 NMC and Turnigy cells) and the current has reduced to less than 0.1 A (Figure 4.5). Following another 30-minute rest period, the discharge and charge steps are repeated for a second time at the same rate so that a charge efficiency can be calculated. The entire process is then repeated over the desired charge-rate range.
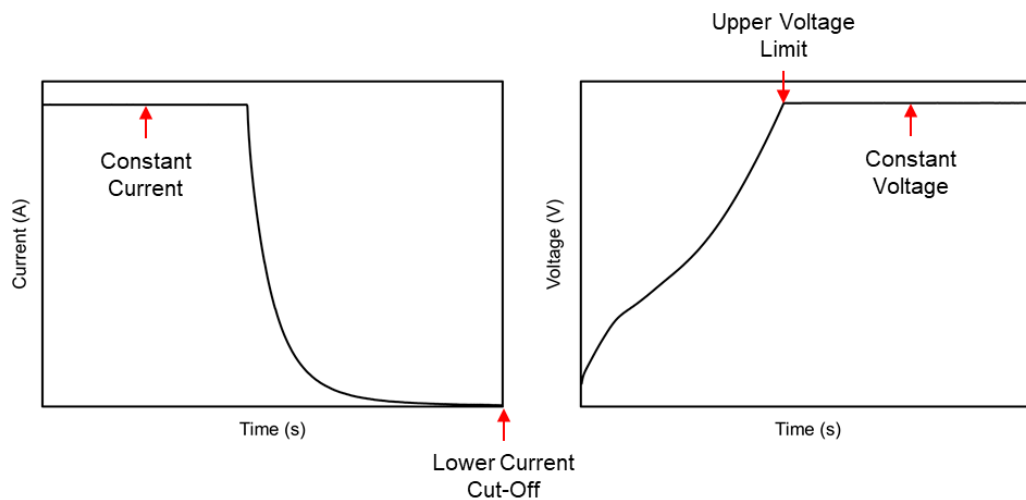
Figure 4.5. Representation of constant current, constant voltage charging.

Table 4.2. Charge protocol for the batteries over the charge-rate range.

Step	Action	Step End
1	Pause	After 5 seconds
2	0.5C Discharge	< 3.2 V (A123 LFP)
		< 3.5 V (A123 NMC, Turnigy)
3	Pause	After 30 minutes
4	CCCV Charge @ xC	> 3.6 V (A123 LFP)
		> 4.2 V (A123 NMC, Turnigy)
		< 0.1 A
5	Pause	After 30 minutes
6	0.5C Discharge	< 3.2 V (A123 LFP)
		< 3.5 V (A123 NMC, Turnigy)
7	Pause	After 30 minutes
8	CCCV Charge @ xC	> 3.6 V (A123 LFP)
		> 4.2 V (A123 NMC, Turnigy)
		< 0.1 A
9	Pause	After 30 minutes
10	0.5C Discharge	< 3.2 V (A123 LFP)
		< 3.5 V (A123 NMC, Turnigy)
11	Pause	After 30 minutes
12	Repeat 1–11	For 1C–6C (A123 LFP and NMC)
		For 1C, 2C, 4C, 6C, 8C, 10C (Turnigy)

4.4.3. Charging Results

The A123 LFP and NMC cells were charged from 1C to 6C, above their rated limit of 4C charge. The Turnigy cell was charged from 1C up to its rated limit of 10C charge. At 1C charge, all three batteries spend most of the charge time in the constant current part (Figure 4.6). Heat is generated during the constant current part, as shown by the increase in temperature of the batteries during the constant current part and the decrease in temperature of following the start of the constant voltage part. Since different fixtures were used for the A123 and Turnigy cells, the measured temperature is used for qualitative purposes only. The A123 NMC cell generates more loss for given C-rate than the A123 LFP cell, resulting in higher temperatures, as has been observed in literature [87]. For the Turnigy cell, there is

an initial decrease in temperature during charging that eventually increases, starting around 1000 seconds (Figure 4.6b). The endothermic nature of the charge reaction is evident here. Cooling from the charge reaction, i.e., the migration of lithium ions back from the cathode material (LFP and NMC) to graphite, is not overcome by the losses associated with charging, especially the interface and ohmic losses. Overall, the cell peak temperatures are within the acceptable range (typically 0°C to 45°C).
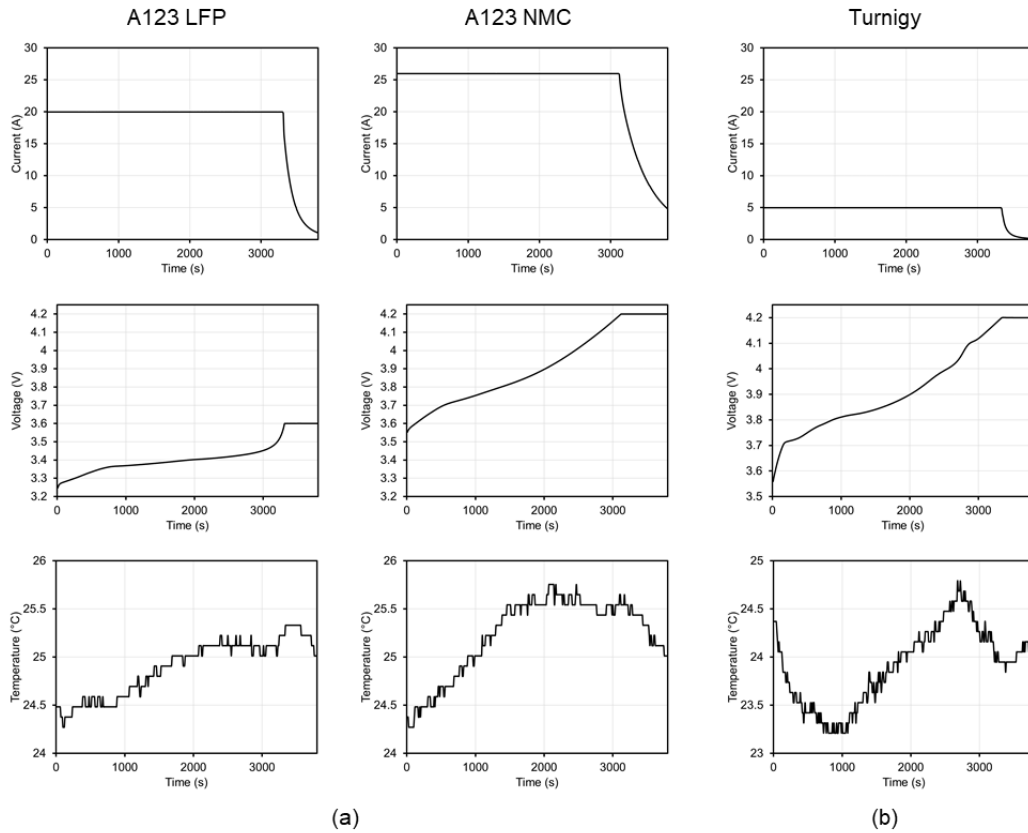
Figure 4.6. Results from batteries during 1C charge: (a) A123 cells and (b) Turnigy cell.

Similar results for the batteries are observed during 4C charge (Figure 4.7). But here, the charge time is now split between the constant current part and the

constant voltage part. The switch from constant current to constant voltage occurs at 600 seconds rather than 3000 seconds during 1C charge. The higher charge rate also means more heat is generated. The A123 NMC cell sees the largest increase in the peak temperature from 26°C to 34°C (Figure 4.7a). The endothermic reaction is also still present in the charging of the Turnigy cell (Figure 4.7b).
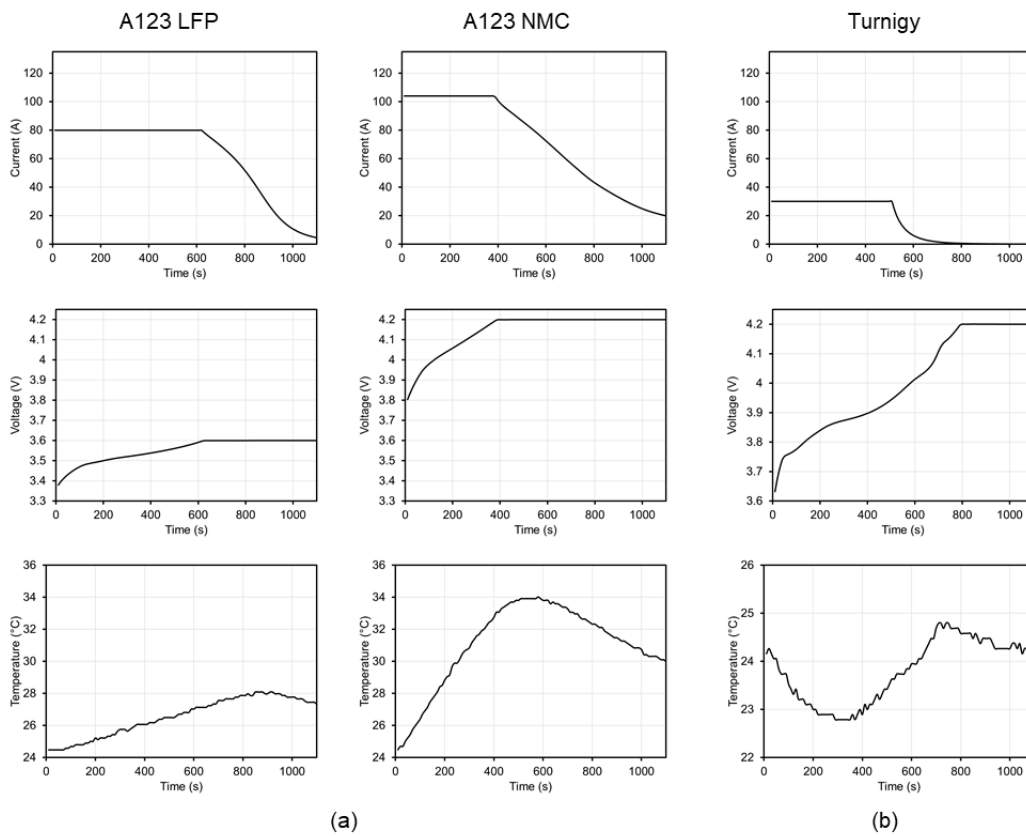
Figure 4.7. Results from batteries during 4C charge: (a) A123 cells and (b) Turnigy cell.

4.4.4. Charge Performance

Results from charging are shown in Figure 4.8. The performance of the cells during ultra-fast charging is determined using four criteria: (1) the charge time of

the cell to 80% SOC, (2) the charge efficiency of the cell, (3) the calculated charge loss from the cell, and (4) the peak temperature of the cell measured during charging. Ultra-fast charging is achieved with a charge time of less than 15 minutes. A high charge efficiency (>95%) is also required for the application of the batteries in the ultra-fast charging of electric vehicles. The charge efficiency is associated with the charge loss and temperature. A lower efficiency means an increase in loss, resulting in a higher peak temperature. Maintaining the temperature of the cell within its optimal range is critical in the health and safety of the battery.
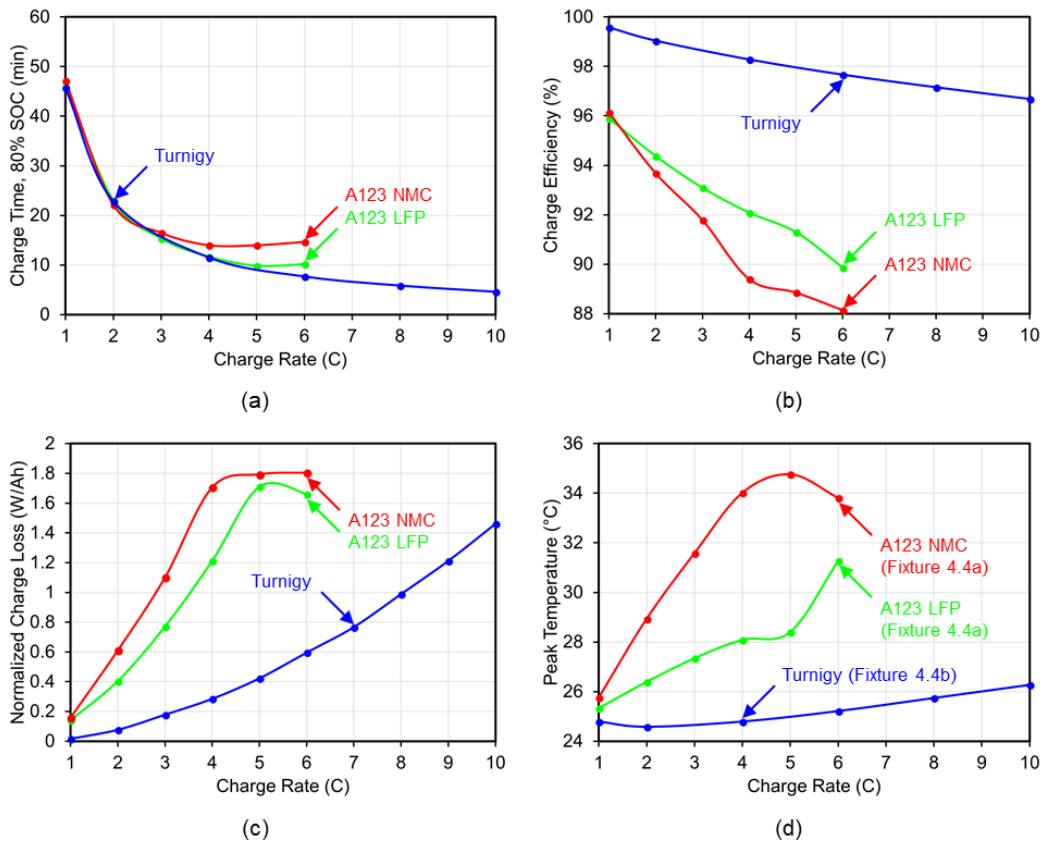
Figure 4.8. Charge performance of the batteries: (a) charge time to 80% SOC, (b) charge efficiency, (c) charge loss, and (d) peak temperature: fixture in Figure 4.4a used for the A123 cells and fixture in Figure 4.4b used for the Turnigy cell.

4.4.5. Charge Time

Charge times of less than 15 minutes to 80% SOC were achieved for all three batteries. In fact, the Turnigy cell was able to achieve a charge time of less than five minutes. However, as mentioned earlier, charging is limited in the A123 LFP and NMC cells. The maximum charge rate for the LFP cell is limited to 5C and a charge time of around 10 minutes to 80% SOC. The charge rate for the NMC cell saturates at 4C with a charge time of 14 minutes to 80% SOC. These results show that the batteries are capable of ultra-fast charging, but the cell resistance will limit the charge time when the charge rate is high enough.

The kinetic differences in the three batteries may explain the charge rate limitations or lack thereof. The Turnigy cell is much smaller than the A123 cells but it has a higher density. It is likely then that there are more electrode layers in the cell and they are thinner than ones in the A123 cells. It has been shown that the charge time for an LIB can be reduced with thinner electrodes [96]. This is because thinner electrodes increase the diffusion rate. Combined with a lower magnitude of current, the Turnigy cell can achieve much higher rates.

The two A123 cells are expected to have thicker layers, resulting in lower diffusion rates. At 5C and 4C charge for the A123 LFP and NMC cell, the diffusion rate of lithium ions and electrons into the electrodes cannot keep up with the rate at which electrons are forced into the cathode and lithium ions are generated. As a result, lithium ions and electrons remain on the surface of the anode and current collector. The cell resistance increases, resulting in limits to the power and rates

during charging. The difference in the charge limits between the LFP and NMC cell are most likely due to the stability of the LFP material. While NMC is expected to facilitate faster kinetics, LFP is better able to withstand the higher charge rates.

4.4.6. Charge Efficiency

The charge/discharge cycle is repeated twice at each charge rate to allow accurate calculation of the charge efficiency and loss, which are calculated from the second cycle. The charge efficiency is defined as,

$$\eta_{chg} = \frac{E_{dis} + E_{dis,loss}}{E_{chg}} \tag{4.5}$$

Where E_{dis} is the measured discharge energy, E_{chg} is the measured charge energy, and $E_{dis,loss}$ is the estimated energy loss during discharge. It describes how much energy is removed from the cell during the discharge step and then put back into the cell during the charge step. The discharge steps were performed at a slow rate to minimize the impact of discharge loss on the efficiency calculation. But loss still occurs during discharge, and it is assumed to be one-fifth of the total loss for the C/2 discharge/1C charge cycle. The loss is added to the experimental value to give the total discharge energy.

The charge efficiency for the Turnigy cell is very high, ranging from 99.6% at the 1C charge rate to 96.6% at the 10C charge rate. The A123 cells have lower efficiencies, ranging from approximately 96% at the 1C charge rate for both cells to 91.3% and 88.9% at the 5C charge rate for the LFP and NMC cell, respectively.

The performance of the A123 NMC quickly drops with charge rate. Consequently, the A123 LFP and NMC cell may not be appropriate for ultra-fast charging as almost 10% of the energy from the charge is lost as heat.

4.4.7. Charge Loss

The average charge loss, $P_{chg,loss}$, is calculated from the charge tests and used as the input for the steady-state thermal analysis. It is defined as the average loss until 80% SOC is reached and is calculated by dividing the charge loss energy, which occurs up until 80% SOC, by the time to reach 80% SOC. The calculated charge loss extrapolated or interpolated to all charge rates from 1C to 10C and normalized by the cell capacity is given in Figure 4.8c. Since the batteries differ in capacity, the charge loss is normalized to enable a direct comparison.

The Turnigy cell has, by far, the lowest loss with the A123 LFP cell having about four times the loss and the A123 NMC cell having about six times the loss. As previously mentioned, the charge rate for the NMC cell quickly saturates for rates beyond 4C. Once charging reaches the 5C rate, the constant current part of the charge is very short, with only a duration of two minutes or less. This results in similar charge times and loss values for the 4C and 5C charges.

For the A123 LFP cell, there is a decrease in the loss from 5C to 6C charge, but the charge time remains the same. At 5C charge, the constant current part lasts 360 seconds. At 6C charge, the constant current part is only 20 seconds long. Since loss occurs during the constant current part, the loss generated at 6C charge over time is much less, even with the higher current magnitude at 6C charge.

4.4.8. Peak Temperature

All of the temperatures are within the acceptable operating range of the batteries. As previously mentioned, the measurements are qualitative as different test fixtures were used. The peak temperatures, shown in Figure 4.8d, for the most part, match the calculated charge losses. The A123 NMC cell has the greatest loss and is, therefore the hottest. The Turnigy cell is the coolest. There is one exception to the trend, charging the A123 LFP cell at 6C. The charge loss at 6C is less than the loss at 5C, but the peak temperature is much greater. The heat must be generated from the entropic losses, which are reversible and not seen in the charge efficiency. There must be significant changes in states and phases occurring in the electrodes, which is indicative of the rate mismatch between lithium ion generation and diffusion, which leads to electrode deformation.

4.5. Conclusions

In conclusion, charge times less than 15 minutes were achieved for the three batteries. The charge efficiency remained high for the Turnigy cell (>95%) but dropped quickly for the A123 cells (<90%). The impact of chemistry and size were identified in the charge time and loss. The A123 LFP and NMC cells experienced limits to charging at rates higher than 4C. The LFP cell achieved faster charge rates than the NMC cell. The limits can be rationalized by mismatches in transport rates and the better stability in the LFP electr. The smaller size of the Turnigy cell, both in capacity and dimensions, enabled higher charge rates. Therefore, the Turnigy cell appears to be the most viable option for ultra-fast charging.

Chapter 5
Thermal Analysis

5.1. Model Design

Thermal analysis of the batteries during ultra-fast charging was performed using finite element analysis (FEA) software, ANSYS. The batteries were modeled in a cooling apparatus to determine their thermal management requirements, i.e., how effectively must the loss be removed from the cell for a desired temperature rise. The apparatus modeled in ANSYS was inspired by the thermal management system for the battery pack in the Chevrolet Bolt (Figure 5.1). In the Bolt, cells are cooled using aluminum plates placed on the face of the cells, which are connected to an active liquid cooling plate located at the bottom of the pack [97]. The cells are grouped in three; an aluminum plate is placed between every two cells.

In the model, three cells are sandwiched between four aluminum plates and attached to cooling plates found on either side of the cells. The outer aluminum plates are used to ensure uniform cooling (Figure 5.2). The cooling plates are set to a fixed temperature of 20°C; all other surfaces are assumed to be perfectly insulated. For the sake of computational simplicity, fixed-temperature cooling plates are used. In practice, the cooling plates can be air-cooled heat sinks or liquid-cooled cold plates. And to provide a fair comparison of the A123 cells to the Turnigy cell, which has a much smaller capacity, five Turnigy cells, for a total of 15 cells in the apparatus, are modeled together to achieve a stored energy similar to the A123 cells.
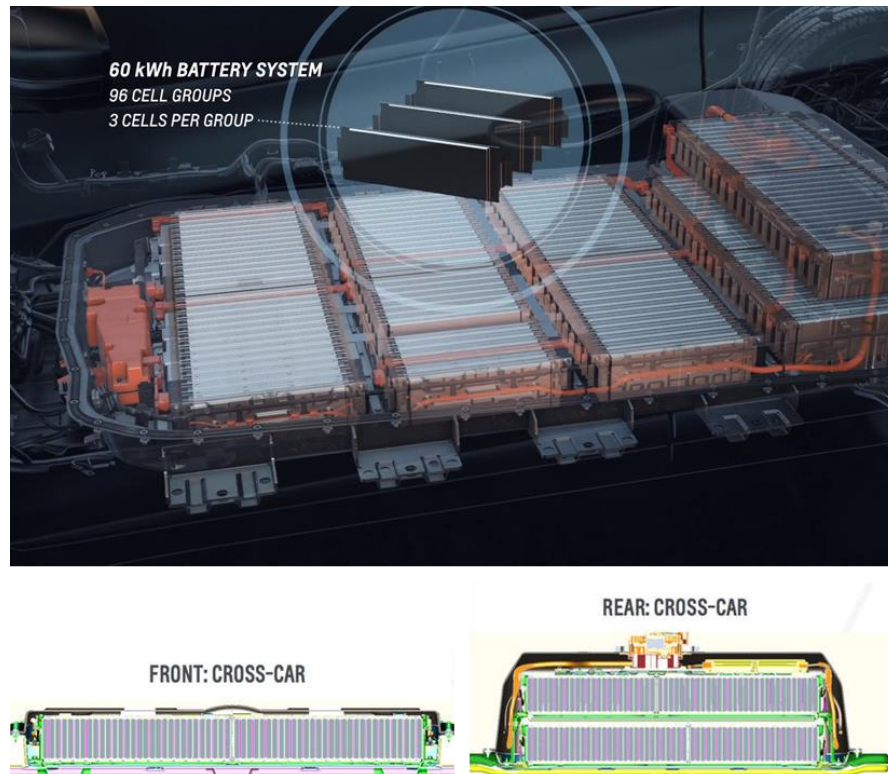
Figure 5.1. Thermal management system for the Chevrolet Bolt [97].

Dimensions for the aluminum plates are based on the dimensions of the cell. The height of the plate is given by the height of the cell. The width of the aluminum plate is 20 mm longer than the width of the cell so that there is a 10 mm overhang on either side of the cell. And the thickness of the plate is varied relative to the thickness of the cell. The variable *p* describes the percentage of the cell thickness that is used for the plate. It has been normalized to the cell for later discussion of packaging in a battery pack. Four plate thicknesses, including 10%, 25%, 50%, and 100% of the cell thickness, were investigated. The thicker the aluminum plates, the more effectively loss can be removed from the cells, resulting in a lower rise; more heat is conducted through the aluminum plates to the cooling plates on the ends.
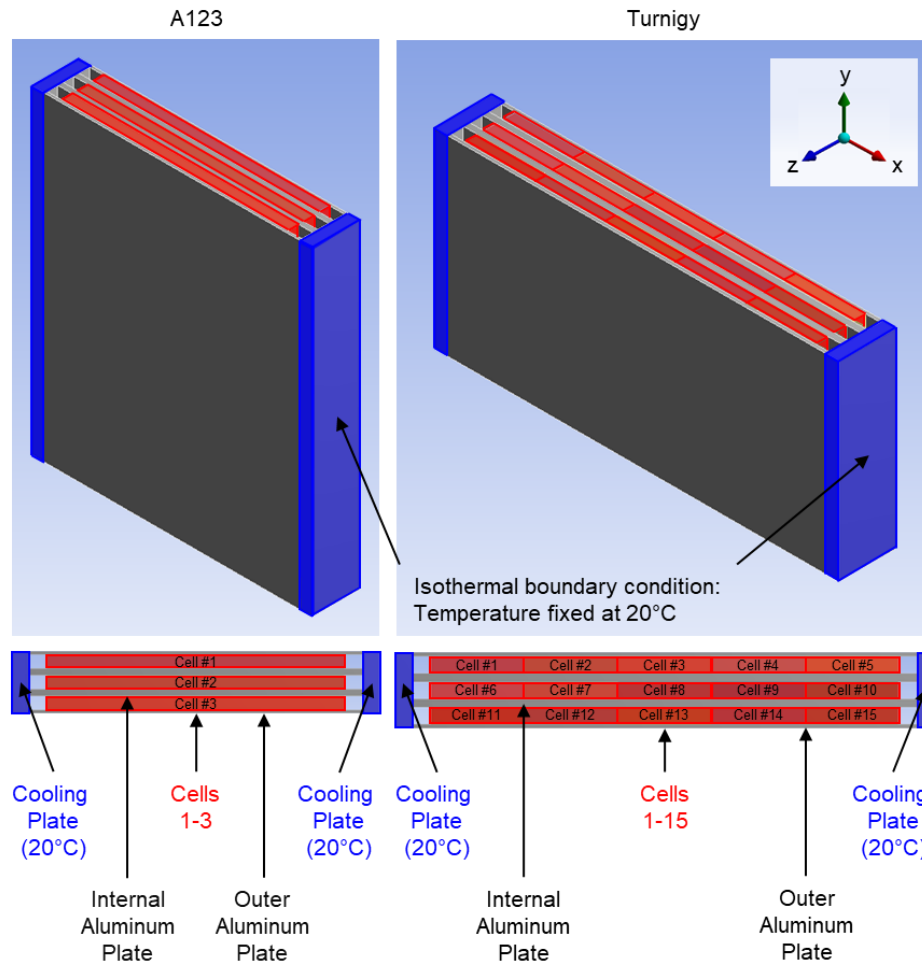
Figure 5.2. Model for the thermal analysis of the batteries.

5.2. Model Reduction

In a thermal analysis, a symmetric boundary condition means that there are no out-of-plane displacements and in-plane rotations. There are three symmetry planes in the model that satisfy these conditions, as shown in Figure 5.3. Heat is equally transferred to both sides of the cell via the two cooling plates and all other surfaces are insulated. These planes can be used to dimensionally reduce the model to an eighth of its original size, which significantly reduces its computational time.
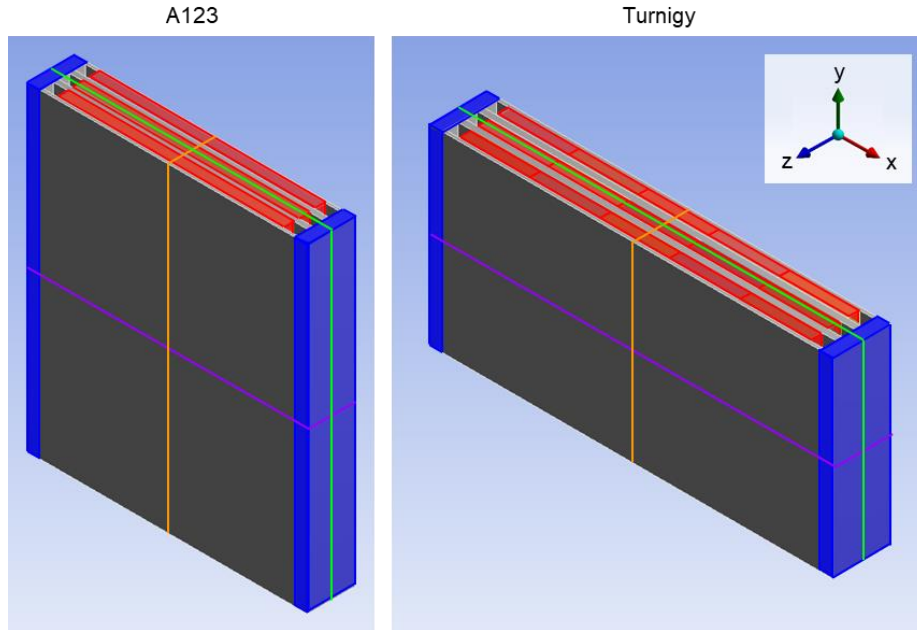
Figure 5.3. Symmetry planes for model reduction in the thermal analysis.

5.3. Thermal Properties

For steady-state thermal analysis, only the battery thermal conductivity is needed. It calculates a temperature rise for a given loss and so, only knowledge about how heat is removed the system is needed. The density (σ) and heat capacity of the batteries are needed in the transient thermal analysis as it considers the impact of the cell's thermal mass on the temperature rise over time. Thermal properties for the materials are listed in Table 5.1. Aluminum values were obtained from ANSYS. The heat capacity and thermal conductivity (κ) for the A123 LFP cell were obtained from [1] and [2], respectively. Values for the A123 NMC and Turnigy cell were based on values from [99]. The thermal properties are calculated as,

$$C_{p,cell} = \frac{\sigma_{cell}}{\sigma_{literature}} \times C_{p,literature} \tag{5.1}$$

$$\kappa_{cell} = \frac{\sigma_{cell}}{\sigma_{literature}} \times \kappa_{literature} \tag{5.2}$$

Table 5.1. Thermal properties of the materials used in the thermal analysis.

Material	Density (kg/m³)	Heat Capacity (J/kg·K)	Thermal Conductivity (W/m·K)	
			In-Plane (x, y)	Through-Plane (z)
A123 LFP	1884	610	16.4	0.51
A123 NMC	2007	885	23.3	1.15
Turnigy	2333	1029	27.1	1.31
Aluminum[a]	2689	951	237.5	

5.4. Steady-State Thermal Analysis

A steady-state thermal analysis was performed to determine the temperature rise and distribution for the batteries given a specific plate thickness. Average loss from the charge tests were used as an input. The results of the analysis were used to compare the charge performance of the batteries with respect to their thermal behaviour. There are trade-offs in achieving a certain charge rate and obtaining a certain temperature rise. The results were also used to elucidate the impact of the thermal management system on the packaging of the batteries for a battery pack. The volume and mass of a pack are points of contention during the design process. Thicker plates mean increased volume and mass, and so, less cells can be packaged.

5.4.1. Temperature Rise and Distribution

The modeled temperature rise for the batteries at different charge rates and aluminum plate thicknesses is shown in Figure 5.4. The figure, for example, shows that for the Turnigy cell, a 15°C rise will occur for 9C charge with an internal plate that is 25% of the cell thickness and for 7C charge with a plate that is 10% of the

cell thickness. Since the charge rate of the A123 NMC cell does not actually increase beyond the 4C charge rate, the temperature rise for the battery asymptotes at 4C charge. Any plate thickness greater than 10% of the cell thickness will keep the temperature rise below 15°C. Complications arise from the A123 LFP cell. The charge capability of the cell decreases after 5C charge, but the extent of the decrease is unknown. Any plate thickness greater than 10% of the cell thickness will have a temperature rise below 15°C. For the plate that is 10% of the cell thickness, it may be possible to achieve a charge rate higher than 4C for a temperature rise of 15°C, but further testing is required.
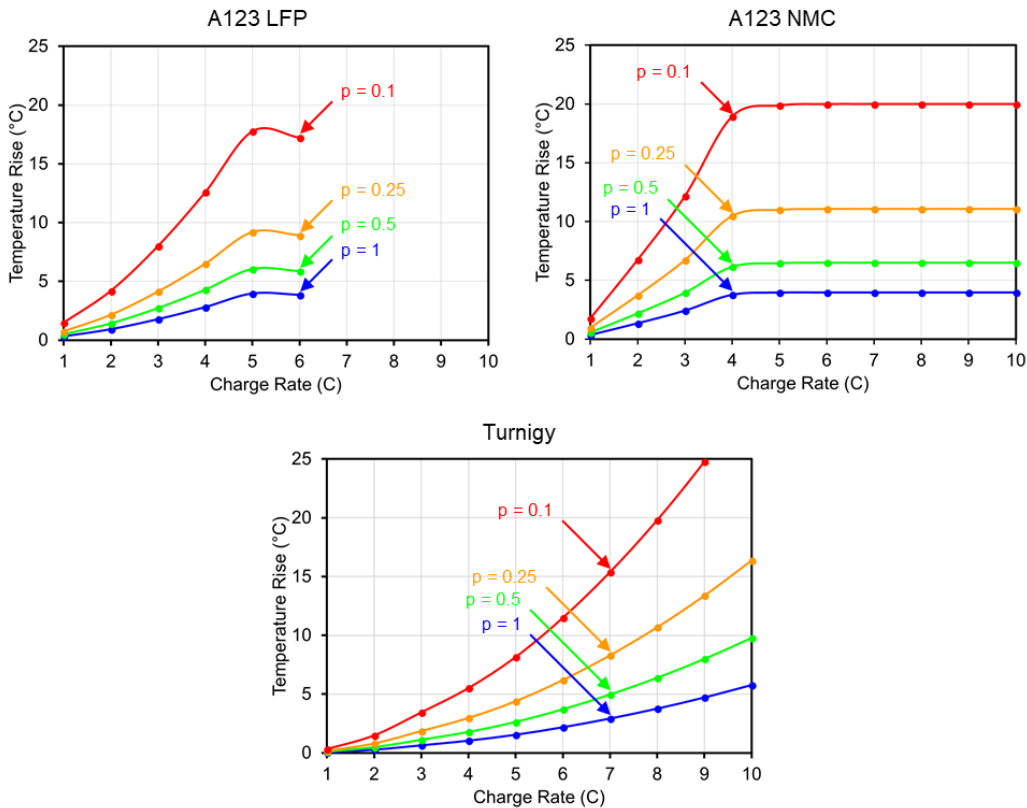
Figure 5.4. Modeled temperature rises obtained from the steady-state thermal analysis of the batteries with different plate thicknesses.

The simulated temperature distribution of the cells at 4C charge (ultra-fast charging conditions) with different plate thicknesses is shown in Figure 5.5. Since the through-plane thermal conductivity for the batteries is an order of magnitude smaller than the in-plane, heat at the center of the cells cannot be as easily removed. With thinner aluminum plates, less heat can be transferred to the cooling plates at the ends, resulting in higher temperatures overall. At the cell centers, this is even more prominent as heat is generated faster than what can be removed. Thicker cooling plates more effectively transfer heat out through the cooling plates, but it comes at the cost of increased volume and weight when used in a battery pack.
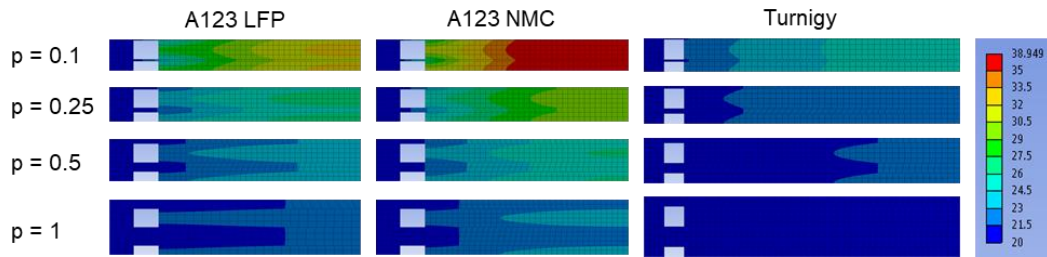
Figure 5.5. Simulated temperature distribution from the steady-state analysis of the batteries during 4C charge with different plate thicknesses.

5.4.2. Effective Energy Density

The thermal management system impacts the mass and volume of a battery pack, which, in turn, affects how much energy can be stored in the pack for a given volume and mass. The effective energy density takes into account the increased mass and volume of the battery from the aluminum plate required to cool it. It is calculated by dividing the total energy in a cell by the sum of the plate and cell mass or volume. And this enables a direct comparison of the thermal management

requirements for the batteries and their performance in a pack.

The effective energy density for the different plate thicknesses are shown in Figure 5.6. The figure shows that the aluminum plates used in the cooling apparatus have a large impact on the battery's energy density. For example, the gravimetric energy density for the A123 NMC cell decreases by 13% with the addition of a plate that is 10% cell thickness. With a plate that is 100% of the cell thickness, the effective energy density decreases by 60%, which means that for a desired pack mass, 60% less energy can be stored. Likewise, the volumetric energy density decreases by 10% using the 10% cell thickness plate. The 100% cell thickness plate decreases the energy density by 47%. Thus, in a pack with volume constraints, 47% less energy can be loaded into the pack. The same phenomenon is seen for the A123 LFP cell and the Turnigy cell.
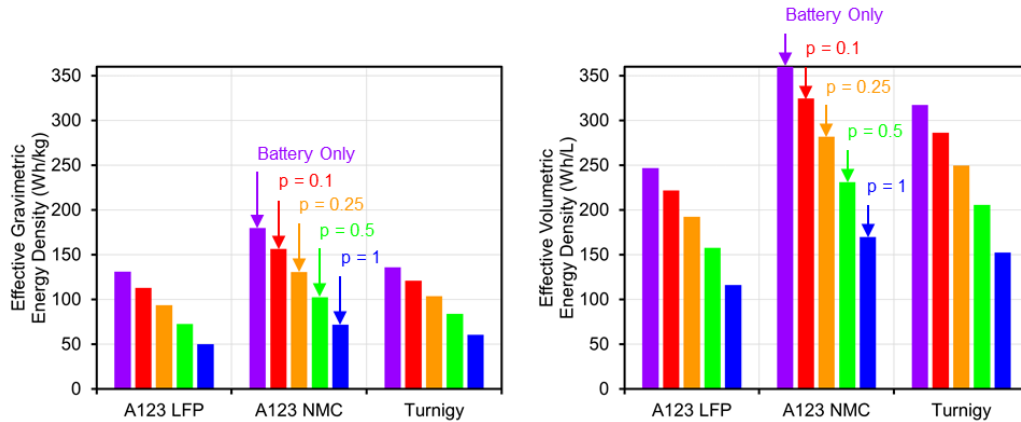
Figure 5.6. Effective energy density of the batteries with different plate thicknesses.

5.4.3. Packaging Performance

The different magnitude of losses in the three batteries and their modeled temperature rise give an indication of the thermal management requirements for the

batteries and how well they can be packed. The packaging performance is reflected in the effective energy density. The Turnigy cell, for example, is expected to have a better performance as a thinner plate can be used to remove the heat. Therefore, more energy can then be stored per volume and mass of a pack. Under ultra-fast charging conditions (4C charge), the maximum temperature rise for the Turnigy cell is 5.5°C using a plate that is 10% of the cell thickness. To achieve the same rise in the A123 LFP and NMC cells, a plate that 25% of the cell thickness and 50% of the cell thickness, respectively, is needed (Table 5.2).

As stated above, the packaging performance of the batteries is shown by their effective energy density. On paper, the A123 NMC cell has the best energy density and the A123 LFP and Turnigy cells have lower and similar energy densities. But at 4C charge, the A123 NMC cell has a lower effective gravimetric energy density than the Turnigy cell. In fact, the effective gravimetric energy density of the A132 NMC cell is much closer to the LFP cell. Originally, there was a 27% difference in the gravimetric energy density between the two cells (180 Wh/kg vs. 130 Wh/kg) but after considering the cooling system, the difference is only 7%. In a comparison of the effective volumetric energy density for the batteries, the Turnigy cell is also the best, followed by the A123 NMC cell, and then the A123 LFP cell. These results show that the aluminum plates can drastically change how a battery performs in a pack; a power-dense battery can have a better performance as the cell requires less cooling. It is therefore important to consider the thermal management requirements of a battery and the impact of the thermal management system on packaging.

Table 5.2. Comparison of battery performance at 4C charge for a 6°C temperature rise.

	A123 LFP	A123 NMC	Turnigy
Temperature Rise (°C)	6.5	6.2	5.5
Plate Thickness (p)	0.25	0.5	0.1
Effective Gravimetric Energy Density (Wh/kg)	93	103	121
Effective Volumetric Energy Density (Wh/L)	193	231	286

5.4.4. Equivalent Charge Capability

There is a trade-off between the charge rate of a battery and its effective energy density. Thicker aluminum plates can be used to achieve higher charge rates for the same temperature rise. Alternatively, thinner plates can be used to achieve a desired energy density. The trade-off most evident in the Turnigy cell where high charge rates are possible. Due to the charge limitations of the A123 LFP and NMC cell, it is less evident. The equivalent charge capability of a battery describes the charge rate that can be achieved for a given temperature rise with a given plate thickness. They are listed for the Turnigy cell in Table 5.3.

With an aluminum plate that is 10% of cell thickness, 4C charge is achieved for a temperature rise of approximately 6°C. With 100% cell thickness plate, 10C charge is achieved. But this 150% increase in charge rate is associated with a 50% decrease in the effective gravimetric energy density and a 47% decrease in the effective volumetric energy density. This means, to decrease the charge time from 15 minutes to 6 minutes, the energy that can be stored in the pack for a set mass and volume must be halved. The temperature rise can then be increased to achieve a higher energy density. In the case of the Turnigy cell, a 10C charge rate can be achieved using a 10% cell thickness plate with a 30°C temperature rise, a 25% cell

thickness plate for a 16.4°C rise, and a 50% cell thickness plate with a 9.8°C temperature rise. Alternatively, a different cooling strategy such as active intercell cooling may be used to achieve the higher rates.

Table 5.3. Equivalent charge capabilities for the Turnigy cell

Plate Thickness (p)	1	0.5	0.25	0.1
Temperature Rise (°C)	5.8	6.4	6.2	5.5
Charge Rate (C)	10	8	6	4
Effective Gravimetric Energy Density (Wh/kg)	61	84	104	121
Effective Volumetric Energy Density (Wh/L)	152	206	250	286

5.4.5. Cooling Plate Placement

The cooling plate placement was investigated to determine a configuration that would provide the best and most uniform cooling. Three configurations were modeled: (1) a cooling plate was placed at the bottom of the cells, (2) a cooling plate was placed on one side of the cells, and (3) cooling plates were placed on both sides of the cells (Figure 5.7). In the first configuration, the top of the cells is the hottest as the aluminum plates cannot transfer heat fast enough from the top to the cooling plate as it is generated (Figure 5.8a). In the second configuration, the cells are the hottest on the opposing side (Figure 5.8b). Like the first, heat must be transferred across the cell and so, it is, again, generated faster than it can be removed. Two cooling plates mean that heat can be transferred out from both sides. Hot spots are present at the center of the cells due to differences in thermal conductivity in the plane of the cell and through the cell (Figure 5.8c). All three batteries have higher conductivities in-plane than through-plane. As a result, heat remains at the center when heat is drawn out by the plates.
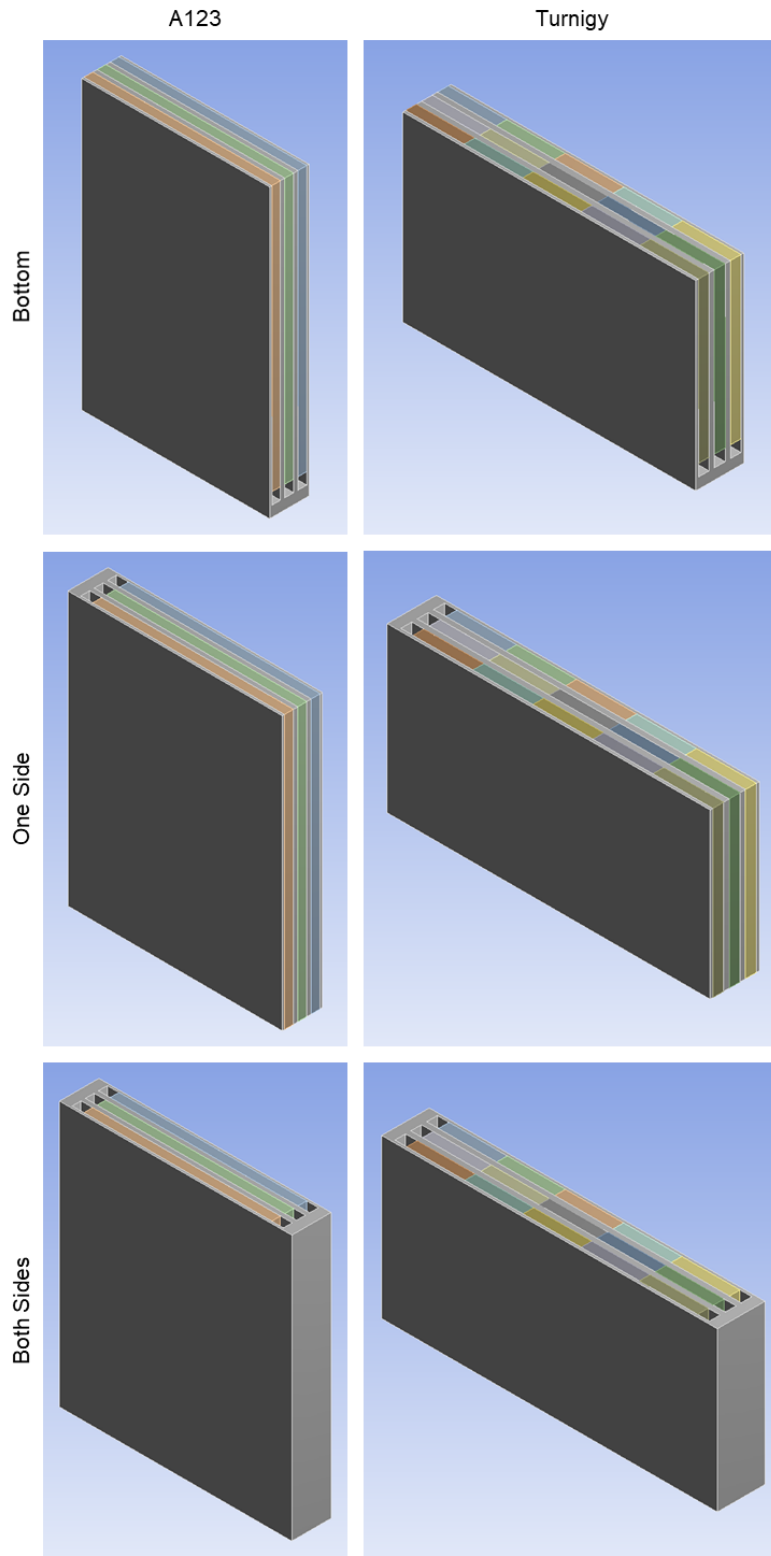
Figure 5.7. Cooling plate configurations investigated for the thermal analysis.
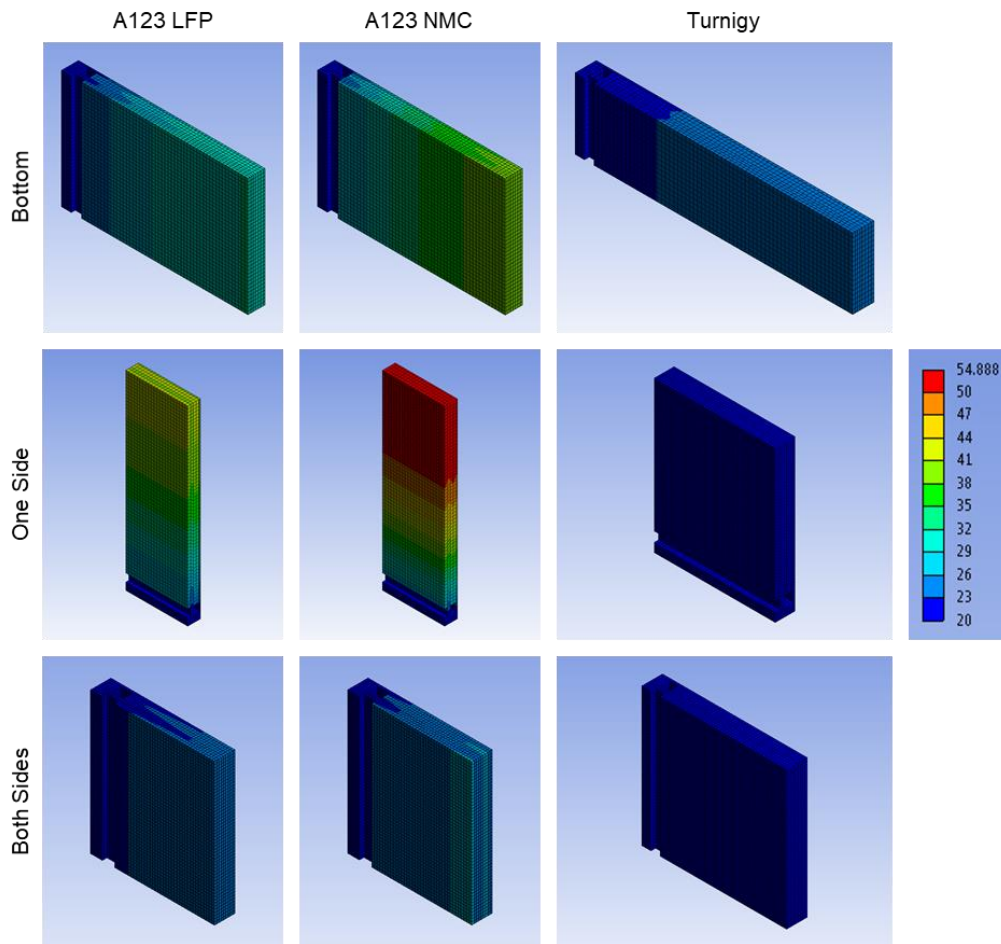
Figure 5.8. Simulated temperature distribution for the batteries at 4C charge with 25% cell thickness plates and different cooling plate placements.

Two cooling plates were used in the cooling apparatus model as they provided the best overall cooling (Figure 5.9). For the A123 LFP cell, the bottom placement had the worst performance with a maximum temperature rise of 72°C compared to the 12.5°C temperature rise for the both sides placement. Similarly, the performance of the bottom placement for the A123 NMC cell where it gave the highest temperature rises. For the Turnigy cell, the bottom placement yielded a similar temperature rise to the both sides placement. This can be attributed to the

difference in size and thermal conductivity between the Turnigy cell and the A123 cells. The Turnigy cell is 49.4% shorter in length than the A123 cells. Accordingly, the rate of heat transfer through the plate is dependent on the distance to the cooling plate. A shorter cooling plate means a higher rate of heat transfer. The Turnigy cell can also transfer 65% and 16% more heat per meter than the A123 LFP and NMC cells. Together, one plate at the bottom is sufficient for cooling the Turnigy cell.
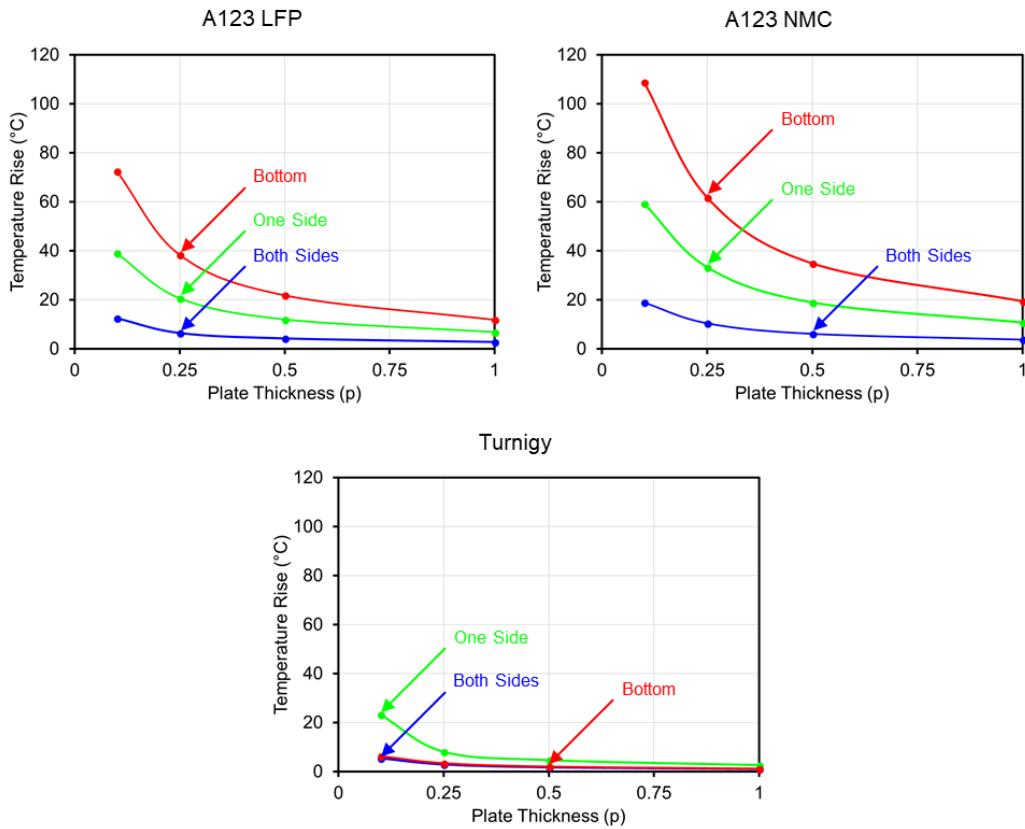
Figure 5.9. Modeled temperature rises for the batteries at 4C charge with different cooling plate configurations and plate thicknesses.

5.5. Transient Thermal Analysis

The steady-state analysis neglects the thermal mass of the components in the

cooling apparatus as there is no time domain. In reality, the thermal mass of the components will affect the temperature and cooling of the batteries over time. The thermal mass describes the ability of a material to absorb and store heat. It is given by the specific heat capacity, which is the amount of heat per unit mass needed to raise the temperature of the material by a degree. A transient thermal analysis was performed to determine the temperature rise and distribution over time and how the thermal mass of the batteries and apparatus impact the cooling behaviour.

5.5.1. Mesh Sizing

The mesh sizing was program controlled where the relevance center was used to adjust the size. There were three options for the relevance center: fine, medium, coarse. The default element size was used with the relevance centers. The number of elements for each battery with the mesh sizes is shown in Table 5.4. There is, on average, a 170% difference in the number of elements between the fine and coarse mesh for the batteries. A fine mesh was used in the steady-state thermal analysis because the scale of the execution time between the three options was similar (21 seconds vs. 6 seconds). But for the transient thermal analysis, the time using the fine mesh was significantly longer (6757 seconds vs. 1948 seconds).

Table 5.4. Number of elements in the different mesh sizes for the thermal analysis of the batteries.

p	Number of Elements in Mesh								
	A123 LFP			**A123 NMC**			**Turnigy**		
	Coarse	Medium	Fine	Coarse	Medium	Fine	Coarse	Medium	Fine
0.1	12911	7245	21840	1968	7245	21632	1740	8461	23280
0.25	1488	7214	19760	1431	7100	20322	1726	8419	20880
0.5	1504	6625	19916	1446	6530	19916	1712	7663	21120
1	893	3631	15687	1341	6380	26214	1530	7719	27730

To decrease the execution time, the peak temperature calculated from each mesh size was investigated using the steady-state thermal analysis. The average peak temperature and standard deviation of the batteries from the different mesh sizes are given in Table 5.5. The results show that the effect of the mesh sizing is negligible in the temperature calculation. The largest deviation is only 0.07°C from the mean. The difference in the mesh sizing is much smaller than the precision needed for battery pack design and thermal management. As a result, the coarse mesh can be used for the transient thermal analysis to reduce the execution time for the transient thermal analysis.

Table 5.5. Variation in the calculated peak temperature from the mesh sizing for the steady-state thermal analysis at 4C charge.

p	Average Peak Temperature (°C)		
	A123 LFP	A123 NMC	Turnigy
0.1	32.547 ± 0.072	38.904 ± 0.097	25.362 ± 0.041
0.25	26.818 ± 0.016	30.483 ± 0.023	22.931 ± 0.007
0.5	24.294 ± 0.004	26.168 ± 0.003	21.759 ± 0.003
1	22.811 ± 0.003	23.780 ± 0.002	21.044 ± 0.001

5.5.2. Temperature Rise

In the steady-state analysis, the average charge loss to 80% SOC was used as the input. For the transient thermal analysis, the loss over the entire charge time is used. Since the majority of the loss occurs during the constant current part of the charge, the results from the transient analysis with the time-dependent charge loss is compared to results using the fixed constant current charge loss (Figure 5.10). The impact of the thermal mass of the batteries and the different aluminum plates can then be investigated.
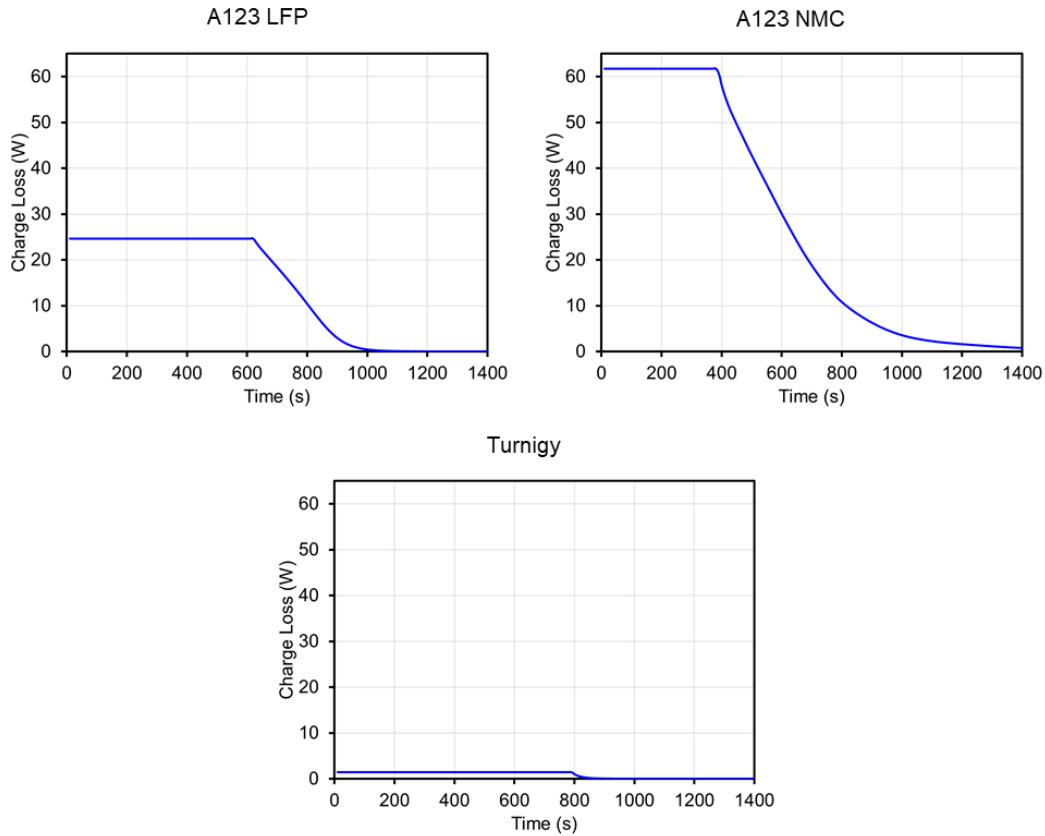
Figure 5.10. Time-dependent charge loss used in the transient thermal analysis of the batteries at 4C charge.

The modeled temperature over time for the two loss inputs with different plate thicknesses is shown in Figure 5.11. The impact of the thermal mass is given by the difference in peak temperature between the constant current loss and the transient loss simulations. It can be especially seen in the A123 NMC cell with a plate that is 10% of the cell thickness (Figure 5.11b). The peak temperature of the cell using the time-dependent charge loss, shown in blue, does not reach the temperature of the cell calculated using the fixed charge loss, shown in red. The cells are 4°C cooler when taking into account the thermal mass. This indicates that

heat is being stored in the thermal mass of the cells. Heat is unlikely to be stored in the plates due to their high thermal conductivity. Accordingly, as the plate thickness is increased, the peak temperature of the cell calculated with the time-dependent loss reaches steady state; heat is removed by the plates and not stored by the cells. It can be concluded that when heat removal by the plates is less effective, such as with thinner plates, it is more dependent on the thermal mass of the cells for cooling.
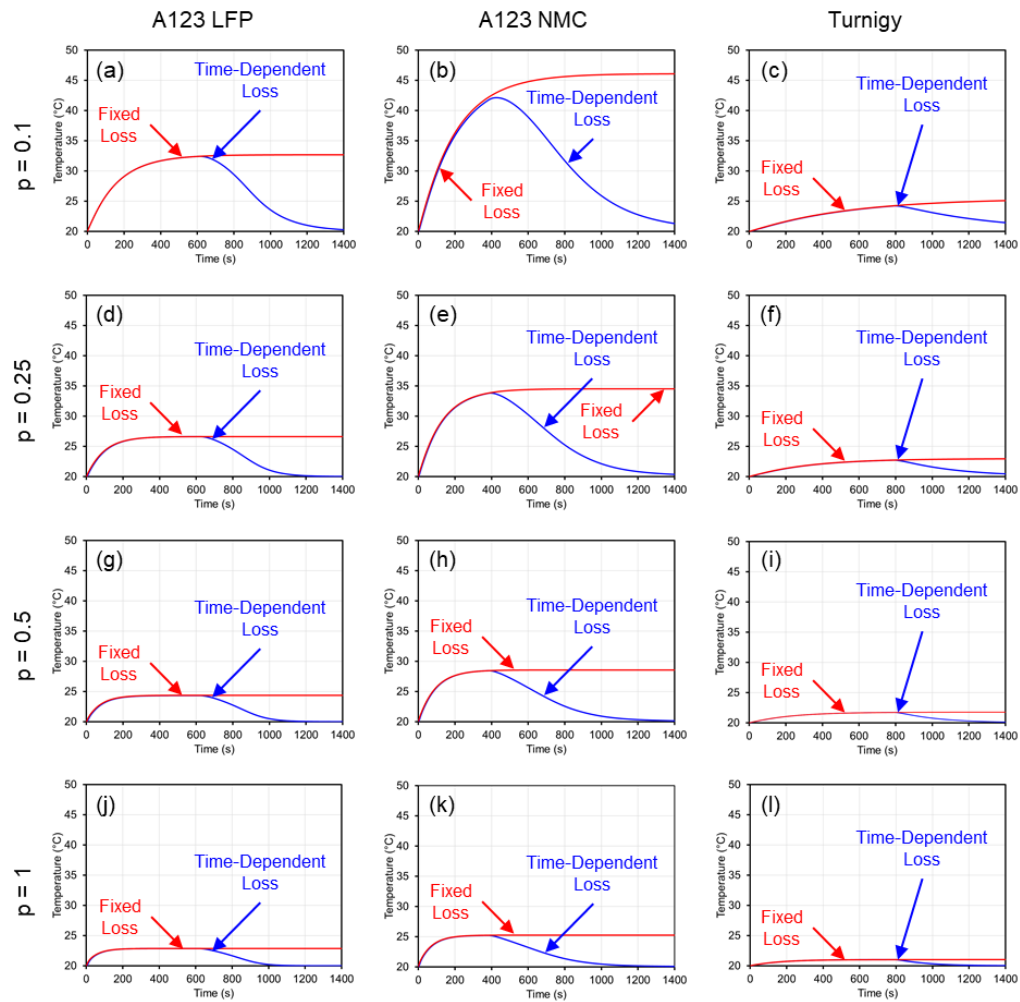
Figure 5.11. Modeled temperature obtained from the transient thermal analysis of the batteries at 4C charge with different plate thicknesses.

In comparison to the A123 NMC cell, the A123 LFP and Turnigy cells reach steady state or the fixed loss temperature in all cases. For these two batteries, cooling is effective at all plate thicknesses in that their thermal masses are not used. It is important to note that the magnitude of the heat removal is still dependent on the thickness of the plate; thicker aluminum plates can remove more heat. These results indicate that, in some cases like the Turnigy cell, the thermal management system is overdesigned for their thermal requirements. Since little heat is generated in the Turnigy cell, thinner aluminum plates, fewer cooling plates, or a simpler cooling system such as passive cooling can be used.

5.5.3. Aluminum Plate Selection

However, realistically, there are limitations to the plate thickness that can be used in a battery pack. Plates that are 10% of the cell thickness or 100% of the cell thickness are unachievable in the pack. With a thinner plate, the structural integrity of the plate is compromised. For the thinnest cell, the A123 LFP cell, a 10% cell thickness plate is about 0.75 mm, which is the thickness of an aluminum foil. And a plate that is 100% of the cell thickness would double the volume and more than double the mass. These two extremes can only be used to demonstrate the effects of changing the plate thickness. Useable plates in a battery pack are limited to the 25% to 50% cell thickness range.

With these plates, there is a trade-off between the desired temperature rise and the plate thickness. For the A123 LFP cell, the difference in the temperature rise between the 25% and 50% cell thickness plates is about 2°C. The 2°C decrease

in temperature results in a 22% decrease in the effective energy density of the cell, which is not justifiable in the design of the battery pack. When the charge loss is higher, the decrease in the effective energy density from the thicker may be acceptable. This can be demonstrated using the A123 NMC cell. The fixed loss for the NMC cell at 4C charge is 61.7 W vs. 24.7 W for the LFP cell. The 25% cell thickness plate for the A123 NMC cell has a peak temperature of 34.5°C, while the 50% cell thickness plate reaches 28.5°C. This 6°C decrease is, to some extent, more justifiable for the decrease in energy density than the 2°C decrease. As the charge loss increases with different cells, the trade-off for a thicker plate becomes more and more acceptable.

5.5.4. System Robustness

The above thermal analyses only look at cooling the batteries during one complete charge. To test the robustness of the thermal management systems, i.e., the ability to maintain the temperature of the cells, multiple partial charges are simulated in the batteries. Charging is cut off after 15 minutes, ultra-fast charging condition, and then immediately charged again for a total of three charges. The temperature was modeled with plates that are 10% of the cell thickness to give the highest temperature rise. The modeled rises are given in Figure 5.12. The cooling systems are robust. In all three cases, the cell temperature is maintained at a steady state. This is higher than the fixed loss temperature shown in Figure 5.11. It appears heat is being stored in the cell. After the initial charge, which reaches, the fixed loss temperature, more heat is added, which cannot be removed.
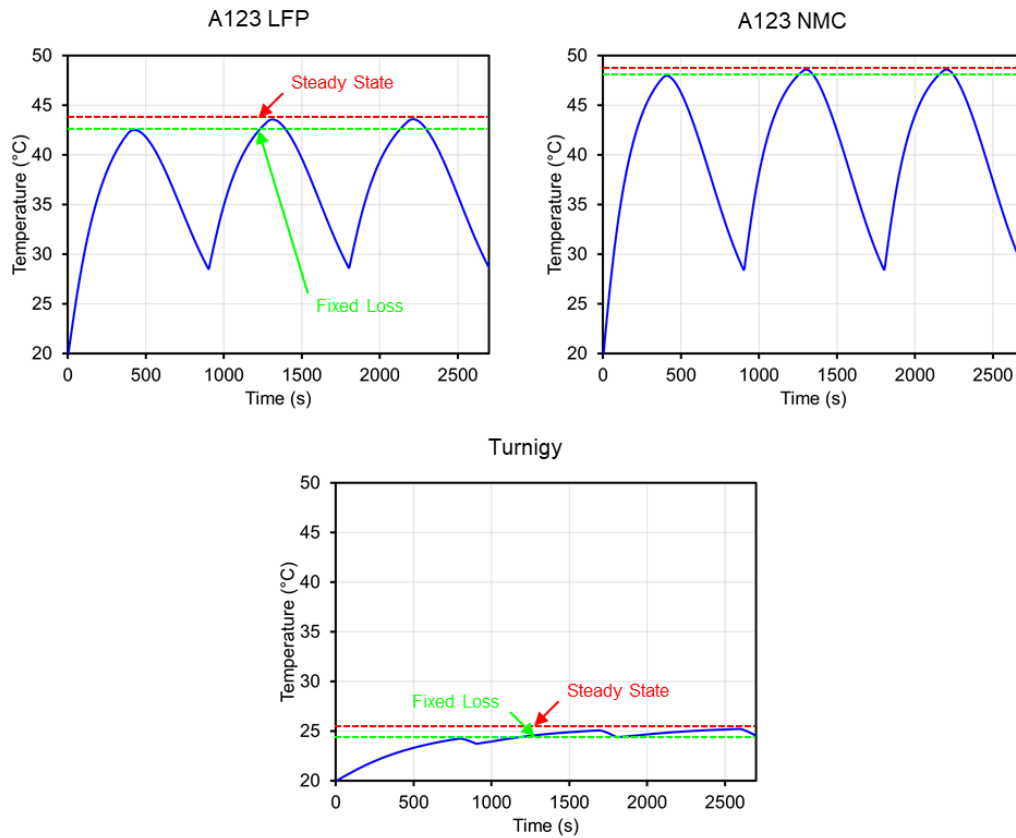
Figure 5.12. Modeled temperature for the batteries with the 10% cell thickness plate over multiple 4C charges.

5.5.5. Real-World Application

In order to round out the thermal analysis, the A123 NMC cell, which has the greatest loss out of the three batteries, was modeled in a vehicle to see how the cell would behave in a real-world situation. The 2018 Nissan Leaf was chosen due to its smaller battery pack (40 kWh vs. 60 kWh in the Chevrolet Bolt or 75 kWh in the Tesla Model 3). During road trip, the Leaf would need to be charged more often and so, charging has significant thermal implications on the vehicle. The Leaf was modeled in an Excel-based program using the road load coefficients from [100].

Relevant vehicle parameters are listed in Table 5.6.

Table 5.6. Model parameters for the 2018 Nissan Leaf.

Vehicle Mass (kg)	1598
Passenger/Cargo Mass (kg)	82
Total Mass (kg)	1680
Tire Radius (m)	0.324
Loaded Tire Radius (m)	0.314
Road Load Coefficient "A" (lbf)	25.89
Road Load Coefficient "B" (lbf/mph)	0.3449
Road Load Coefficient "C" (lbf/mph^2)	0.01945

The US06 drive cycle was then chosen for a road trip simulation due to its aggressive nature and high power. It models high speed and/or acceleration driving behaviour with rapid speed fluctuations. The cycle represents a 12.9 km route with an average speed of 77.9 km/h and a maximum speed of 129.2 km/h. Using the vehicle model with the US06 drive cycle and experimental data from the charge capability tests, a road trip was simulated for battery packs containing the A123 LFP, A123 NMC, or Turnigy cells. Here, 15.9 repetitions of the drive cycle is used to deplete the battery pack, which is followed by CCCV charge at 4C for 15 minutes. In total, there are two driving events and two charging events (Figure 5.14).

For the vehicle model, the battery pack was sized to achieve the 40-kWh of energy for the Nissan Leaf. For the A123 LFP cell, a total 606 cells are needed to achieve the pack energy value. For the A123 NMC cell, a total of 416 cells is used to achieve a 40-kWh pack. And for the Turnigy cell, a total of 2160 cells to achieve the same pack energy. The power for each pack was calculated from the drive power and the associated losses. The pack loss is calculated from the pack current and resistance. The resistance is based on the cell resistances from the 1C charge test tests (7.1 mΩ for the A123 LFP, 6.1 mΩ for the A123 NMC, and 3.4 mΩ for the Turnigy cells). The pack losses over the road trip are then shown in Figure 5.13.
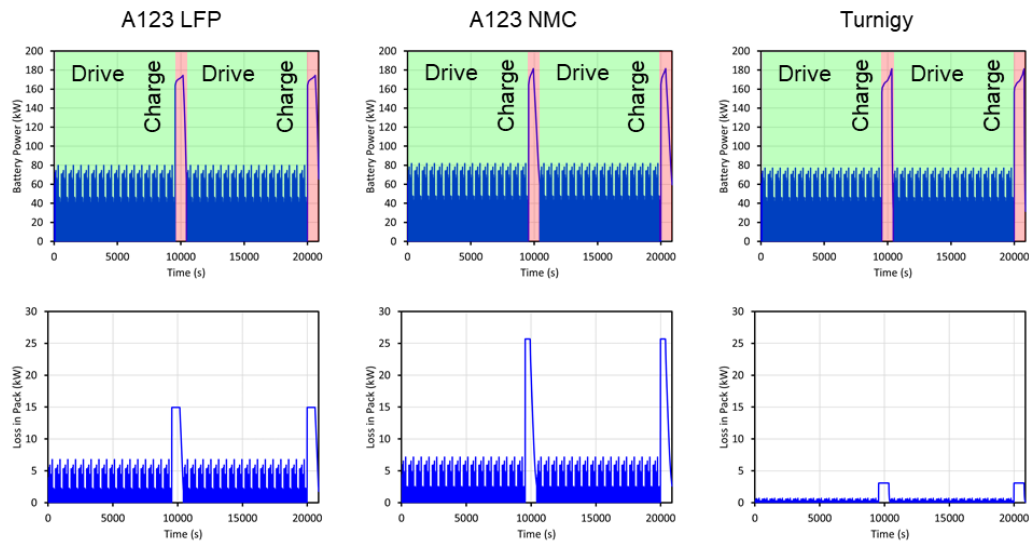
Figure 5.13. Calculated loss in the battery packs over the road trip.

The average power during driving is 23 kW and 160 kW during charging. The average losses are then 0.8 kW (drive) and 12.8 kW (charge) in the A123 LFP pack, 0.9 kW (drive) and 17.4 kW (charge) in the A12 NMC pack, and 0.09 kW

(drive) and 2.8 kW (charge) in the Turnigy pack. During driving, the loss between the A123 LFP and NMC packs are the similar as they have similar cell resistances (7.1 mΩ for the A123 LFP cell vs. 6.1 mΩ for the A123 NMC cell). The difference in the loss between the A123 packs during charge are a result of the difference in resistance at higher currents. At 4C charge, the resistance for the A123 LFP cell is 3.9 mΩ, while the resistance for the A123 NMC cell is 5.7 mΩ. There is a larger difference at 4C that is enhanced also by the higher currents, assuming the pack losses are solely from joule heating.

The loss per cell in the battery packs is calculated from the power demand for each cell. The power for each cell is calculated by dividing the pack power by the total number of cells in the pack. The power for each cell is:

$$P_{cell} = \frac{P_{pack}}{N_{cell}} \tag{5.3}$$

The current from the resulting cell power is calculated by dividing the cell power by the nominal voltage of the batteries (3.3 V for the A123 LFP, 3.6 V for the A123 NMC, and 3.7 V for the Turnigy cell).

$$I = \frac{P_{cell}}{V_{cell,nom}} \tag{5.4}$$

The cell loss is assumed to be solely from joule heating:

$$P_{cell,loss} = I^2 R_{cell} \tag{5.5}$$

The loss for a single cell calculated from the road trip simulation, which is shown in Figure 5.14, was used for the transient analysis of the three batteries in the cooling apparatus with the 10% cell thickness aluminum plate. As previously stated, charging now becomes the main source of loss. During driving, the average loss for the A123 LFP, A123 NMC, and Turnigy cells are 1.5 W, 2.3 W, and 0.01 W, respectively. During charging, the losses are then 25W, 60 W, and 1.4 W for the A123 LFP, A123 NMC, and Turnigy cells, respectively. As a result, the sizing of the cooling system for the battery pack is dictated by the charging, which generates far more than driving the vehicle.
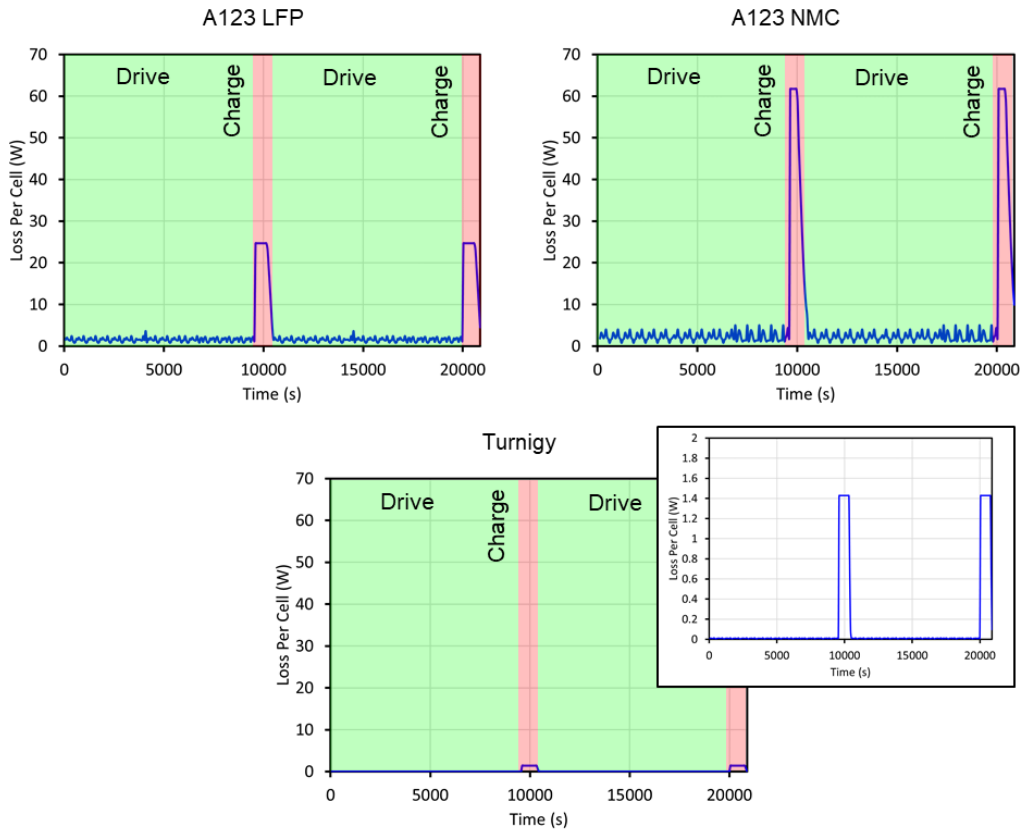
Figure 5.14. Calculated loss per cell for the batteries over the road trip.

The modeled temperature for the batteries is shown in Figure 5.15. The A123 NMC cell is the hottest over the road trip, reaching 42°C during the charging events. During the driving events, the cell achieves a steady-state temperature of 21°C. The A123 LFP and Turnigy cells are much cooler, reaching 32°C and 24°C respectively during charge. During the driving events, the three batteries reach a steady-state temperature. For the A123 LFP cell, the steady-state temperature is around 21°C. The same is observed for the A123 NMC cell. For the Turnigy cell, the loss is an order of magnitude smaller than the A123 cells, such that the temperature of the cell is maintained at the 20°C cooling plate temperature.
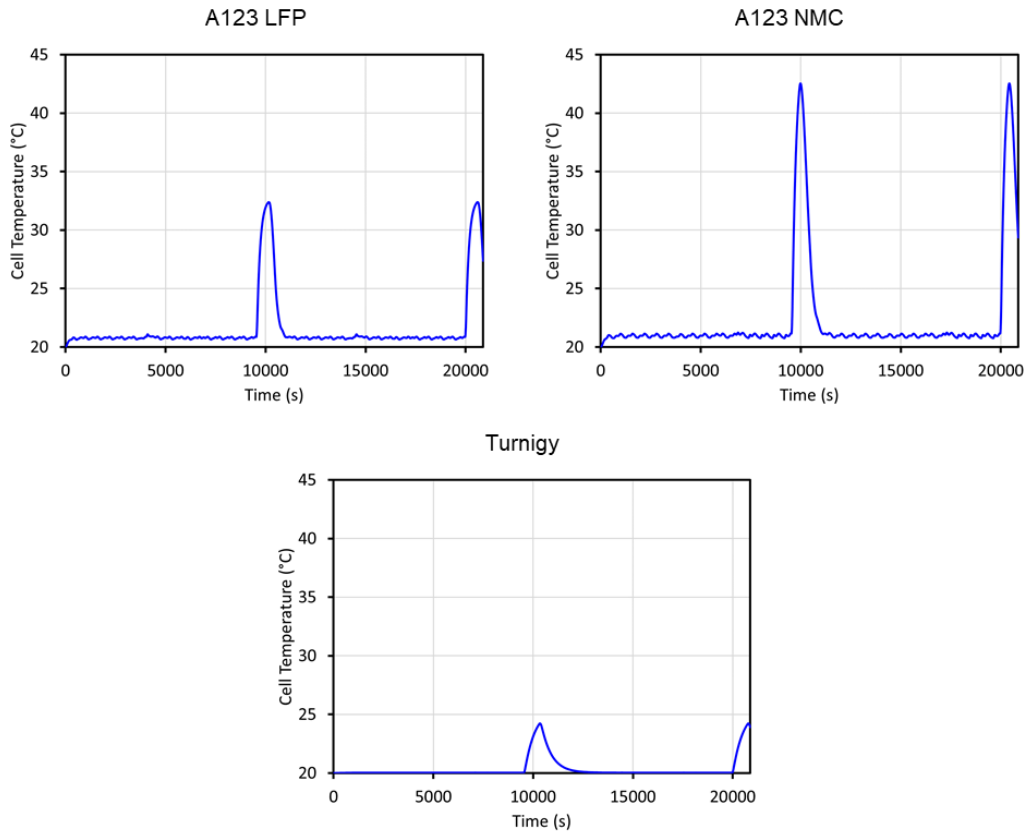
Figure 5.15. Modeled temperature of the batteries over the road trip with a 10% cell thickness plate.

5.6. Conclusions

It is important to determine what is important for the pack performance-wise and thermally, i.e., charge capability, temperature rise, energy density. From this, a more complete design of a battery pack can be made. When the thermal behaviour of the battery is considered in the cell selection and the design of a pack, a more effective thermal management system can be created and used. The cooling system can be both lighter and smaller, allowing for more room for cells.

Chapter 6
Experimental Validation to Inform Battery Pack Design

6.1. Introduction

A test fixture was built to experimentally validate the thermal analysis from Chapter 5. To do so, the fixture was designed to best replicate the model used in the analysis. The general design of the fixture was done as part of the thesis where another master's student built the fixture. Here, no experimental work is performed, but work with the fixture beyond the scope of the thesis is discussed.

6.2. Fixture Design

The fixture takes inspiration from the work by Nieto *et al.* [99]. In the paper, they present a methodology for the creation and testing of a thermal management system for high-power LIBs. Here, a battery module is built using Kokam NMC pouch cells (Figure 6.1). The module consists of 12 cells connected in series where they are positioned upright so that the tabs are found at the top. The thermal management system was designed to keep the maximum cell temperature below 35°C. The system consists of two cold plates that are placed on either side of the cell stack. It is symmetrically cooled to increase the thermal uniformity of the cells and obtain lower temperatures at the center of the cells. The same placement was selected in the thermal analysis from Chapter 5. Liquid cold plates are used where

copper tubes are embedded into aluminum. They are connected to a chiller where the inlet and coolant flow are fixed. A 50/50 ethylene glycol/water mixture is pumped through the system. The cells are sandwiched between aluminum sheets to facilitate heat dissipation from the cells to the two cold plates. Thermal interface material (TIM) is placed between the cells and sheets to increase contact between the surfaces. The cells were then compressed using the rods that run the entire length of the module and fixed at the ends. The module is enclosed in plastic.

Figure 6.1. Design of a battery module and the resulting prototype investigating the thermal management of high-power cells [99].

In the fixture, three cells are connected in parallel to achieve the same battery configuration and behaviour from the analysis. The cells are placed between aluminum sheets, which are used as the aluminum plates from the analysis. The outer sheets are half the thickness of the interior sheets like in the model to ensure uniform cooling. They are connected to cold plates located on either side of the cells using aluminum bars. The analysis assumes a perfect connection between the aluminum plates and the cooling plates. The aluminum bars enhance the contact

between the sheets and plates. Thermal pads are added between the cells and sheets to enhance heat transfer between the two. The cells are compressed using bolts threaded through the sheets. One-inch thick plastic is added to the faces of the test fixture to ensure no heat is lost from the fixture faces. Thermal properties of the materials used in the fixture are summarized in Table 6.1.
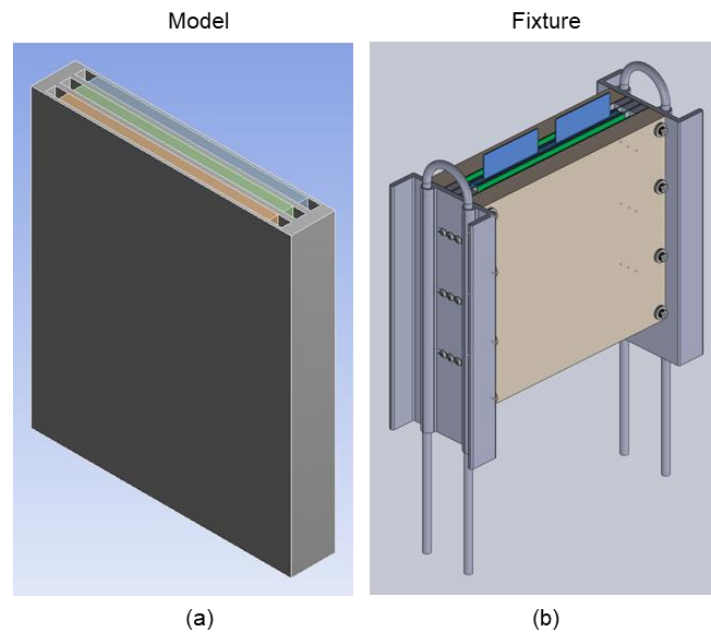
Figure 6.2. Design of the (a) cooling apparatus used in the thermal analysis and (b) test fixture used to experimentally validate the thermal analysis.

Table 6.1. Thermal properties of the materials used in the test fixture.

Component	Material	Density (kg/m³)	Specific Heat Capacity (J/kg·K)	Thermal Conductivity (W/m·K)	Thermal Expansion (μm/m·K)
Aluminum Sheet	Aluminum 3003-H14	2800	900	180	23
Aluminum Bar	Aluminum 6061-T6511	2700	900	170	24
Thermal Pad	Tflex HR440	-	-	1.8	-
Plastic	UHMW Polyethylene	940	1750	0.41	180

Based on the thermal analysis in Chapter 5, the 25% cell thickness plate was chosen for the aluminum sheets in the test fixture. The analysis showed that for the A123 cells, the decrease in the temperature rise from a plate that is 25% of the cell thickness to 50% of the cell thickness was unjustifiable with the decrease in the effective energy density. At 4C charge (ultra-fast charging), there was only a 2°C difference in temperature between the two plates for the A123 LFP cell. And for the A123 NMC cell, which generates almost double the loss of the LFP cell, the difference in temperature was only 6°C. The increase in mass and volume is not justifiable for the small decrease in the peak temperature. Aluminum sheets that are 0.08" or 2.0 mm in thickness are used. It is 26% of the cell thickness, which is the closest plate thickness to the 25% cell thickness used in the thermal analysis.

Liquid cold plates from Wakefield-Vette (180-11-12C) are used in the fixture. Specifications for the plates are given in Table 6.2. They have a rolled tube design in which copper tubes are attached to an aluminum base. Liquid cooling is used to achieve the isothermal boundary condition assumed in the thermal analysis. This boundary condition holds given a sufficiently high flow rate. They are attached to the cell structure using the same aluminum bars that attach the sheets to the plates.

Table 6.2. Specifications for the liquid cold plates.

Body Length (mm)	304.8
Body Width (mm)	127.2
Body Thickness (mm)	17.5
Channel Width (mm)	46.1
Overall Length (mm)	500.1
Overall Thermal Resistance (°C/W)	0.041 @ 1.5 GPM
Mass (kg)	1.30

The chiller that will be used is a 6-L VWR refrigerated/heated recirculating bath. The temperature range for the chiller is –20°C to 150°C ± 0.05°C. Water will be recirculated through the system to keep the cold plates at 20°C. It uses a simplex pump that has two flow rates: low at 9 L/minute or high at 15 L/minute. The higher flow rate will be used to achieve the isothermal boundary condition during testing.

The final test fixture is shown in Figure 6.3.
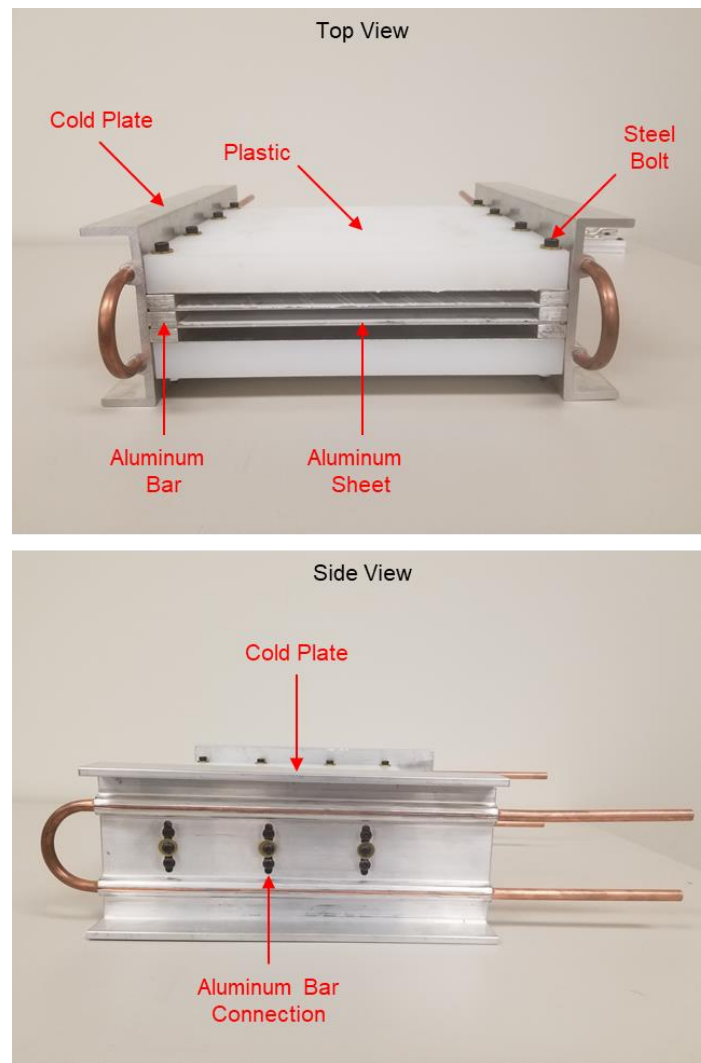
Figure 6.3. Final test fixture for the experimental validation of the thermal analysis.

The dimensions for the components shown in Figure 6.3 are given in Table 6.3.

Table 6.3. Dimensions for test fixture components.

Internal Aluminum Sheet	279 mm × 254 mm × 2 mm (11" × 10" × 0.08")
Outer Aluminum Sheet	279 mm × 254 mm × 1 mm (11" × 10" × 0.04")
Aluminum Bar	279 mm × 19 mm × 9.5 mm (11" × 0.75" × 0.375")
Plastic	279 mm × 254 mm × 25 mm (11" × 10" × 1")

6.3. Temperature Sensor Placement

The test fixture has been built but cells have not been tested in the fixture. The planned placement for temperature sensors in the fixture is shown in Figure 6.4. In total, six Type K thermocouples (TCs) will be used in the test fixture. The inlet and outlet temperature of the liquid used in the cold plates will also be measured. The TCs will be placed on the center cell and an interior aluminum sheet. More specifically, four of the TCs will be placed on the surface of the cell, as shown in Figure 6.4a. Literature has shown that a majority of the heat is initially generated near the tabs [101], [102]. As a result, temperature sensors will be placed near both the positive and negative tabs. The thermal analysis showed that the center of the cells is the hottest in the cooling apparatus. And so, the third TC will be placed at the center of the cell. To determine the temperature distribution on the surface of the cell, a fourth TC will be placed on the bottom center of the cell.

In the thermal analysis, contact resistances were ignored between all surfaces. To determine the contact resistance between the cell, thermal pad, and sheets, the remaining TCs will be placed on the aluminum sheet closest to the cell surface that is being measured (Figure 6.4b). One TC will be placed at the center of the sheet

on the side facing the cell, between the sheet and the thermal pad. The other TC will be placed on the other side of the sheet in the same location. Since the loss from the cell is known, the contact resistance is then,

$$R_{contact} = \frac{\Delta T \times A_{contact}}{Q} \tag{6.1}$$

Where Q is the known loss, $A_{contact}$ is the area of contact between the materials, and ΔT is the temperature difference between any two TCs. Using the three TCs found at the center of the fixture, the contact resistances can be calculated from the temperature difference from the cell to the plate and then across the plate to give the resistances across all surfaces.
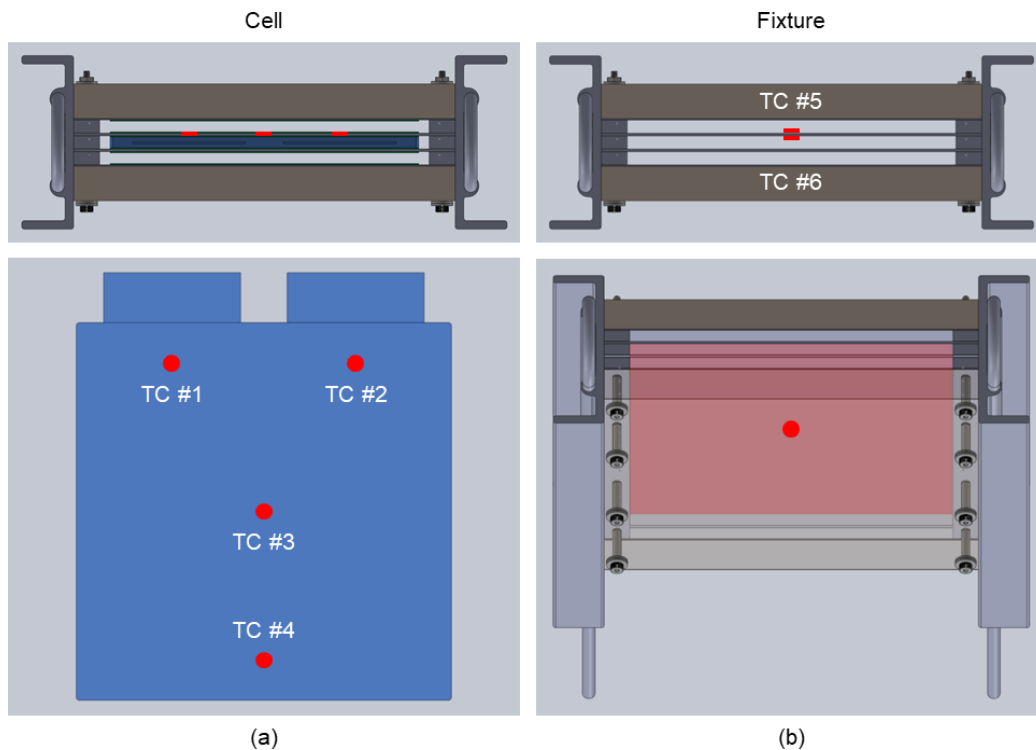
Figure 6.4. Planned temperature sensor placement for the (a) cell and (b) test fixture.

6.4. Cell Selection

Two out of the three batteries tested encountered limits at higher charge rates (>4C). The cause of these limits can only be speculated as the rate capability of a battery is dependent on a multitude of factors that are unspecified in commercial cells, e.g., cathode composition, electrolyte composition, electrode thickness. And so, a Kokam NMC cell was selected as the battery to be tested in the fixture. Unlike other manufacturers, Kokam provides more detail into the cathode chemistry of their cells. Their NMC cells are divided into high energy (HE), high power (HP), and ultra-high power (UHP). These categories can be used to infer the composition of the cathode. The Kokam NMC cell is a HP cell, which makes it most likely NMC 111. Their UHP NMC cells are then mostly likely NMC 622 or NMC 811. The Kokam cell is compared against the A123 NMC cell in Table 6.4.

Table 6.4. Comparison of specifications for the NMC cells.

	A123 NMC	Kokam NMC
Dimensions (mm)	$w = 161$	$w = 226$
	$h = 227$	$h = 227$
	$t = 7.5$	$t = 7.8$
Mass (kg)	0.55	0.72
Density (kg/m^3)	2007	1799
Rated Capacity (Ah)	26	31
Nominal Resistance (mΩ)	2.7	1.4[a]
Maximum Continuous Discharge Rate (C)	6	8
Gravimetric Energy Density (Wh/kg)	180	158

[a]Based on the AC resistance = 0.9 mΩ

The Kokam cell is larger and heavier than the A123 cell. But as a result, it is less dense than the A123 cell with a difference of 11% in density. The energy density of the Kokam cell is also 20% less than the A123 cell. However, the cell

resistance indicates the potential of the Kokam cell for a higher rate capability. The Kokam cell has almost half the resistance of the A123 cell. And so, at the same charge rate (e.g. 4C charge), it will have half the loss, assuming that heat is mainly generated from joule heating.

6.5. Preliminary Analysis

The rated cell resistance was used to estimate the charge loss in the Kokam cell. In Figure 6.5, the normalized charge loss for the Kokam NMC cell is compared to the A123 NMC cell. Over the experimental charge range for the A123 cell (1C to 4C), the Kokam cell is expected to have one-third less loss per ampere-hour than the A123 cell. The Kokam cell was then modeled in the cooling apparatus described in Chapter 4, where the temperature rise with the different plates thicknesses was calculated. A comparison of the rises for the NMC cells is given in Figure 6.6.
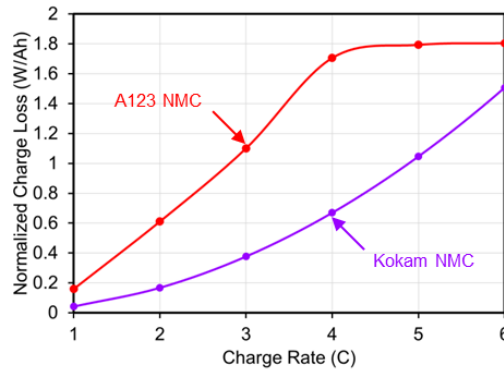
Figure 6.5. Comparison of charge losses for the NMC batteries. The charge loss for the Kokam NMC cell is estimated from the rated cell resistance.

As expected, the temperature rise for the Kokam cell is overall lower than for the A123 cell. At 4C charge, a 6°C temperature rise is achieved with the Kokam

cell using a plate that is 25% of the cell thickness. The effective energy density of the Kokam cell is then 109 Wh/kg. For the same charge rate and temperature rise, the A123 cell requires a plate that is 50% of the cell thickness. The effective energy density for the A123 cell is 103 Wh/kg. While the values for the energy density of the systems are similar, there is only a 6% difference between the two, the A123 cell sees a larger decrease in energy density when compared to its rated value. With the plate, the energy density of the Kokam cell decreases by 29%, while the A123 cell decreases by 43%, which is a difference of 40%.
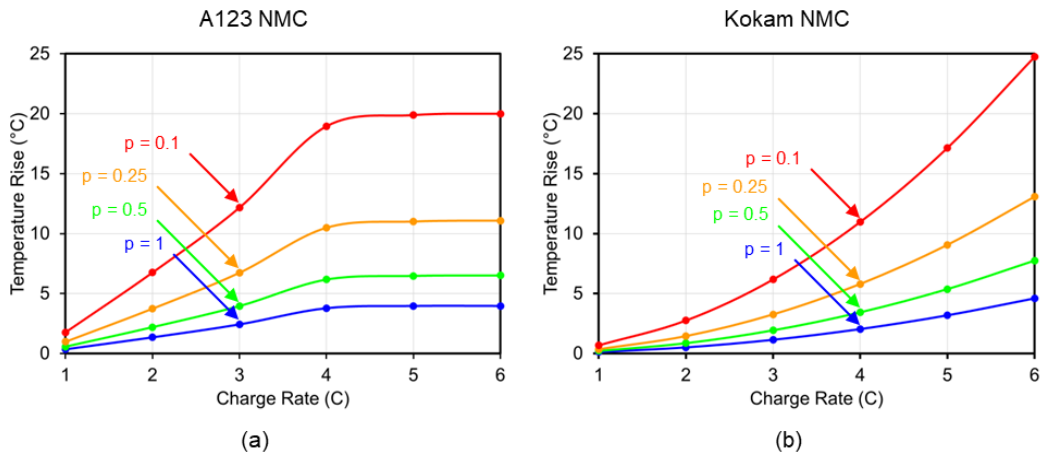
Figure 6.6. Comparison of the modeled temperature rise obtained from the steady-state thermal analysis of the (a) A123 NMC and (b) Kokam NMC cells with different plate thicknesses.

6.6. Test Plan

The purpose of the test fixture is to refine the model used in the thermal analysis and experimentally validate the results from the analysis. Since the cells have yet to be tested in the fixture, the plan for the tests will be discussed. The tests can be separated into three specific stages: (1) characterization, (2) validation, and (3) testing. Details for the tests are summarized in Table 6.5.

In the first stage, the three Kokam cells will be characterized together. This is to ensure that there is no uneven aging of the cells and that the cells remain in the same relative condition. As well, the cooling system will be turned off during the characterization stage to observe the thermal behaviour of the cells and calculate contact resistances. First, the cells will be characterized using the HPPC test described in Chapter 3. Due to the increase in capacity with paralleling the cells, only the 1C charge and discharge pulse will be used. Once the cells have been characterized and the resistance and power capabilities of the battery have been calculated, the charge capability for the cells will be investigated. The Kokam cells will be probed from 1C to 6C, like the A123 cells. The calculated loss will be used in the thermal analysis at 4C charge.

To validate the temperature rise calculations in the thermal analysis, the cells will again be charged at the 4C charge rate but with active cooling. The cold plates will be maintained at 20°C to determine the actual temperature rise with the cooling system. To validate the road trip simulation performed in the thermal analysis in Chapter 5, the US06 drive cycle will be tested on the cell until the cell is fully depleted to determine the thermal behaviour of the cells during driving. These two tests will then be combined to simulate a road trip to examine how the battery would behave thermally in real-world conditions, as simulated in Section 5.5.5 for the three other batteries. Charging at different plate temperatures (15°C and 25°C) and rates (1C and 4C) will also be investigated to evaluate the thermal model after it has been refined and validated.

Table 6.5. Details for the experimental validation of the thermal analysis using the test fixture.

Test #	Test	Details
1	HPPC (Characterization)	No cooling 1C pulse only 10% SOC increments Upper voltage limit: 4.2 V Lower voltage limit: 2.7 V Lower current cut off: 0.1 A
2	Charge Capability (Characterization)	No cooling CCCV charge Charge rate: 1C–6C
3	Temperature Rise (Validation)	Cold plate temperature: 20°C CCCV charge Charge rate: 4C
4	Drive Cycle (Testing)	Cold plate temperature: 20°C US06 drive cycle
5	Road Trip (Testing)	Cold plate temperature: 20°C US06 drive cycle, CCCV charge @ 4C
6	Temperature Rise (Testing)	Cold plate temperature: 15°C, 25°C CCCV charge Charge rate: 1C, 4C

6.7. Conclusions

In summary, a test fixture was designed and built to experimentally validate the results from the thermal analysis and refine the models used in the analysis for the battery pack design. A new LIB, the Kokam NMC cell, was chosen for testing as the A123 cells encounter charge limits at higher rates. This cell shows promise for ultra-fast charging due to its low cell resistance. The preliminary steady-state thermal analysis of the Kokam cell using FEA shows superior cooling results when compared to the A123 NMC cell. Since the battery has yet to be tested, plans for testing were discussed.

Chapter 7
Conclusions

7.1. Summary and Conclusions

In the thesis, three batteries covering a matrix of energy and power densities were investigated for ultra-fast charging. They include the A123 LFP, A123 NMC, and Turnigy cells. The thesis can be divided into two parts: (1) experimental and (2) simulation work. In the first part, the HPPC test was used to determine the cell resistance and power capabilities of the batteries. Overall, the A123 NMC cell had the best cell characteristics. The NMC cell was shown to have the lowest resistance and the highest power capability during both charge and discharge. The charge capability of the batteries was then investigated. All three cells achieved ultra-fast charging rates. The A123 cells were charged from 1C to 6C rate, while the Turnigy cell was charged up to 10C. Their performance during charging was evaluated by their efficiency, loss, and peak temperature. The power-dense Turnigy cell proved to have the best charge performance. At 4C charge, its charge efficiency was above 98% with less than 0.4 W/Ah of loss and the lowest peak temperature at 25°C. This was followed by the energy-dense A123 NMC cell and then the A123 LFP cell. The efficiencies of these cells were much lower, ending below 90%. The A123 NMC cell has almost six times the loss of the Turnigy cell and the LFP cell has about four times the loss at 4C charge. As a result, the peak temperatures are higher at 30°C and 28°C, respectively.

In the second part, the loss calculated from the cell testing was used in the thermal analysis of the cells using FEA. Both steady-state and transient analyses were performed. A cooling apparatus was modeled with the batteries using solid aluminum plates. In the steady-state analysis, the thermal behaviour of the cells with different plate thicknesses was investigated where the temperature rises were calculated. The Turnigy cell was shown to have the best thermal performance with the lowest temperatures throughout the analysis, while the A123 NMC cell had the highest temperatures. The impact of the cooling system on the battery for use in a battery pack was also determined. Here, the plates affect the energy density of the battery in the pack. With a larger system, i.e., thicker plates, less cells can be packed for a given pack volume and mass. The cooling system had the largest impact on the hotter A123 NMC cell. As a result, similar energy densities were achieved by the A123 LFP and Turnigy cells. It shows that battery selection is key in the design of a pack for ultra-fast charging. A less energy dense but more power dense cell can provide similar overall energy density to a more energy dense but less power dense cell after taking into account its thermal management. The trade-off between the desired temperature rise and a realistic plate thickness was also discussed. In the transient analysis, the impact of the thermal mass of the cells was investigated. Here, it was shown that the less effective the cooling system, i.e., the thinner the plates, the more dependent it is on the thermal mass of the batteries. This is more apparent when the charge loss is high. With the transient thermal analysis, it also showed that cooling system was effective and robust.

The main contribution of this research is its holistic approach to the ultra-fast charging of LIBs. In contrast to literature, multiple different LIBs were tested and compared at charge rates higher than 3C where both the electrical and thermal performance of the batteries were considered. This thesis identifies the trade-offs between the electrical and thermal performance of the batteries and stresses the need to understand the thermal behaviour of the cells. The thesis attempts to bridge the gap between the electrical engineer and electrochemist in answering questions about how the cell performs and why the cell performs in this way. The observed performance of the batteries was tied back to the underlying chemistry that governs the batteries.

7.2. Future Work

The next steps in the research are clear: validate the thermal analysis of the batteries and expand upon the selection of batteries from the thesis. The analysis also holds little meaning toward the design of battery pack if it is not confirmed experimentally. Results from the simulations can only be used to compare the relative performance of the batteries. But to reliably select a cell for the pack, the analysis must be validated. Additionally, both A123 cells used in the thesis were unable to achieve charging times beyond the 4C rate. In order to determine whether this was a limitation of the cathode chemistries or the cell assembly, e.g., electrode thickness, tab attachment, electrolyte composition, LIBs from other manufacturers must be tested. And for the design of a battery pack capable of ultra-fast charging, the more batteries that are studied, the better the cell selection. A more informed

choice can be made for the pack, which allows for a lighter, cooler, and longer lasting battery pack. To start the next stage of research, Kokam NMC cells have been purchased and received, while the test fixture for the cells has been built. Plans for both of these steps are discussed in Chapter 6.

The future work for the thesis is to investigate battery aging with ultra-fast charging. While there was very little change in the capacity of the cells during testing, aging of the cells with charging must be addressed. Research has shown that LIBs will age with repeated cycling and under extreme operating conditions, i.e., high and low temperatures, overvoltage, high rates [21], [103]. In all of these cases, the stability of the battery components is affected. Electrode deformation, lithium plating, dendrite formation will affect the lifetime of a cell. Since high rates are used during ultra-fast charging, batteries are expected to age faster. And with aging, the resistance of the cell will increase, which will increase the amount of loss during charging. This will, in turn, affect the thermal management requirements of the battery. Therefore, the initial thermal management requirements for the battery do not necessarily meet the requirements for the battery after aging. It is important to understand how the battery ages with ultra-fast charging to ensure that the cell is appropriate for the application, i.e., the battery has a high cycle life, and that the thermal management system can meet the needs of the cell.

References

[1]   S. M. Lukic, J. Cao, R. C. Bansal, F. Rodriguez, and A. Emadi, "Energy Storage Systems for Automotive Applications," *IEEE Trans. Ind. Electron.*, vol. 55, pp. 2258–2267, 2008.

[2]   M. Yilmaz and P. T. Krein, "Review of Charging Power Levels and Infrastructure for Plug-In Electric and Hybrid Vehicles," *IEEE Trans. Power Electron.*, vol. 28, pp. 2151–2169, 2012.

[3]   International Energy Agency, "Global EV Outlook 2017," *IEA Publ.*, pp. 1–71, 2017.

[4]   F. Lambert, "Ionity Ultra-Fast Electric Car Charging Network Partners with Shell To Deploy Chargers at Petrol Stations," *Electrek*, 2017. .

[5]   F. Lambert, "Another 'Ultra-Fast' Electric Vehicle Charging Network is Coming to Europe," *Electrek*, 2018. .

[6]   F. Lambert, "Porsche is Bringing its Ultra-Fast Electric Car Charging Stations to the US," *Electrek*, 2017. .

[7]   ABB, "TOSA Electrical Bus Charging Infrastructure," 2018. [Online]. Available: https://new.abb.com/substations/railway-and-urban-transport-electrification/tosa-electrical-bus-charging-infrastructure.

[8]   Microvast, "Applications - Public Transit," 2018. [Online]. Available: http://www.microvast.com/index.php/application_areas/28.

[9]   Siemens AG, "Charging Systems for Ebuses," 2018. [Online]. Available: https://www.siemens.com/global/en/home/products/mobility/road-

solutions/electromobility/ebus-charging.html.

[10]   Endesa, "Next Stop: Ultrafast Charging in Barcelona," 2017. [Online].
         Available: https://www.endesa.com/en/projects/a201611-ultrafast-
         charging-bus-barcelona.html.

[11]   G. Jungmeier, "IEA HEV Task 33 'Battery Electric Busses,'" in
         International Conference on Electric Mobility and Public Transport, 2017.

[12]   A. Atak and L. Grande, "Li-Ion Batteries for Electric Buses 2018-2028,"
         2018.

[13]   T. Tong and C. Groesbeck, "10 Minute LTO Ultrafast Charge Public
         Transit EV Bus Fleet Operational Data - Analysis of 240,000 KM, 6 Bus
         Fleet Shows Viable Solution," *World Electr. Veh. J.*, vol. 5, no. 1, pp. 261–
         268, 2012.

[14]   S.-L. Wu *et al.*, "High Rate Capability of Li(Ni1⁄3Mn1⁄3Co1⁄3)O2
         Electrode for Li-Ion Batteries," *J. Electrochem. Soc.*, vol. 159, no. 4, p.
         A438, 2012.

[15]   P. D. Prezas *et al.*, "Effect of Fast Charging of Lithium-Ion Cells:
         Performance and Post-Test Results," 2016.

[16]   X. Yang and T. Miller, "Fast-Charging Lithium-Ion Batteries," in *SAE
         World Congress Experience*, 2017, pp. 1–7.

[17]   T. Grandjean, A. Barai, E. Hosseinzadeh, Y. Guo, A. McGordon, and J.
         Marco, "Large Format Lithium Ion Pouch Cell Full Thermal
         Characterisation for Improved Electric Vehicle Thermal Management," *J.*

Power Sources, vol. 359, pp. 215–225, 2017.

[18] U. S. Kim, J. Yi, C. B. Shin, T. Han, and S. Park, "Modelling the Thermal Behaviour of a Lithium-Ion Battery During Charge," *J. Power Sources*, vol. 196, no. 11, pp. 5115–5121, 2011.

[19] M. Keyser *et al.*, "Enabling Fast Charging – Battery Thermal Considerations," *J. Power Sources*, vol. 367, pp. 228–236, 2017.

[20] A. Burke and M. Miller, "Life Cycle Testing of Lithium Batteries for Fast Charging and Second-Use Applications," in *International Battery, Hybrid and Fuel Cell Electric Vehicle Sym*, 2014, pp. 1–10.

[21] Y. Gao, J. Jiang, C. Zhang, W. Zhang, and Z. Ma, "Lithium-Ion Battery Aging Mechanisms and Life Model Under Different Charging Stresses," *J. Power Sources*, vol. 356, pp. 103–114, 2017.

[22] C. D. Rahn and C.-Y. Wang, *Battery Systems Engineering*. 2013.

[23] M. Eshani, Y. Gao, S. Gay, and A. Emadi, *Modern Electric, Hybrid Electric and Fuel Cell Vehicles: Fundamentals, Theory, and Design*. 2010.

[24] A. Emadi, *Advanced Electric Drive Vehicles*. 2015.

[25] N. Nitta, F. Wu, J. T. Lee, and G. Yushin, "Li-Ion Battery Materials: Present and Future," *Mater. Today*, vol. 18, no. 5, pp. 252–264, 2015.

[26] P. C. Tsai *et al.*, "Single-Particle Measurements of Electrochemical Kinetics in NMC and NCA Cathodes for Li-Ion Batteries," *Energy Environ. Sci.*, vol. 11, no. 4, pp. 860–871, 2018.

[27] Johnson Matthey Battery Systems, "Guide to Batteries," 2017.

[28] J. Dahn and G. M. Ehrlich, "Lithium-Ion Batteries," in *Linden's Handbook of Batteries*, Fourth Edi., T. B. Reddy, Ed. 2011.

[29] R. Amin, D. B. Ravnsbaek, and Y.-M. Chiang, "Characterization of Electronic and Ionic Transport in Li1-xNi0.8Co0.15Al0.05O2 (NCA)," *J. Electrochem. Soc.*, vol. 162, no. 7, pp. A1163–A1169, 2015.

[30] M. Park, X. Zhang, M. Chung, G. B. Less, and A. M. Sastry, "A Review of Conduction Phenomena in Li-Ion Batteries," *J. Power Sources*, vol. 195, no. 24, pp. 7904–7929, 2010.

[31] B. Zhao, R. Ran, M. Liu, and Z. Shao, "A Comprehensive Review of Li4Ti5O12-Based Electrodes for Lithium-Ion Batteries: The Latest Advancements and Future Perspectives," *Mater. Sci. Eng. R*, vol. 98, pp. 1–71, 2015.

[32] M. Armand and J. M. Tarascon, "Building Better Batteries," *Nature*, vol. 451, no. 7179, pp. 652–657, 2008.

[33] B. Scrosati and J. Garche, "Lithium Batteries: Status, Prospects and Future," *J. Power Sources*, vol. 195, no. 9, pp. 2419–2430, 2010.

[34] J. W. Choi and D. Aurbach, "Promise and Reality of Post-Lithium-Ion Batteries with High Energy Densities," *Nat. Rev. Mater.*, vol. 1, 2016.

[35] A. Manthiram, "An Outlook on Lithium Ion Battery Technology," *ACS Cent. Sci.*, vol. 3, no. 10, pp. 1063–1069, 2017.

[36] Y. Tang, Y. Zhang, W. Li, B. Ma, and X. Chen, "Rational Material Design for Ultrafast Rechargeable Lithium-Ion Batteries," *Chem. Soc. Rev.*, vol.

44, no. 17, pp. 5926–5940, 2015.

[37]   X. Zuo, J. Zhu, P. Müller-Buschbaum, and Y. J. Cheng, "Silicon Based Lithium-Ion Battery Anodes: A Chronicle Perspective Review," *Nano Energy*, vol. 31, no. October 2016, pp. 113–143, 2017.

[38]   A. Franco Gonzalez, N. H. Yang, and R. S. Liu, "Silicon Anode Design for Lithium-Ion Batteries: Progress and Perspectives," *J. Phys. Chem. C*, vol. 121, no. 50, pp. 27775–27787, 2017.

[39]   X. Song, X. Wang, Z. Sun, P. Zhang, and L. Gao, "Recent Developments in Silicon Anode Materials for High Performance Lithium-Ion Batteries," *Sigma-Aldrich*, 2013. [Online]. Available: https://www.sigmaaldrich.com/technical-documents/articles/materials-science/recent-developments-in-silicon-anode-materials.html.

[40]   V. G. Khomenko, V. Z. Barsukov, J. E. Doninger, and I. V. Barsukov, "Lithium-Ion Batteries Based on Carbon-Silicon-Graphite Composite Anodes," *J. Power Sources*, vol. 165, no. 2, pp. 598–608, 2007.

[41]   F. Schipper, E. M. Erickson, C. Erk, J.-Y. Shin, F. F. Chesneau, and D. Aurbach, "Review—Recent Advances and Remaining Challenges for Lithium Ion Battery Cathodes," *J. Electrochem. Soc.*, vol. 164, no. 1, pp. A6220–A6228, 2017.

[42]   S. T. Myung *et al.*, "Nickel-Rich Layered Cathode Materials for Automotive Lithium-Ion Batteries: Achievements and Perspectives," *ACS Energy Lett.*, vol. 2, no. 1, pp. 196–223, 2017.

[43]   A. Manthiram, B. Song, and W. Li, "A Perspective on Nickel-Rich Layered Oxide Cathodes for Lithium-Ion Batteries," *Energy Storage Mater.*, vol. 6, pp. 125–139, 2017.

[44]   EC Power, "Virtual Cell Design and System Sizing with Ni-Rich High Capacity Cathode Active Materials," 2014.

[45]   W. Xu *et al.*, "Lithium Metal Anodes for Rechargeable Batteries," *Energy Environ. Sci.*, vol. 7, no. 2, pp. 513–537, 2014.

[46]   G. Girishkumar, B. McCloskey, A. C. Luntz, S. Swanson, and W. Wilcke, "Lithium-Air Battery: Promise and Challenges," *J. Phys. Chem. Lett.*, vol. 1, no. 14, pp. 2193–2203, 2010.

[47]   P. Tan *et al.*, "Advances and Challenges in Lithium-Air Batteries," *Appl. Energy*, vol. 204, pp. 780–806, 2017.

[48]   D. Lin, Y. Liu, and Y. Cui, "Reviving the Lithium Metal Anode for High-Energy Batteries," *Nat. Nanotechnol.*, vol. 12, no. 3, pp. 194–206, 2017.

[49]   X. B. Cheng, R. Zhang, C. Z. Zhao, and Q. Zhang, "Toward Safe Lithium Metal Anode in Rechargeable Batteries: A Review," *Chem. Rev.*, vol. 117, no. 15, pp. 10403–10473, 2017.

[50]   W. Qi, J. G. Shapter, Q. Wu, T. Yin, G. Gao, and D. Cui, "Nanostructured Anode Materials for Lithium-Ion Batteries: Principle, Recent Progress and Future Perspectives," *J. Mater. Chem. A*, vol. 5, no. 37, pp. 19521–19540, 2017.

[51]   R. Mukherjee, A. V. Thomas, A. Krishnamurthy, and N. Koratkar,

"Photothermally Reduced Graphene as High-Power Anodes for Lithium-Ion Batteries," *ACS Nano*, vol. 6, no. 9, pp. 7867–7878, 2012.

[52]   Y. Wang and G. Cao, "Developments in Nanostructured Cathode Materials for High-Performance Lithium-Ion Batteries," *Adv. Mater.*, vol. 20, no. 12, pp. 2251–2269, 2008.

[53]   H.-K. Song, K. T. Lee, M. G. Kim, L. F. Nazar, and J. Cho, "Recent Progress in Nanostructured Cathode Materials for Lithium Secondary Batteries," *Adv. Funct. Mater.*, vol. 20, no. 22, pp. 3818–3834, 2010.

[54]   R. Pitchai, V. Thavasi, S. G. Mhaisalkar, and S. Ramakrishna, "Nanostructured Cathode Materials: A Key for Better Performance in Li-Ion Batteries," *J. Mater. Chem.*, vol. 21, no. 30, pp. 11040–11051, 2011.

[55]   S. T. Myung, K. Amine, and Y. K. Sun, "Nanostructured Cathode Materials for Rechargeable Lithium Batteries," *J. Power Sources*, vol. 283, pp. 219–236, 2015.

[56]   Z. S. Wu, W. Ren, L. Xu, F. Li, and H. M. Cheng, "Doped Graphene Sheets as Anode Materials with Superhigh Rate and Large Capacity for Lithium Ion Batteries," *ACS Nano*, vol. 5, no. 7, pp. 5463–5471, 2011.

[57]   U. H. Kim, E. J. Lee, C. S. Yoon, S. T. Myung, and Y. K. Sun, "Compositionally Graded Cathode Material with Long-Term Cycling Stability for Electric Vehicles Application," *Adv. Energy Mater.*, vol. 6, no. 22, pp. 1–8, 2016.

[58]   G. Derrien, J. Hassoun, S. Panero, and B. Scrosati, "Nanostructured Sn-C

Composite as an Advanced Anode Material in High-Performance Lithium-Ion Batteries," *Adv. Mater.*, vol. 19, no. 17, pp. 2336–2340, 2007.

[59] F. Jiang and P. Peng, "Elucidating the Performance Limitations of Lithium-Ion Batteries due to Species and Charge Transport through Five Characteristic Parameters," *Sci. Rep.*, vol. 6, no. August, pp. 1–18, 2016.

[60] T. Abe, F. Sagane, M. Ohtsuka, Y. Iriyama, and Z. Ogumi, "Lithium-Ion Transfer at the Interface Between Lithium-Ion Conductive Ceramic Electrolyte and Liquid Electrolyte-A Key to Enhancing the Rate Capability of Lithium-Ion Batteries," *J. Electrochem. Soc.*, vol. 152, no. 11, p. A2151, 2005.

[61] B. Kang and G. Ceder, "Battery Materials for Ultrafast Charging and Discharging," *Nature*, vol. 458, no. 7235, pp. 190–193, 2009.

[62] A. Mukhopadhyay and B. W. Sheldon, "Deformation and Stress in Electrode Materials for Li-Ion Batteries," *Prog. Mater. Sci.*, vol. 63, no. January, pp. 58–116, 2014.

[63] Y.-T. Cheng and M. W. Verbrugge, "Diffusion-Induced Stress, Interfacial Charge Transfer, and Criteria for Avoiding Crack Initiation of Electrode Particles," *J. Electrochem. Soc.*, vol. 157, no. 4, p. A508, 2010.

[64] Y. N. Zhou *et al.*, "High-Rate Charging Induced Intermediate Phases and Structural Changes of Layer-Structured Cathode for Lithium-Ion Batteries," *Adv. Energy Mater.*, vol. 6, no. 21, pp. 1–8, 2016.

[65] W. H. Woodford, Y.-M. Chiang, and W. C. Carter, "'Electrochemical

Shock' of Intercalation Electrodes: A Fracture Mechanics Analysis," *J. Electrochem. Soc.*, vol. 157, no. 10, p. A1052, 2010.

[66] K. Zhao, M. Pharr, J. J. Vlassak, and Z. Suo, "Fracture of Electrodes in Lithium-Ion Batteries Caused by Fast Charging," *J. Appl. Phys.*, vol. 108, no. 7, pp. 1–7, 2010.

[67] A. Yoshino, "The Birth of the Lithium-Ion Battery," *Angew. Chemie - Int. Ed.*, vol. 51, no. 24, pp. 5798–5800, 2012.

[68] S. J. Harris, A. Timmons, D. R. Baker, and C. Monroe, "Direct In Situ Measurements of Li Transport in Li-Ion Battery Negative Electrodes," *Chem. Phys. Lett.*, vol. 485, no. 4–6, pp. 265–274, 2010.

[69] A. Eftekhari, "On the Theoretical Capacity/Energy of Lithium Batteries and Their Counterparts," *ACS Sustain. Chem. Eng.*, p. A-D, 2018.

[70] S. R. Sivakkumar, J. Y. Nerkar, and A. G. Pandolfo, "Rate Capability of Graphite Materials as Negative Electrodes in Lithium-Ion Capacitors," *Electrochim. Acta*, vol. 55, no. 9, pp. 3330–3335, 2010.

[71] Y. Qi and S. J. Harris, "In Situ Observation of Strains During Lithiation of a Graphite Electrode," *J. Electrochem. Soc.*, vol. 157, no. 6, p. A741, 2010.

[72] M. S. Islam and C. A. J. Fisher, "Lithium and Sodium Battery Cathode Materials: Computational Insights Into Voltage, Diffusion and Nanostructural Properties," *Chem. Soc. Rev.*, vol. 43, no. 1, pp. 185–204, 2014.

[73] K. Abe, "Electrolyte Reagents for Lithium-Ion Batteries," *Sigma-Aldrich*.

[Online]. Available: https://www.sigmaaldrich.com/technical-documents/articles/technology-spotlights/electrolyte-reagents-for-lithium-ion-batteries.html#solvents.

[74]   K. Xu, "Electrolytes and Interphases in Li-Ion Batteries and Beyond," *Chem. Rev.*, vol. 114, no. 23, pp. 11503–11618, 2014.

[75]   E. Peled and S. Menkin, "Review—SEI: Past, Present and Future," *J. Electrochem. Soc.*, vol. 164, no. 7, pp. A1703–A1719, 2017.

[76]   S. S. Zhang, "A Review on Electrolyte Additives for lithium-ion batteries," *J. Power Sources*, vol. 162, no. 2 SPEC. ISS., pp. 1379–1394, 2006.

[77]   T. M. Bandhauer, S. Garimella, and T. F. Fuller, "A Critical Review of Thermal Issues in Lithium-Ion Batteries," *J. Electrochem. Soc.*, vol. 158, no. 3, p. R1, 2011.

[78]   D. Bernardi, E. Pawlikowski, and J. Newman, "A General Energy Balance for Battery Systems," *J. Electrochem. Soc.*, vol. 132, no. 1, p. 5, 1985.

[79]   L. Rao and J. Newman, "Heat-Generation Rate and General Energy Balance for Insertion Battery Systems," *J. Electrochem. Soc.*, vol. 144, no. 8, p. 2697, 1997.

[80]   L. H. Saw, K. Somasundaram, Y. Ye, and A. A. O. Tay, "Electro-Thermal Analysis of Lithium Iron Phosphate Battery for Electric Vehicles," *J. Power Sources*, vol. 249, pp. 231–238, 2014.

[81]   I. Baghdadi, O. Briat, A. Eddahech, J. M. Vinassa, I. Baghdadi, and P. Gyan, "Electro-Thermal Model of Lithium-Ion Batteries for Electrified

Vehicles Applications," in *IEEE International Symposium on Industrial Electronics*, 2015, pp. 1248–1252.

[82] J. Sun *et al.*, "Online Internal Temperature Estimation for Lithium-Ion Batteries Based on Kalman Filter," *Energies*, vol. 8, pp. 4400–4415, 2015.

[83] X. Lin *et al.*, "Online Parameterization of Lumped Thermal Dynamics in Cylindrical Lithium Ion Batteries for Core Temperature Estimation and Health Monitoring," *IEEE Trans. Control Syst. Technol.*, vol. 21, pp. 1745–1755, 2013.

[84] A. M. Bizeray, S. Zhao, S. R. Duncan, and D. A. Howey, "Lithium-Ion Battery Thermal-Electrochemical Model-Based State Estimation Using Orthogonal Collocation and a Modified Extended Kalman Filter," *J. Power Sources*, vol. 296, pp. 400–412, 2015.

[85] P. Amiribavandpour, W. Shen, D. Mu, and A. Kapoor, "An Improved Theoretical Electrochemical-Thermal Modelling of Lithium-Ion Battery Packs in Electric Vehicles," *J. Power Sources*, vol. 284, pp. 328–338, 2015.

[86] R. Zhao, S. Zhang, J. Liu, and J. Gu, "A Review of Thermal Performance Improving Methods of Lithium Ion Battery: Electrode Modification and Thermal Management System," *J. Power Sources*, vol. 299, pp. 557–577, 2015.

[87] S. Goutam, J. M. Timmermans, N. Omar, P. Van den Bossche, and J. Van Mierlo, "Comparative Study of Surface Temperature Behavior of

Commercial Li-Ion Pouch Cells of Different Chemistries and Capacities by Infrared Thermography," *Energies*, vol. 8, no. 8, pp. 8175–8192, 2015.

[88]   S. Panchal, I. Dincer, M. Agelin-Chaab, R. Fraser, and M. Fowler, "Transient Electrochemical Heat Transfer Modeling and Experimental Validation of a Large Sized LiFePO4/Graphite Battery," *Int. J. Heat Mass Transf.*, vol. 109, pp. 1239–1251, 2017.

[89]   J. S. Hong, H. Maleki, S. Al Hallaj, L. Redey, and J. R. Selman, "Electrochemical-Calorimetric Studies of Lithium-Ion Cells," *J. Electrochem. Soc.*, vol. 145, no. 5, pp. 1489–1501, 1998.

[90]   Y. Saito, K. Kanari, and K. Takano, "Thermal Studies of a Lithium-Ion Battery," *J. Power Sources*, vol. 68, no. 2, pp. 451–454, 1997.

[91]   S. Al Hallaj, J. Prakash, and J. R. Selman, "Characterization of Commercial Li-Ion Batteries using Electrochemical – Calorimetric Measurements," *J. Power Sources*, vol. 87, pp. 186–194, 2000.

[92]   A123 Systems, "Battery Pack Design, Validation, and Assembly Guide Using A123 Systems AMP20M1HD-A Nanophosphate Cells," 2014.

[93]   Q. Kellner, E. Hosseinzadeh, G. Chouchelamane, W. D. Widanage, and J. Marco, "Battery Cycle Life Test Development for High-Performance Electric Vehicle Applications," *J. Energy Storage*, vol. 15, pp. 228–244, 2018.

[94]   HobbyKing, "Turnigy 5000mAh 3S 65C Lipo Pack." [Online]. Available: https://hobbyking.com/en_us/graphene-3000mah-3s-65c-w-xt90.html.

[95] Idaho National Laboratory, "United States Advanced Battery Consortium Battery Test Manual for Electric Vehicles," 2015.

[96] C. K. Park *et al.*, "Variables Study for the Fast Charging Lithium Ion Batteries," *J. Power Sources*, vol. 165, no. 2, pp. 892–896, 2007.

[97] A. Krok, "Deep Dive: The 2017 Chevrolet Bolt's Electric Powertrain," *CNET*, 2016. [Online]. Available: https://www.cnet.com/roadshow/news/deep-dive-2017-chevrolet-bolt-electric-powertrain/.

[98] M. Muratori, M. Canova, Y. Guezennec, and G. Rizzoni, "A Reduced-Order Model for the Thermal Dynamics of Li-Ion Battery Cells," in *IFAC Symposium Advances in Automotive Control*, 2010, pp. 192–197.

[99] N. Nieto, L. Díaz, J. Gastelurrutia, F. Blanco, J. C. Ramos, and A. Rivas, "Novel Thermal Management System Design Methodology for Power Lithium-Ion Battery," *J. Power Sources*, vol. 272, pp. 291–302, 2014.

[100] Environmental Protection Agency, "Annual Certification Data for Vehicles, Engines, and Equipment," 2018. [Online]. Available: https://www.epa.gov/compliance-and-fuel-economy-data/annual-certification-data-vehicles-engines-and-equipment.

[101] Y. Ye, L. Huat, Y. Shi, K. Somasundaram, and A. A. O. Tay, "Effect of Thermal Contact Resistances on Fast Charging of Large Format Lithium Ion Batteries," *Electrochim. Acta*, vol. 134, pp. 327–337, 2014.

[102] J. Yi, S. Kim, B. Shin, T. Han, and S. Park, "Three-Dimensional Thermal

Modeling of a Lithium-Ion Battery Considering the Combined Effects of the Electrical and Thermal Contact Resistances between Current Collecting Tab and Lead Wire," vol. 160, no. 3, pp. 437–443, 2013.

[103] M. Broussely, P. Biensan, F. Bonhomme, and P. Blanchard, "Main Aging Mechanisms in Li Ion Batteries," *J. Pow*, vol. 146, pp. 90–96, 2005.